CHARACTERIZATION OF SOLID STATE DEFECT SYSTEMS FOR QUANTUM COMPUTING, COMMUNICATION, AND SENSING

Stanley A. Breitweiser

A DISSERTATION

in

Physics and Astronomy

Presented to the Faculties of the University of Pennsylvania

in

Partial Fulfillment of the Requirements for the

Degree of Doctor of Philosophy

2023

Supervisor of Dissertation

Lee C. Bassett, Associate Professor - Electrical and Systems Engineering

Graduate Group Chairperson

Bo Zhen, Assistant Professor - Physics and Astronomy

Dissertation Committee

Marija Drndić, Fay R. and Eugene L. Langberg Professor of Physics - Physics and Astronomy
Philip Nelson, Professor - Physics and Astronomy
Anthony Sigillito, Assistant Professor - Electrical and Systems Engineering

CHARACTERIZATION OF SOLID STATE DEFECT SYSTEMS FOR QUANTUM COMPUTING, COMMUNICATION, AND SENSING

To my friends, family, and loved ones who were not able to see this moment.

Ad Astra Per Aspera

ACKNOWLEDGEMENT

The list of people who supported and encouraged me during my PhD, and to whom I am eternally indebted, runs longer than my thesis itself, so here I mention only a few.

First, I would like to acknowledge my thesis advisor, Lee Bassett, without whom this work would not have been possible. Beyond financial and research support, Lee taught me what it means to be a scientist - how to critically look at research, both others' and my own, and create experiments that revealed the true nature of the systems we are studying.

I must also acknowledge the many fellow students and postdocs who helped me during my time at Penn. David, Yung, and Annemarie in particular taught me almost everything I know about how to work in a lab. Ian, Sebastian, and my other classmates in Physics, ESE, and the Bassett Group kept me sane and on the right track.

And finally I am of course forever grateful for my family, especially my parents, Chip and Agnee, and my brother, Nick. Even though you all told me not to go to graduate school I know you are still proud of me.

ABSTRACT

CHARACTERIZATION OF SOLID STATE DEFECT SYSTEMS FOR QUANTUM COMPUTING, COMMUNICATION, AND SENSING

Stanley A. Breitweiser

Lee C. Bassett

Solid state defects have emerged as a leading candidate for platforms in quantum computing, communication, and sensing. The electronic spins localized around these defects have many advantages such as room temperature coherence, spin dependent optical transitions which enable visible-wavelength initialization and readout, and resonant frequencies compatible with widely available off-the-shelf microwave hardware. Furthermore, the nuclear spins coupled to these electronic spins provide additional quantum registers which can be used as long-lived memories, ancilla qubits to enhance sensing and communication schemes based on the electronic spin, or for general purpose computation. However, unlike systems which are all identical, such as trapped atoms, or systems which are man-made, such as superconducting circuits, the formation and structure of defects, as well as their coupled nuclear spins, is stochastic and difficult to model using *ab initio* methods. This thesis focuses on methods to efficiently and precisely characterize the properties of these systems. After presenting sufficient background for a general scientific audience, a method is outlined for robustly and efficiently quantifying the optical properties of defect-based emitters, even if the emitters are heterogeneous. We show how this method can be used to study treatment effects in novel systems, such as hexagonal Boron Nitride (hBN), where a new class of defect-based emitters has been identified but proven difficult to characterize - largely due to the widely varying optical properties of emitters which are believed to arise from the same defect. We then

describe the infrastructure developed within the laboratory to generate, run, and simulate the results of experiments such as those used in the remainder of the thesis. This is followed by an explanation of some of the state of the art techniques used to identify, control, and map the nuclear spins coupled to an electronic spin within a defect system. We then show how these techniques can be expanded to precisely measure the Hamiltonian parameters of a single nuclear spin - which opens the door to a new era where individual nuclear spins can be used to measure their environment and reveal information about the local molecular and crystal structure. Finally, this thesis concludes with a brief discussion of the ongoing work and future directions inspired by the ideas and work presented in this thesis.

TABLE OF CONTENTS

LIST OF TABLES

LIST OF ILLUSTRATIONS

CHAPTER 1

QUANTUM SYSTEMS AND THEIR APPLICATIONS

1.1. Introduction

At the turn of the 20th century, the theory of quantum mechanics was demonstrated to replicate the behavior of light and atomic systems, resolving several long standing problems in physics. [1, 2] Bell's theorem later proved that quantum mechanics was fundamentally incompatible with any local, deterministic classical theory. [3] The departure from classical mechanics, which accurately described natural phenomena at most scales probed by experiments until then, as well as relativistic mechanics, which was later shown to accurately describe the behavior of bodies in space, has remained a mystery of both philosophy and science.

However, quantum mechanics can be used to understand any system which obeys a few basic mathematical postulates.[4] Among these are *superposition*, *coherent evolution*, and *measurement*. In finite systems, which we are primarily concerned with here, *superposition* posits that any system with discrete states $|0\rangle$, $|1\rangle$, $|2\rangle$, ... can be exist in a complex combination

$$|\psi\rangle = c_0 |0\rangle + c_1 |1\rangle + c_2 |2\rangle + ... \quad s.t. \quad \sum_i |c_i|^2 = 1. \tag{1.1}$$

Coherent evolution posits that states evolve according to Schrödinger's equation

$$H |\psi\rangle = i\hbar \frac{d}{dt} |\psi\rangle , \tag{1.2}$$

where H is a Hermitian operator known as the Hamiltonian and $\hbar$ is a fundamental constant known as the reduced Planck's constant. (Henceforth we will use units such that $\hbar = 1$ for simplicity). *Measurement* posits that upon measuring any observable A, described mathematically as a Hermitian operator $A = \sum_i \lambda_i |a_i\rangle \langle a_i|$ where $\langle a_i | a_j \rangle = \delta_{ij}$, each eigenstate $|a_i\rangle$ is measured with probability given by the square of its overlap with the state being

measured, $P(|a_i\rangle) = |\langle a_i|\psi\rangle|^2$, and after the measurement the state is left in the eigenstate it was measured to be in.

While these systems have long been believed to be difficult to simulate classically, it was separately proposed by Yuri Manin in 1980 and Richard Feynman in 1982 that these systems might therefore be used to model other systems, both classical and quantum, which are themselves difficult to simulate. [5, 6, 7] This led to the field of quantum computing, whereby quantum systems are used for useful computations, and the related field of quantum networking, where quantum information is transmitted long distances for computation or other uses. Another related field, known as quantum sensing, has also become of interest - where the quantum properties of a system may be used to gain additional information about the local fields and environment surrounding the system. Each application poses its own slightly different requirements, which we shall explore now.

1.2. Quantum Applications and Requirements

In this section, we consider three of the most promising applications for quantum systems: quantum computation, quantum communication, and quantum sensing. All of these fields seek to take advantage of the unique properties of quantum systems described above to gain an advantage over systems characterized by classical mechanics. However, many of the properties of quantum systems that make them useful also make them difficult to work with. Superposition states are often quite unstable due to incoherent evolution which is introduced into the system by interactions with external degrees of freedom and eventually returns systems to a quasi-classical mixed state. Measurements of quantum systems are often difficult to implement, and since they collapse the quantum superposition many experiments are required to observe the distribution of measurement outcomes. For each of the three quantum applications described above, we give examples of the potential uses and explain what properties each application requires from the underlying quantum system,

1.2.1. Quantum Computing

In quantum computing, an initial state $|\psi_i\rangle$ is coherently evolved to a final state $|\psi_f\rangle$ according to some predetermined algorithm. Typically the algorithm is expressed as a series of unitary operators U_i, known as gates, which are sequentially applied to the state

$$|\psi_f\rangle = U_N U_{N-1} ... U_0 |\psi_i\rangle . \tag{1.3}$$

In analogy with classical computation, these operations can perform useful information processing. In fact, for many known problems such as integer factorization[8], database searching [9], and simulating other quantum systems[10], quantum algorithms have been shown to exponentially outperform the fastest known classical algorithms. For a thorough introduction to quantum computation, we point the interested reader to the seminal text by Nielsen and Chuang [4]. The requirements for a system to be used as a quantum computer are well captured by the Divincenzo Criteria, proposed by David Divincenzo in 2000. [11] These are

- A scalable physical system with well characterized qubits
- The ability to initialize the state of the qubits to a simple fiducial state, such as $|000...\rangle$
- Long relevant decoherence times, much longer than the gate operation time
- A "universal" set of quantum gates
- A qubit-specific measurement capability

Each one of these requirements is simple to describe, but requires a complex union of science, technology, and engineering to realize. Any general purpose quantum computing architecture will need to address all five.

1.2.2. Communication

While quantum computations generally assume entirely local operations, another class of quantum applications concerns quantum information which is shared or distributed across large distances. Such quantum communication enables provably secure key distribution across long distances[12], "blind" quantum computation where quantum algorithms can be run remotely without compromising security[13, 14], as well as quantum teleportation - whereby quantum information can be quickly transmitted over long distances using entanglement and classical communication [15, 16, 17]. In addition to the five requirements described above, DiVicenzo laid out two additional requirements for quantum networking[11]

- The ability to interconvert stationary and flying qubits
- The ability faithfully to transmit flying qubits between specified locations

While quantum communication platforms require the original five DiVincenzo criteria for quantum computing, sometimes a tradeoff in one of these areas for an improvement in the two additional communication criteria is advantageous. For example, many quantum computation platforms do not have a straightforward way to move computational qubits from one location to another, and rely on potentially inefficient processes to coherently convert the qubit states to some form of electromagnetic signal. Visible and near-IR photonic signals are of particular interest, as they have low attenuation rates in existing optical fibers, but can require inefficient upconversion from the microwave signals obtained from some qubit architectures. Since many quantum communication algorithms do not require long gate sequences, slower and less efficient gates may be acceptable in exchange for better conversion and transmission of quantum information into photonic signals.

1.2.3. Quantum Sensing

Quantum sensing seeks to use the intrinsic sensitivity of quantum systems to measure local fields.[18] Quantum systems have already been shown to detect magnetic[19, 20] and electric[20] fields, as well as temperature[21, 22, 23], pressure[24], and even gravity[25, 26] and rotation[27]. In addition to offering a highly sensitive measurement of local fields, the use of quantum entanglement between many qubits enables more accurate measurements, lowering the detection limit and increasing the precision of sensing.[28, 29, 30] While many requirements for quantum sensing are similar to those for quantum computing, paradoxically we want our qubit systems to be sensitive to the local field we are trying to measure. This is counter-intuitive because normally we look for qubits which are insensitive to external fields, as they can lead to spectral drift and decoherence which destroys the quantum state. However, we can either find qubits which are only sensitive to the specific fields we are trying to measure, or we may engineer and operate our qubits in a way that enhances their sensitivity to the fields we want to measure while simultaneously causing them to become insensitive to other fields. Similar to quantum communication, some of the requirements for general purpose quantum computation may be relaxed. Again, long sequences of arbitrary gates are not strictly required - although we will see later on how they might be used to improve our measurements. However, one non-trivial requirement for quantum sensing is the ability to locate the quantum system close to the fields we want to measure. This is not always as simple as it might sound - since often quantum systems require low temperatures, high vacuums, and/or strong electromagnetic shielding to maintain long decoherence and relaxation times.

1.3. Quantum Architectures

While many architectures have been proposed for quantum technology applications, and many more will certainly be explored in the coming years, a few have emerged as leading

candidates - each with their own benefits and drawbacks. Among these are platforms based on atomic systems, superconducting circuits, and the spins of subatomic particles. Here we look at a few of these systems with the goal of comparing their advantages and disadvantages with respect to the criteria discussed above. For a more complete and relatively accessible - albeit somewhat outdated - overview of quantum computing platforms, we direct the interested reader to [31].

1.3.1. Atomic Systems

Broadly speaking, quantum systems of this type are based on individual atoms or small molecules. Because each atom is identical and the transitions are well understood, a qubit can be chosen from two levels with favorable properties - generally the ground state and some excited state - and controlled used resonant lasers. [31] One version of such a system uses ions trapped by oscillating electric fields under vacuum, which are then cooled and manipulated using lasers. [32] Laser-controlled harmonic modes couple ions in the same trap and give rise to intrinsic two-qubits gates, even between distant ions. Another version used neutral atoms trapped by lasers into optical lattices[33], with two qubit gates induced by bringing nearby atoms together to cause exchange interactions.[34] While trapping and controlling the atoms can be labor intensive and requires specialized equipment, the resulting qubits have many favorable properties for quantum computation. Decoherence times are long and gates, as well as readout and initialization, have very high fidelities. Because of this, systems of ultracold atoms have pioneered the field of quantum simulations[35], where one quantum systems is used to simulate the physics of another, and are among the most advanced platforms for quantum computation.[36] However, there are fundamental limits to the number of qubits that can be efficiently trapped in a single trap or optical lattice.[31] Current efforts are under way to explore how to shuttle ions in between traps[37] or transmit information between traps using photonic interactions[38] to enable larger computers based on this technology, as well

as to miniaturize the platform.

Atomic systems can also detect magnetic fields by measuring the induced Zeeman splitting, which changes the Larmor precession frequency of different spin states. [19] Magnetometers based on atomic vapors have displayed among the highest sensitivities due to their exceptional coherence times and well understood Hamiltonians[39], and have even been used to measure nerve activity.[40] However, the use of such magnetometers *in situ* is not immediately straightforward, as they require carefully controlled environments to operate.[18]

1.3.2. Superconducting Circuits

Qubits can also be built using the charge[41, 42, 43], flux[44, 45, 46], or phase[47] state of a superconducting circuit. Josephson junctions are used as non-linear elements to separate the transitions, and the qubit is defined between the ground and lowest excited states. Microwaves are used to both control and readout the qubits, and initialization can be performed using either thermal cooling or microwave-assisted techniques. Since there is no resistance below the critical temperature, these states can persist for long times relative to the fast microwave control used for gates. The processes used to construct these devices are broadly compatible with existing semiconductor fabrication techniques, and since the transition frequencies can be tuned by the device parameters they can be chosen to be compatible with widely available off-the-shelf hardware and resistant to sources of decoherence and relaxation.[31]

The largest modern quantum computers are universally based on superconducting circuits[48, 49], and they have continued to scale at a rapid pace. However, these qubits face their own limitations. Since the circuit dimensions (typically $\approx 100\,\mu$m) are set by the desired transition frequencies ($\approx 5\,$GHz) and noise considerations, only a limited number can be placed on a chip small enough to fit into the dilution refrigerators required to achieve supercon-

ducting temperatures and avoid thermal excitations. Furthermore, the host materials must be strictly controlled to prevent Two-Level Systems and other defects from interacting with the qubits and causing decoherence or relaxation.[31] Finally, due to the semi-stochastic nature of the fabrication process, some superconducting architectures face scaling issues due to the steep combinatorial growth of frequency collision probabilities as the number of qubits increases.

For quantum sensing applications, among the most sensitive and widely-used magnetometers are those based on Superconducting Quantum Interference Devices (SQUIDs)[50, 51, 52]. SQUIDs take advantage of the relationship between the magnetic field flux, superconducting phase, and current of a superconducting circuit containing one or more Josephson junctions to measure the external magnetic field. Their fast acquisition times and high sensitivities have found use in an array of biological and chemical applications. However, once again the size of the devices is limited by the desired transition frequencies, and therefore fields can only be measured with a spatial resolution equivalent to the size of the devices.[18] Recent efforts have focused on shrinking the size of SQUID based sensors below $1\,\mu$m to further improve their spatial resolution.[53, 54] Still, the requirement to cool the devices to cryogenic temperatures limits their application, especially *in vivo*.

1.3.3. Subatomic Spins

Qubits of this type are defined by the spin of individual or small collections of electrons and/or nuclei. One such architecture is based on electrons trapped within semiconductor heterostructures by gate-defined quantum dots. Individual electron spins can be initialized and read out by manipulating gate voltages to induce spin-dependent charge transport and controlled by microwave signals. Two-qubit gates can be implemented by a gate-controlled exchange interaction between nearby spins. Because the underlying technology is similar to existing transistor platforms used in classical computers, this platform has a clear path to

scalability. However, the devices are still difficult to fabricate and sensitive to charge noise, and further research is still needed to improve yields.

Another version of such an architecture is based on subatomic spins trapped within the atomic structure of materials. Among the first quantum computers were those based on ensembles of nuclear spins within liquid molecules.[55, 56, 57] The nuclear spins can be controlled using radio frequency signals, with qubits defined by the collective spin state of ensembles of nuclei at specific atomic sites within the identical molecules. Each qubit has a unique resonant frequency due to the local field environment caused by the molecular structure, and therefore qubits can be addressed and read out individually. While initialization relied on thermal alignment of the spins, and the readout signal from each nucleus was small, sufficient signal could be obtained due to the large number of nuclei in any macroscopic size sample. However, these systems suffered from rapid decoherence due to the interactions with other degrees of freedom within the lattice. This led to the development of control techniques, known as dynamical decoupling, which would isolate the nuclei from the effects of the environment. [58, 59, 60] Later proposals extended this to focus on nuclear spins in bulk semiconductors, with readout mediated by coupled electronic spins. [61]

As optical and microwave equipment improved and became more accessible, and further work done on the materials synthesis, attention turned to individual defects within semiconductors, such as the Nitrogen-Vacancy (NV) center in diamond.[62] These defects can host electronic degrees of freedom with spin-dependent optical transitions, offering a path to initialize and readout individual subatomic spin states using confocal microscopy techniques.[63] Spin levels are split by an external magnetic field and can be controlled using microwaves.[64] By leveraging the ever-improving control over materials growth and treatment, as well as using dynamical decoupling techniques, relaxation and decoherence times many orders of magnitude longer than control times are easily achievable, even at room temperature. Additional

qubits, which can be used as ancilla, long-lived memories, or for general computation, are provided by nuclear spins coupled to the electronic spin, which display even longer relaxation and decoherence times due to their weak intrinsic coupling mechanisms. These spins can be initialized, controlled, and read out using their strong coupling to the electron spin.[65]

Solid state defect systems have attracted particular interest for applications in quantum communication and sensing. For quantum communication applications, the intrinsic mechanism for converting qubits into visible wavelength photonic signals precludes the need for inefficient up-conversion processes, and nuclear spins offer long-lived registers capable of storing information and implementing rudimentary error correction schemes. Many experiments demonstrating long range entanglement[66, 67] and proposals for quantum repeater networks[68] have been based on solid state defects. Since defect systems often do not require strong vacuums or low temperatures and can be coupled to free-space optics, they are often advantageous for quantum sensing as they can easily be located next to systems of interest with little or no disruption. The quantum states are localized to a few atomic sites and therefore offer an unparalleled degree of localization, and furthermore are generally protected from the environment by their host material. Sensors based on these technologies have already been used to create highly-sensitive, highly localized sensors of magnetic[69, 70, 71, 72] and electric[73] fields and temperature[22], and been demonstrated to collect signals from very small material samples[74, 75]. They have also been demonstrated in living cells[76] and as simultaneous 2D sensors [77]. Furthermore the coupled nuclear spins can be used to improve the sensitivity of local field measurements, and the variety of host material systems offers a plethora of form factors and properties for different applications.[78, 18]

However, these systems are not without their drawbacks. The formation of defects is stochastic and not always well understood. Furthermore, the intrinsic charge, spin, and optical dynamics of the system must be carefully characterized before they can be used for appli-

cations. While *ab initio* methods can give some insights, often the only way to gain reliable information about the system is through experimental methods. The remainder of this thesis concerns the physics of these defect systems, with a focus on characterizing and controlling their properties for use in quantum technologies such as communication and sensing. While we study a few particular examples, the insights and techniques are broadly applicable to a wide class of systems with similar Hamiltonians.

CHAPTER 2

SOLID STATE SPIN DEFECTS

Solid state materials can host a variety of point defects, where the chemical makeup is altered in a finite (zero-dimensional) region of the crystal lattice. These defects can be formed from vacancies (where an atom is missing), substitutions (where an atom is replaced with an atom of another type), interstitial defects (where an atom is located within a region that should be empty), or any combination of these. If the host material is a semiconductor, with a finite bandgap between the conduction and valence bands, these defects can host local electronic states with well-defined charge, spin, and orbital properties. Similar to atomic systems, defects of the same type are always identical and, in materials with sufficiently low defect densities, defects can be isolated and addressed optically using confocal microscopy techniques. However, unlike isolated atomic systems, these defects also interact with other defects and the host lattice - which is the source of both many advantageous properties and challenges for quantum applications. In this chapter we explore an important and well characterized example for these systems - the Nitrogen-Vacancy (NV) center in diamond. We conclude by highlighting the important properties of this system, as well as the drawbacks that must be overcome, and how they might inform our exploration of new materials for similar defects.

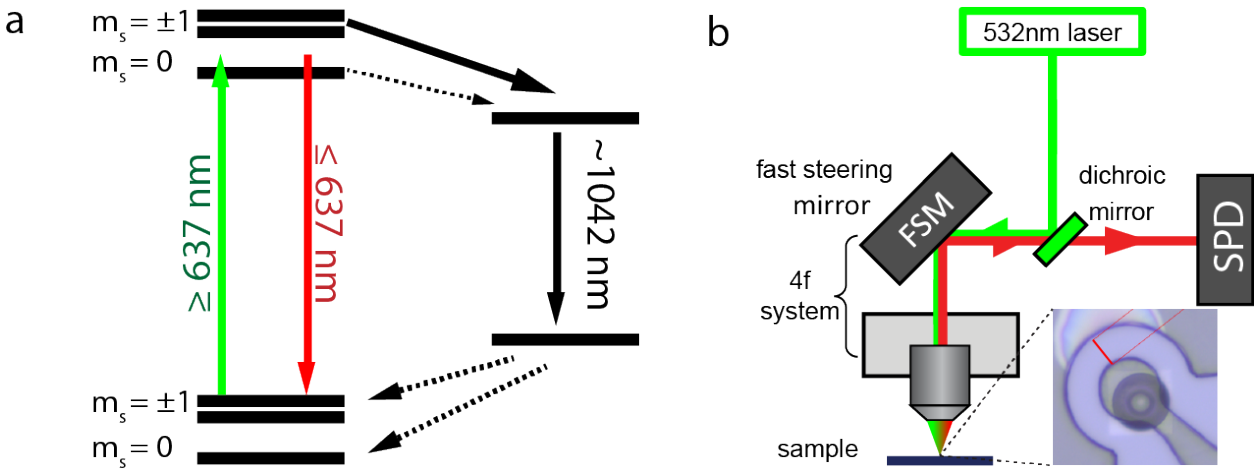

Figure 2.1: (a) The electronic level structure of a room temperature negatively charged NV center. A triplet ground state couples to an effective triplet excited state through a radiative transition with a ZPL of 637 nm, which can be excited through shorter wavelength light and spontaneously decays. A spin-dependent inter-system crossing allows the excited state to decay to a singlet state through a non-radiative transition that is more likely if the electron spin started in an $m_s = \pm 1$ state. A further IR decay into another singlet state followed by another non-radiative transition brings the electron back to the triplet ground state, with the original spin information having been lost. (b) A simplified diagram of a typical confocal microscopy setup used to initialize and readout individual NV centers in diamond. 532 nm laser light is steered using a fast steering mirror (FSM) and focused onto a single NV center. Red light emitted by spontaneous decay from the excited state of the NV center is collected using the same optics and sent to a Single-Photon Detector (SPD) using a low-pass dichroic mirror to separate it from the laser path. (Inset) Optical image of a typical bulk diamond sample. A Solid-Immersion Lens (SIL, shadowed disk) is milled out of the diamond on top of an NV center to improve the optical collection efficiency. A circular antenna (blue w/ outline) is fabricated around the SIL to deliver strong microwave fields to control the NV electronic spin. Red scale bar indicates approximately 10 μm.

The Nitrogen-Vacancy (NV) center in diamond is formed from a substitutional Nitrogen next to a vacant site within the Carbon lattice. While it is found in naturally occurring and Chemical Vapor Deposition (CVD) grown diamond, it can also be created through a process using ion implantation or radiation followed by annealing. [79] Multiple charge states are possible; however, the negatively charged (NV^-) state is the most common and of particular

interest in the samples studied for quantum applications. In this charge state, six electrons (three from neighboring Carbons, two from the Nitrogen, and one captured from elsewhere in the lattice) combine to form an isolated state space deep within the band gap. Henceforth we simply refer to this charge state as an NV center, except in cases where giving the charge state explicitly is necessary for clarity. Here we give a brief overview of the relevant properties of the NV center pertinent to the remainder of this thesis. For a more complete treatment of the NV center, we point the interested reader to [80].

The room temperature level structure of the NV center is shown in Fig. 2.1(a). A triplet (spin-1) electronic ground state is separated by 1.945 eV from an effective spin-1 excited state arising from fast mixing within the larger excited orbital state space. In both of these, the spin states with Z projection $m_s = 0$ lie below those with $m_s = \pm 1$ at zero magnetic field due to a strong quadrupolar splitting, which is believed to arise from the spin-spin interaction of the individual electrons forming the state. Direct transitions between the ground and excited states preserve the electronic spin and are mediated by a combination of photons and phonons, with only a few % of the spontaneous emission being into the 637 nm Zero Phonon Line (ZPL). Between these states lie two singlet (spin-0) states, separated by 1.19 eV (1042 nm). Non-radiative transitions between the triplet and singlet manifolds, called the inter-system crossing (ISC), are spin dependent. While the exact rates for each branch of the inter-system crossing are not accurately known, triplet states with $m_s = \pm 1$ are more likely to decay through the ISC, while singlet states may decay into any of the ground level spin states.

Fig. 2.1(b) shows a simplified view of a typical setup used for bulk samples. Laser light above the ZPL (typically 532 nm in the case of NV centers) is steered using a Fast Steering Mirror (FSM) and focused onto the sample such that it illuminates only a single defect. Light emitted by the defect, which is red shifted to or below the ZPL, is collected by the

same optics, and then separated from the excitation pathway using a low-pass dichroic mirror and enters a Single Photon Detector (SPD) used for measurement. A Solid Immersion Lens (SIL), shown in the inset, is milled out of the diamond surface above an NV of interest and used to improve collection efficiency. A circular antenna is deposited onto the diamond surface around the NV/SIL and connected to an external source of microwaves to enable fast control of the spin state. More details about the specific equipment used in our experiments are given in Section 4.1.

2.2. Initialization and Readout of the Electronic Spin

By illuminating the NV with 532 nm light, the electronic ground state is stimulated into the excited state. If the electron started in $m_s = 0$, it will maintain that spin state and will most likely return to the ground state directly without changing spin. However, if the electron started in $m_s = \pm 1$, it is likely to undergo the ISC transition through the singlet states, and might return to ground state with an $m_s = 0$ spin projection. By repeatedly exciting the ground state with continuous illumination, the spin state will most likely eventually end in the $m_s = 0$ state, with a typical equilibrium purity of $> 90\,\%$.

Readout of the spin state can also be achieved with 532 nm illumination. Since states with $m_s = \pm 1$ are more likely to decay through the ISC after excitation, they will emit less visible light on average after many repetitions. However, this contrast is limited by the ISC rates and the collection efficiency of the optical path, and since repeated illumination re-initializes the spin state there is a limit to how much signal can be gained from a single measurement. Instead, states used for computation, communication, or sensing must be prepared many times and repeatedly measured in order to gain sufficient information using this technique. More efficient readout methods such as spin-to-charge conversion, nuclear assisted readout, and low-temperature resonant readout have been studied but are beyond the scope of this thesis.[81]

2.3. Microwave Control

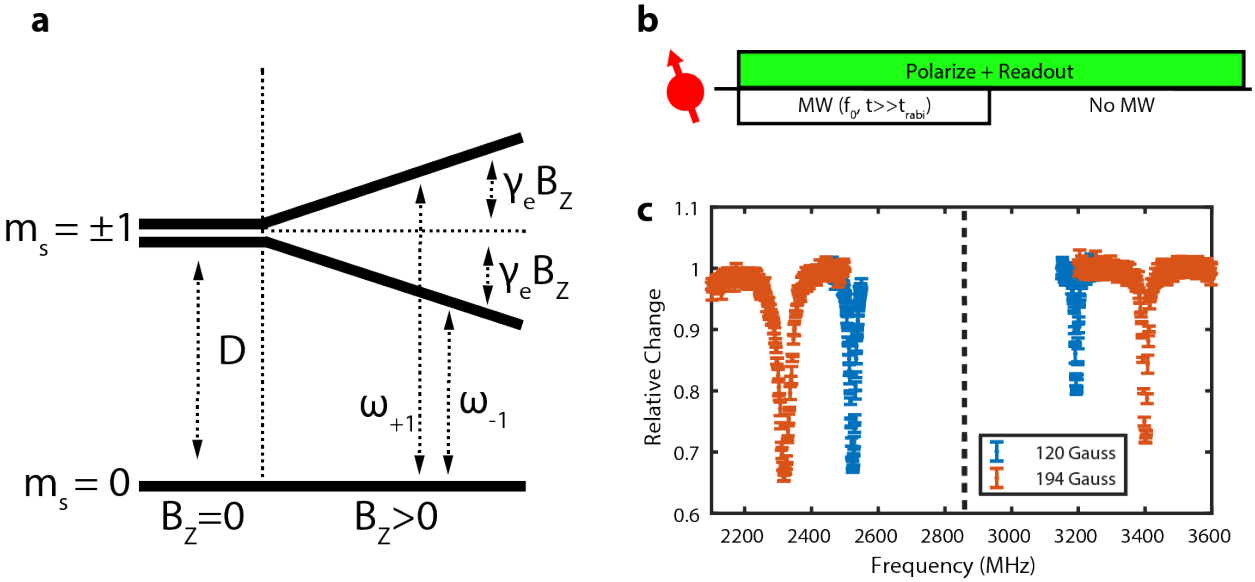

Figure 2.2: (a) With no external field, the ground state electronic spin of the NV center is split between the $m_s = 0$ and $m_s = \pm 1$ states by $D \approx 2\pi \times 2.87\,\mathrm{GHz}$. The $m_s = \pm 1$ states may further be mixed and split by a highly sample dependent E parameter. As an external field, B_Z, is applied along the NV axis, the $m_s = \pm 1$ states split by the Zeeman splitting at a rate of $\gamma_e \approx 2\pi \times 2.8\,\mathrm{MHz/Gauss}$. This gives two distinct transition frequencies, $\omega_{\pm 1}$, which can be probed using microwaves. (b, c) Experimental sequence and data from an ODMR experiment at two different magnetic fields. Continuous laser illumination cycles the electron through the excited state. When the applied microwave tone is off-resonance, the electron is quickly pumped into the $m_s = 0$ state and gives off bright photoluminescence (PL). When the microwave tone is resonant with either ω_{-1} or ω_{+1}, which are symmetric around the Zero Field Splitting D (dashed line), the electron goes into the $m_s = \pm 1$ state, and is more likely to undergo the non-radiative ISC transition - leading to a decrease in PL. As the external field, B_Z, is increased, the spacing between $\omega_{\pm 1}$ increases according to the Zeeman splitting, γ_e

Within the ground state, the electron spin Hamiltonian of an NV center is given by[82]

$$H_e = DS_Z^2 + E(S_X^2 - S_Y^2) + \gamma_e B \cdot S \tag{2.1}$$

Where $S = (S_X, S_Y, S_Z)$ is the electron spin operator, $D \approx 2\pi \times 2.87\,\text{GHz}$ is the Zero-Field Splitting (ZFS) between the $m_s = \pm 1$ and $m_s = 0$ states, E is a highly NV dependent parameter which mixes and splits the $m_s = \pm 1$ states at low fields, $\gamma_e \approx 2\pi \times 2.8\,\text{MHz/Gauss}$ is the gyromagnetic ratio of the electron spin, and $B = (B_X, B_Y, B_Z)$ is the external field applied along the NV axis. Fig. 2.2(a) shows the level structure arising from this Hamiltonian. By applying a non-zero magnetic field $B_Z > 0$ along the NV axis, the $m_s = \pm 1$ levels may be split, yielding direct transitions between $m_s = 0$ and either $m_s = +1$ or $m_s = -1$, with resonance frequencies ω_{+1} and ω_{-1}, respectively. By applying alternating fields perpendicular to the NV axis at these frequencies, for example using the circular antenna shown in Fig. 2.1(b), we can coherently control the electron spin state.

Fig. 2.2(b) shows the photoluminescence (PL) obtained from continuously illuminating a single NV while applying microwave tones of varying frequencies. When the field is off resonance, the electron stays in the $m_s = 0$ state, and simply undergoes continuous excitation and decay. However, when the microwave tone is resonant with the transition frequencies $\omega_{\pm 1}$ the electron is placed into the $m_s = \pm 1$ state, which gives decreased visible photoluminescence as it is more likely to undergo the non-radiative ISC decay pathway. These resonances are split by the static magnetic field and are symmetric about D. While this technique is an effective way to calibrate the magnetic field, the continuous optical excitation causes the electron to constantly cycle between states. This both broadens the resonance and prevents the electron from achieving a coherent state of interest. To fix both of these issues, we switch to pulsed experiments, where microwaves are used to coherently manipulate the electron spin in between initialization and readout using 532 nm laser light as described in the above section. While either transition can be used to define and control a qubit, or both can be used to define and control a three-level "qutrit," generally experiments are done using the $m_s = 0$ to $m_s = -1$ transition due to the greater efficiency of microwave components at

lower frequency. Henceforth, all experiments in this thesis are performed in this subspace, unless specified otherwise.

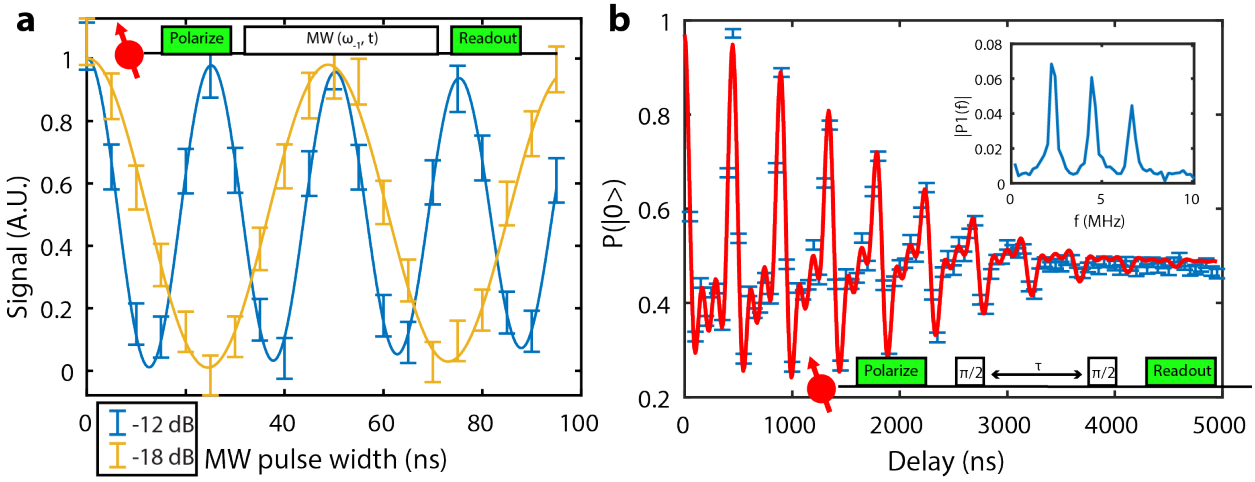

Figure 2.3: (a) Data from a Rabi experiment, where a microwave pulse resonant with the $m_s = 0$ to $m_s = -1$ transition is applied with a variable total pulse time, showing coherent oscillations between the two states. The signal is calibrated so that the fitted oscillation covers the range from 0 to 1. As the microwave signal is attenuated, the frequency of the oscillation decreases, shrinking approximately as the square root of the applied power. (b) Ramsey experiment, where $\frac{\pi}{2}$ pulses are applied at the beginning and end of the experiment to prepare and measure the electronic spin along the equator of the Bloch sphere. In between, the electronic spin is allowed to evolve freely for a variable amount of time. The phase of the final $\frac{\pi}{2}$ pulse is swept at $2\pi \times 5\,\mathrm{MHz}$ with the free evolution time, to allow small oscillations to become more visible. The signal shows multiple beating oscillations, before eventually decaying with a characteristic time $T_2^* \approx 2.4(1)\,\mu\mathrm{s}$. The signal is calibrated using a blank line (assumed to give a pure $m_s = 0$ state) and a calibrated π pulse (assumed to give a state with no $m_s = 0$ overlap) interleaved with the experimental lines to determine the occupation probability of the electron in the $m_s = 0$ state. (Inset) Power spectrum of the Ramsey signal, showing three distinct peaks - evidence of the $\approx 2\pi \times 2\,\mathrm{MHz}$ splitting caused by the coupling of the electron to the Nitrogen-14 nuclear spin.

Fig. 2.3(a) shows the result of applying microwave pulses of varying lengths at the resonance frequency ω_{-1}. The observed oscillations, named Rabi oscillations, demonstrate coherent transitions between the electronic spin states, which can also be viewed as off-axis rotations of the Bloch sphere. The frequency of the oscillation, known as a Rabi frequency, shows how powerful the applied microwave field is, and as expected grows as the square root of the

power applied to the antenna.

Using the result from the Rabi experiment, we can calibrate our pulses to cause the electronic spin to undergo a $\frac{\pi}{2}$ rotation, placing it along the equator of the Bloch sphere. We then allow the electron state to evolve freely for a period of time. if there are no couplings in the system the electron will stay in the same state (in the rotating frame of the microwave tone). However, if the electron is coupled to another spin, such as a nuclear spin, it will rotate along the equator of the Bloch sphere with the direction and speed of rotation dependent on the sign and strength of the coupling and the state of the external spin. After allowing the electronic spin to evolve, a final $\frac{\pi}{2}$ pulse maps the phase of the electron spin along the Bloch sphere equator back to a Z polarization which can be read out. To make small oscillations easier to detect, the phase of the final $\frac{\pi}{2}$ pulse can be swept according to the evolution time at a certain frequency.

Fig. 2.3(b) shows the result of such a Ramsey experiment. Several beating oscillations are seen before the signal decays due to incoherent processes, with a characteristic time $T_2^* \approx 2.4(1)\,\mu$s. The inset shows the power spectrum of the obtained signal, which shows two peaks approximately 2 MHz on either side of a central peak near ≈ 5 MHz, which was the frequency at which the final $\frac{\pi}{2}$ pulse phase was swept. This is consistent with a coupling to a spin-1 system such as the Nitrogen-14 nuclear spin within the NV center. The decay is also caused by nuclear interactions with the Carbon-13 spin bath, although no single carbon shows a strong enough coupling $|A| \gtrsim \frac{1}{T_2^*}$ to appear in this Ramsey experiment. More advanced techniques to detect and control the nuclear spins are discussed in Chapter 5 and Chapter 6.

2.4. New Defect Systems

The NV center has several advantages which have led it to be used for foundational demonstrations of quantum computing, communication, and sensing. Decades of research into the growth and treatment of diamond have allowed stable, isolated NV centers to be created in many types of diamond - from bulk diamond to nanoparticles and thin membranes - allowing a variety of form factors suitable for different applications[83]. The ability to initialize and readout the electronic spin state using visible wavelength light allows experiments to use relatively simple free-space or fiber-based optics. Furthermore, the microwave frequencies required for coherent control ($\approx 1 - 4\,\mathrm{GHz}$) can be generated and controlled with widely available off-the-shelf components. Finally, the stability of the NV system and the ability to form and manipulate quantum superpositions in a variety of conditions, from low temperature vacuums up to high-pressure, high-temperature environments, make it an ideal candidate for many in-situ demonstrations. However, the NV center not without limitations. The relatively weak ZPL means that most photons emitted by the defect are red-shifted and lose some energy to one or more phonons. Furthermore, NVs have the most advantageous properties in bulk diamond, with coherence times and charge purity decreasing in both nanodiamonds and near the diamond surface due to uncoupled dangling bonds and other surface effects[78].

While these challenges are actively being studied, it is not unreasonable to assume there exist other defect systems without these limitations, either naturally occuring or man-made.[84, 85] The presence of spin-dependent optical mechanics is a generic property of defects in semiconductors which allows initialization and readout of electronic spin state states.[86, 87] Many other host materials and defect systems are being studied, but one broad class of materials which have been of interest are two-dimensional (2D) materials. These materials, which are formed from one or more identical stacked layers, do not have dangling surface

bonds and may exhibit improved coherence times after isotopic purification.[88] Many 2D materials, such as hexagonal Boron-Nitride (hBN), are already well studied and clean, high-purity samples are commercially available. hBN is known to host many defects, some of which are emit radiation in the IR, visible, and ultraviolet regimes. Several defects have recently been shown to host optically detectable magnetic resonance (ODMR) signals[89, 90, 91] and have already been used to sense pressure, temperature, and magnetic fields. [92, 93] One particular defect has been shown to emit light around 2 eV, similar to the NV center, with a high brightness and the majority of the emission being into the ZPL. The emitters have been shown to have magnetic-field sensitive emission[94], a sign of spin-dependent mechanics, and multiple possible configurations for the defect and the associated level structure have been proposed. However, for reasons which are still unknown different examples of what are assumed to be the same defect display widely varying optical properties. This presents a significant challenge in characterizing its properties, since studies have historically used large ensembles of identical emitters to increase the signal to noise ratio when studying new defect systems. The following chapter, taken from a published manuscript, describes a technique we developed to aide in the characterization of heterogeneous emitters such as these and how it can be used to study the effect of material treatments on the emitters' density, brightness, and other properties.

CHAPTER 3

EFFICIENT OPTICAL QUANTIFICATION OF HETEROGENEOUS EMITTER ENSEMBLES

This chapter, along with supplemental material, was published previously in ACS Nano[95]. Reproduced with permission from S. A. Breitweiser et al. "Efficient Optical Quantification of Heterogeneous Emitter Ensembles", ACS Photonics 2020 7 (1), 288-295. Copyright 2020 American Chemical Society.

3.1. Abstract

Defect-based quantum emitters in solid state materials offer a promising platform for quantum communication and sensing. Confocal fluorescence microscopy techniques have revealed quantum emitters in a multitude of host materials. The ability to quickly and accurately sample emitter ensembles is an important tool for characterizing these new quantum emitter systems. In some materials, however, optical properties vary widely between emitters, even within the same sample. In these cases, traditional ensemble fluorescence measurements are confounded by heterogeneity, whereas individual defect-by-defect studies are impractical. Here, we develop a method to quantitatively and systematically analyze the properties of heterogeneous emitter ensembles using large-area photoluminescence maps, summarized in **??**. We apply this method to study the effects of sample treatments on emitters in hexagonal boron nitride, and we find that low-energy (3 keV) electron irradiation creates emitters, whereas high-temperature (850 °C) annealing in an inert gas environment brightens emitters.

3.2. Introduction

As optically addressable spin qubits, defects in solid-state materials have been used to facilitate the storage and transmission of quantum information and precisely sense temperature, strain, and electromagnetic fields at the nano-scale.[87, 96] The most prominent of these defects, such as the nitrogen-vacancy (NV) center in diamond, act as point-source quantum emitters and have a well-understood chemical structure that can be controllably formed in high-purity host materials. Historically, the availability of homogeneous emitter ensembles has been essential for their identification [97, 98] and development for quantum applications

[99, 100]. Using confocal microscopy, however, it is possible to screen many potential host materials for individual quantum emitters. Indeed, quantum emitters have been found in an ever increasing number of materials, including silicon carbide, zinc oxide, gallium nitride, hexagonal boron nitride (hBN), and the transition metal dichalcogenides [101, 84]. In these emerging materials platforms, ensemble studies have proven to be more difficult. Studies are confounded by difficulty synthesizing the host material and controlling its purity, uncertainty about the background impurity levels, unknown chemical structure of the emitters, and often substantial heterogeneity of the emitters themselves. Furthermore, traditional ensemble studies, where average photoluminescence (proportional to density multiplied by brightness) is used to make quantitative comparisons, are not sufficient for such heterogeneous emitters. New techniques are required that can distinguish brightness from density, while still being efficient enough to sample large ensembles across wide field images.

Hexagonal boron nitride (hBN), a two-dimensional (2D) semiconductor with an indirect bandgap of 5.955 eV [102] and a rich taxonomy of defects [103, 104], is a prototypical example. HBN is already an ubiquitous dielectric in van der Waals heterostructures [105], and it is emerging as a versatile platform for nanophotonics [106]. Recent experiments have identified point-like quantum emission at visible to near-infrared wavelengths from hBN [107, 108, 109, 110, 111, 112]. These emitters appear to be robust to the preparation method, having been found in hBN samples of dispersed nanoflakes, exfoliated bulk crystals, and thin films grown by chemical vapor deposition, in thicknesses ranging from monolayer to bulk [113]. The emitters can be spectrally tuned by strain [114] and electric fields [115], and they can be coupled to photonic nanocavities and dielectric antennas which direct and enhance the emission [116, 117]. Some emitters in hBN also exhibit magnetically-sensitive fluorescence at room temperature, indicating the potential for coherent spin control [94].

However, the underlying electronic and chemical structure of emitters in hBN has remained

elusive, partly due to their heterogeneous properties. The brightness, density, polarization, and spectral distribution of emitters varies widely, both between and within samples [111, 108, 109]. Electronic structure calculations have considered multiple defect candidates as possible sources of the emission [118, 119, 120, 104], but none can fully account for the observations. A plethora of treatments — including annealing [107], plasma [121, 122] and chemical [110] etching, irradiation by electrons (both low- and high-energy) [108, 123, 124] and ions [110], strain engineering [125], and ion-beam milling [126] — have been used to create and stabilize emitters. Analyzing the effects of these experiments has so far relied on individually cataloguing large numbers of heterogeneous emitters by hand. However, these studies are prone to sampling bias and have not been able to capture enough emitters to make statistically rigorous quantitative statistical comparisons. Here, we present a versatile and efficient framework for quantifying the optical properties of heterogeneous emitter ensembles from large-area photoluminescence (PL) maps, and we apply it to analyze two common sample treatments in hBN: high-temperature annealing under an inert gas environment and low-energy electron beam irradiation. We found that, in contrast to other well-studied defect-based emitters, low-energy irradiation was sufficient to create new emitters, while annealing primarily brightened existing ensembles without significantly changing their density.

3.3. Model and Analysis

As an example of the type of data we wish to analyze, Fig. 3.1 shows optical and electron microscope images of an hBN flake, as well as PL maps from a suspended region taken before treatment, after electron irradiation, and after subsequent annealing. The pre-treatment map reveals multiple emitters of similar brightness. After undergoing electron beam irradiation, many more emitters are visible, with some now much brighter than others. After annealing, the apparent number of emitters further increases, with the brightest emitters again much brighter than the dimmest. While it is generally difficult to track individual emitters across

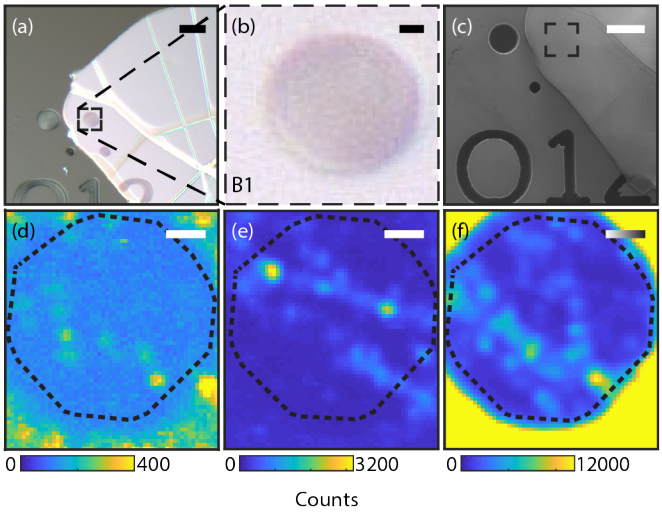

Figure 3.1: a,b) Optical and c) electron microscope images of a flake of hBN on a patterned Si/SiO_2 substrate. The magnified window in (b) is outlined with a dashed line in (a) and shows a suspended region of hBN, labeled as Region B1 later in the text. The same region is outlined again in the electron microscope image (c). Profilometer measurements, available in the Supporting Information, confirm the flake is flat near this region. The lower panels show PL maps of the same region d) before treatment, e) after electron irradiation, and f) after high temperature argon annealing. The suspended region used in subsequent analysis is outlined with a dashed line in (d-f). Scale bars in (a,c) represent 10 µm, while those in (b) and (d-f) represent 1 µm.

treatments, the Supporting Information includes a dataset where certain emitter clusters persisted before and after irradiation, and some isolated emitters appear in the same location with similar dipole orientations before and after annealing.

Rather than attempting to identify and track every emitter in these scans, we fit the data using a model that predicts the statistical properties of heterogeneous point-source emitter ensembles. The procedure distills the map into a distribution of pixel intensities, which is fit to produce an estimate of the density and brightness distribution of emitters present in the region. The model assumes that emitters appear as diffraction-limited point sources with uniform spatial distribution, and with brightness drawn from a weighted mixture of normal distributions. In the following analysis and discussion, we interpret these normal distributions as multiple emitter "families," each characterized by a spatial density, mean brightness, and brightness variance. We stress, however, that this is purely a phenomenological description of the observed emitter distributions; it does not necessarily reflect a classification of the underlying chemical or electronic structure of these emitters.

The model produces a probability density for the intensity of pixels in the region,

$$p(I|\eta_m, A_m, \sigma_m, \lambda) = \overset{M}{\underset{m=1}{\circledast}} \left(\sum_n P_n(\eta_m) p_n(I|A_m, \sigma_m) \right) \circledast \text{Poiss}(I|\lambda)\,, \tag{3.1}$$

where $m \in [1, M]$ labels each emitter family with corresponding density, η_m, average brightness, A_m, and brightness standard deviation, σ_m, while λ parameterizes the brightness of the Poissonian background. $P_n(\eta_m)$ is the probability of having n emitters of family m within the region of interest, and $p_n(I|A_m, \sigma_m)$ is the probability density for pixels as a function of brightness, I, resulting from n emitters from family m. $\text{Poiss}(I|\lambda)$ is the probability density resulting from a Poissonian background with average intensity λ, and $\circledast_{m=1}^{M}$ and $\circledast$ represent convolutions. See the Supporting Information for a derivation of this model, along

with explicit expressions for P_n and p_n. In general, the form of these functions depends on assumptions regarding the emitters' spatial and brightness distribution. We assume a uniform spatial distribution and a normal brightness distribution for each emitter family, but the model can be adapted to any spatial or brightness distribution. The model is probabilistic and ignores spatial information to take advantage of the statistical power of large maps; therefore it does not reveal information about individual emitters, but rather ensemble properties of the collection of emitters present in a sample.

We fit this model to the observed pixel brightness distributions using Differential Evolution [127] to optimize the chi-squared statistic. The number of families, M, is chosen to minimize the Akaike Information Criteria (AIC), which measures fit quality while penalizing overfitting from a high number of families. More details are presented in the Supporting Information.

To test this procedure, we compared the fit results from the model against the parameters of known emitter distributions. Figure 3.2(a) shows a PL map of NV centers in bulk, single-crystal diamond, with a focus plane located approximately 3 µm from the planar, (100)-oriented surface. The laser polarization is aligned to the dominant optical excitation dipole for the NV center at the center of the map. There are three aligned and ten misaligned NV centers in this 400 μm^2 region, with reproducible peak intensities of ≈ 300 Counts (30 kCts/s) and ≈ 120 Counts (12 kCts/s), respectively. These peak intensities include a background of ≈ 10 Counts (1 kCts/s), which appears to be uniform across the map. In addition, some non-point-like emission appears in Fig. 3.2(a), which may result from out-of-focus NV centers or surface contamination.

Figure 3.2(b) shows the histogram of pixel intensities from this map, as well as the result of fitting the model to this distribution. The fitting procedure identifies three emitter families, whose density and brightness parameters are shown in Fig. 3.2(c). Two of these families are

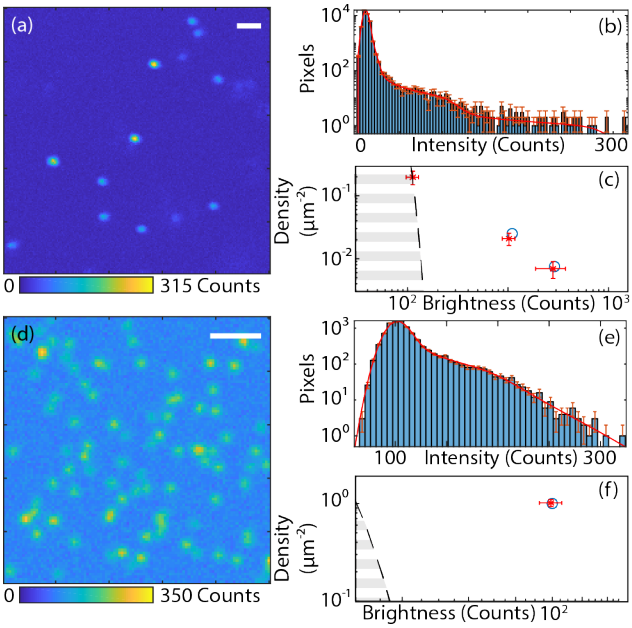

Figure 3.2: Testing the quantitative model. a) PL map of NV centers in single-crystal, bulk diamond. Several NV centers, both aligned and misaligned to the excitation laser polarization, are in focus. b) Histogram of pixel intensities (points) from (a), together with the best fit of the quantitative model (red curve). c) Emitter family parameters (red crosses) corresponding to the best-fit curve in (b). The best-fit background is represented by a dashed curve, bounding a hatched region where the model cannot resolve emitter families from noise. Known values for the density and brightness corresponding to NV centers with different dipole orientations are shown as blue circles. d) Simulated PL map for a single family of emitters based on parameters similar to hBN maps. (e-f) Corresponding pixel intensity histogram, fit, and emitter family parameter plot as in (b-c). The underlying simulation values for the emitter family are indicated by a blue circle. Scale bars in (a,d) represent 2 µm. Error bars in (c,f) represent 95 % confidence intervals.

Region	Thickness	1st Treatment	2nd Treatment
A1	215nm	Low-dose e^- Irr.	Ar Anneal
A2	240nm	Low-dose e^- Irr.	Ar Anneal
B1	390nm	High-dose e^- Irr.	Ar Anneal
B2	250-350nm	High-dose e^- Irr.	Ar Anneal
C1	630nm	Indirect e^- Irr.	Ar Anneal
D1	*	Ar Anneal	Low-dose e^- Irr.†

Table 3.1: Summary of hBN regions and treatment sequences
* Thickness information is not available for this region.
† The radiation dose in this region was $4 \times 10^{15}\,e^-/cm^2$.

within one standard uncertainty of both the density and brightness of the aligned and misaligned NV centers identified in the map, after accounting for the background. In addition, the best-fit background of 10.064(92) Counts is close to the ≈ 10 Counts measured by eye from the PL map, and is represented in Fig. 3.2(c) by a dashed curve in brightness/density space. For values of brightness and density below this curve, the model cannot reliably distinguish emitter families from noise. One additional emitter family appears close to the noise floor in Fig. 3.2(c); this may arise from weak, non-point-source PL features in the map.

The low density and reproducible brightness of NV centers in diamond make maps like Fig. 3.2(a) easy to interpret by eye. A simulated dataset with less ideal conditions, similar to the hBN PL maps of Fig. 3.1(d-f), is shown in Fig. 3.2(d). Here the density of emitters is much greater, such that some emitters overlap and are indistinguishable by eye, and the brightness of emitters has a wide distribution. In addition, the background intensity is comparable to the brightness of emitters. Nevertheless, the fitting procedure captures the pixel intensity distribution well, and the analysis yields a single emitter family with parameters that agree with the underlying simulation parameters, as shown in Fig. 3.2(e,f). Similar analyses for multiple emitter families are presented in the Supporting Information.

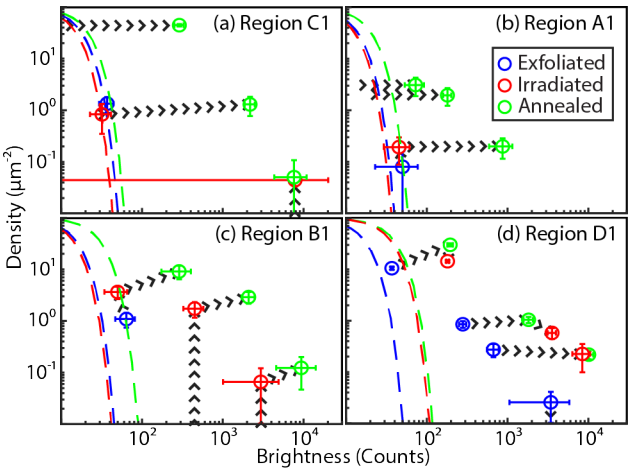

Figure 3.3: Best-fit parameters after each treatment stage for four representative hBN regions from Table 3.1. The estimated density and brightness of each emitter family is represented as a circle in blue (pre-treatment), red (post-irradiation), or green (post-annealing) based on which stage of the treatment process the flake is in. Note that Region D1 in (d) was annealed prior to irradiation, whereas all other regions were irradiated first. Arrows indicate potential evolution of these emitter families from the treatment process, based on qualitative observations. A noise floor, determined by the best-fit background for each map, is displayed as a dashed line and determines the lower limit for detecting emitter families. Error bars represent 95% confidence intervals in the best-fit parameter values.

3.4. Results

A list of hBN regions studied in this work, as well as the treatments applied to them, is presented in Table 3.1. See Methods for details of sample preparation, treatments, and data acquisition. PL maps from each region for each stage of treatment were analyzed using our model; regions were imaged under identical conditions in each stage. The fitting results from four representative regions are presented in Fig. 3.3 and discussed below. Raw PL map data, optical microscope images of the hBN samples, as well as analysis of additional regions are available in the Supporting Information.

We first consider the effect of electron irradiation. Region C1 received no direct exposure to the electron beam, although it was present in the instrument chamber to measure effects of the ambient chamber conditions. As shown in Fig. 3.3(a), this region saw a small decrease in

the density of pre-existing emitters, although it was within the uncertainty of the fits. Some decrease is expected due to photobleaching from successive scans. In addition, the appearance of a single bright emitter resulted in the detection of a new family with high brightness and low density; we tentatively attribute this isolated event to stray ions accelerated in the column. Regions A1 and B1 received low and high doses of direct electron irradiation, respectively. Region A1 saw a small increase in the density of its pre-existing emitter family, although the increase was within the fit uncertainty; see Fig. 3.3(b). The high-dose region B1 considered in Fig. 3.3(c) is the same one presented in Fig. 3.1; it showed a significant increase in the density of its pre-existing emitter family, along with the appearance of two new families of higher brightness.

Regions A1, B1, and C1 were all annealed after irradiation, under the same conditions as described in Methods. Looking at the fit results for region B1, there are three emitter families both before and after annealing, with approximately the same densities but systematically higher brightnesses. The simplest interpretation of these results is that each family became brighter without a significant change in density. Analysis of regions A1 and C1 also uncovered post-annealing families with similar density to pre-existing families but with higher brightness, consistent with this interpretation. However, these regions also contained new dim, dense emitter families after annealing. Considering the relative change in brightness for pre-existing emitter families, we propose that these emitters existed before annealing, but were below the noise floor — only becoming bright enough to be captured by the model after annealing. No new families are detected after annealing for the high-dose Region B1. However, the dimmest family saw a density increase at the edge of statistical significance, and the background showed a large increase not seen in the low-dose or non-irradiated region. Both of these features could be indicative of a dim, dense family that cannot adequately be resolved in the data. In Fig. 3.3, we indicate the possible evolution of emitter families under

annealing *via* dashed lines.

Region D1 was first annealed, followed by a low dose of irradiation; its analysis is shown in Figure 3.3(d). The pre-treatment analysis detects four families of emitters already present in the region; we attribute the greater number of pre-treatment emitter families here to alternate sample preparation, as this flake was exfoliated from a different bulk crystal and underwent a post-exfoliation O_2 plasma clean. Recent studies have shown plasma treatments may create new emitters [121, 122]. After annealing, the brightest family, which consisted of a single emitter, disappeared, which we attribute to photobleaching. The other three families can be seen to increase in brightness again. Similar to region B1, the dimmest emitter family also saw a slight increase in density, and the background saw a large increase. After irradiation, the emitter parameters did not exhibit a significant change. This is consistent with the results for Region A1, which also received a low irradiation dose; the expected increase in emitter density is small compared to the large densities already present in Region D1 after annealing.

In order to compare results from different regions, and to generate a more rigorous statistical understanding of the treatment effects, we consider the full emitter brightness distribution extracted from the analysis of each region. The brightness distribution of emitters is obtained by summing the individual contributions of each family weighted by their densities, $\sum_m \eta_m \mathcal{N}(I|A_m, \sigma_m^2)$, where $\mathcal{N}(I|A, \sigma^2)$ is a normal distribution on I with mean A and variance σ^2. However, due to the wide range of brightnesses observed, the results are best shown on a logarithmic brightness scale. Thus, we present the results as a log-space probability density,

$$\Lambda(I) = I * \sum_m \eta_m \mathcal{N}(I|A_m, \sigma_m^2)\,, \tag{3.2}$$

where the additional factor of I accounts for the logarithmic spacing of brightnesses, cor-

recting the visual weight of the plotted distribution.

Figure 3.4 shows this distribution for regions which received irradiation followed by annealing. In the pre-treatment distributions of Fig. 3.4(a), we observe a localized peak around 50 Counts ($\approx$ 400 Cts/s), with very few emitters brighter than 1000 Counts ($\approx$ 8 kCts/s). Any emitters with brightness below $\approx$ 30 Counts cannot be resolved from the background noise (indicated by dashed lines). Figure 3.4(b) shows the same regions after irradiation. We observe a much larger peak around 70 Counts, as well as new peaks appearing with higher brightness. Finally, the post-annealing distributions shown in Fig. 3.4(c) are much broader, with emitters found from the noise floor of $\approx$ 30 Counts to $\approx 10^4$ Counts ($\approx$ 800 kCts/s).

To better visualize the treatment effects, Fig. 3.4(d,e) present the difference between the distributions before and after irradiation and annealing, respectively. We observe from Fig. 3.4(d) that irradiation produced an almost uniform increase in the density of emitters, and regions B1 and B2, which received larger doses, saw larger density increases than regions A1 and A2. Annealing showed a qualitatively different effect, with densities decreasing at lower brightness and increasing at higher brightness in Fig. 3.4(e). There is a small overall increase in density; this, as well as the overall broadening of the distribution, can tentatively be attributed to the dim, dense emitters that might be below the noise floor in pre-annealing fits.

3.5. Discussion

3.5.1. Irradiation

In agreement with qualitative observations of images such as those in Fig. 3.1 and with the observations of earlier studies [123, 108, 128], our quantitative analysis shows that low-energy electron irradiation increases the emitter density, creating emitters of low-to-intermediate brightness. However, the underlying mechanism for emitter creation due to electron-beam

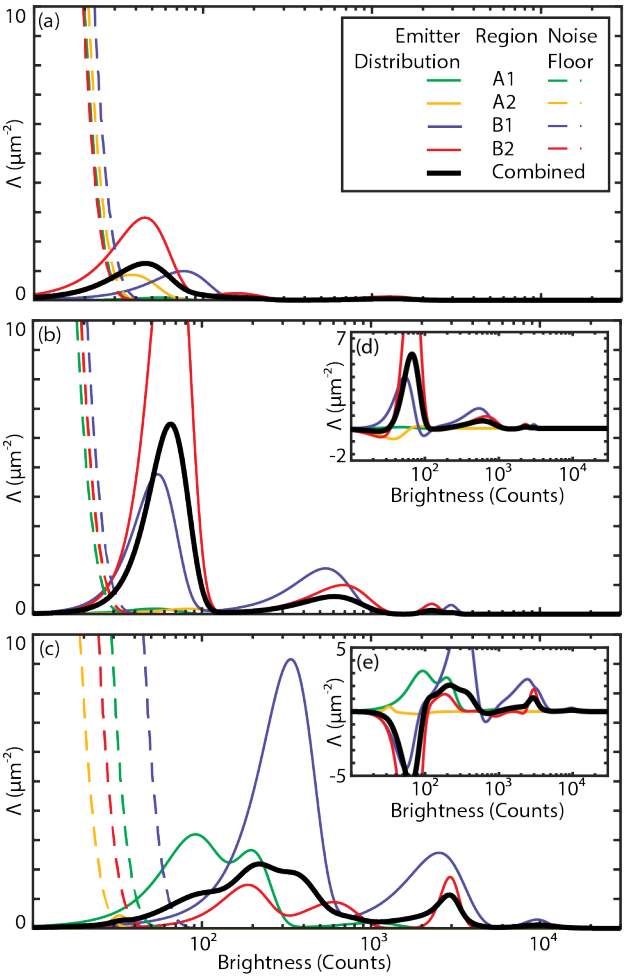

Figure 3.4: Emitter brightness distributions for regions which received direct irradiation prior to annealing; distributions for each region a) before treatment, b) after irradiation, and c) after annealing are plotted as thin colored curves for each region as indicated in the legend, with the combined distribution for all regions shown as a thick black curve. Dashed curves indicate the background noise floor for each region. Inset panels (d) and (e) show the changes in the distributions from pre-treatment to post-irradiation and post-irradiation to post-annealing, respectively. Note that, since the brightness is shown on a logarithmic scale, the log-space probability density is shown; refer to the main text for details.

irradiation remains unknown. For comparison, typical methods to create NV centers in diamond use electrons of sufficient energy to create vacancies in the lattice, with subsequent annealing treatments to combine them with nitrogen defects to create NV centers. In contrast, the electron energies used here are much lower than the minimum knock-on energy for creating monovacancies in hBN [129], corresponding to an accelerating voltage of 80 kV. One possibility is that stray ions accelerated in the chamber, which would have sufficient energy to create vacancies, are creating these new emitters. Using a similar irradiation procedure, however, Vogl *et al.* found emitters are created uniformly in samples thinner than the stopping range of the electrons, which is on the order of a micron for the 3 keV energy of our electron beam [128]. Ions at this energy would only travel a few nanometers into the hBN, and they would appear independently of beam exposure. Combined with our observation that the number of emitters created increases with electron dose, this argues for a creation mechanism based on interactions between the electrons and hBN, rather than accidental implantation of impurity ions in the SEM chamber. The electrons might have sufficient energy to perturb the placement of interstitial atoms, or to cause reconstruction of edges or extended defects. This interpretation could support a recent proposal that dangling bonds on hBN edges are responsible for quantum emission in this material [130]. Alternatively, charge trapping may cause emitter activation, as suggested in previous studies [125, 131]. Irradiation could reconfigure the charge state of existing defects, converting them into a fluorescent configuration, or the reconfiguration of nearby charge traps could alter the (non)radiative relaxation pathways relevant for the visible PL.

3.5.2. Annealing

Similarly, the role of annealing on hBN's quantum emission is poorly understood. For comparison, annealing is used in diamond to increase the mobility of lattice vacancies, which combine with substitutional nitrogen atoms to create NV centers. Whereas qualitative as-

sessment of PL maps like those in Fig. 3.1 gives the impression that annealing also creates emitters in hBN, our quantitative analysis indicates that the primary ensemble effect of annealing is to brighten existing ensembles without significantly changing the density of emitters. The brightness increase by annealing is around one order of magnitude regardless of the emitters' original brightness — a surprising result given that the emitter brightnesses span several orders of magnitude. Some regions also saw the appearance of dim, dense emitter families after annealing; even for regions where such families were not detected, a larger increase in the background intensity and in the density of pre-existing families point to the possibility of dim emitters that were subsumed into the background and excluded from our analysis. Assuming these dim emitters were also brightened by annealing, it is possible they were present before annealing, but not detected because they were below the noise floor.

The brightness enhancement could be explained by an increase in the emitters' quantum efficiency. Potentially, annealing affects the concentration of other, non-emissive defects in the sample, which modify non-radiative decay pathways for the emissive defects. This interpretation is supported by the varied quantum efficiencies for hBN emitters reported in the literature, which range from 6% [117] to 87% [132]. This could also explain why the brightness increase is consistently around an order of magnitude, regardless of the initial brightness of the emitters.

While a systematic increase in brightness due to annealing is the simplest interpretation of our observations, we cannot rule out all other potential effects. Studies using rapid thermal annealing rather than a tube furnace saw an increase in zero phonon line intensity, and noted that longer annealing times led to spatial diffusion of emitters [122]. Such diffusion, combined with the increased brightness of emitters, could give the appearance of bright emitters being created simultaneously with dim emitters being destroyed. The mobility of point defects or impurities in the lattice during annealing might explain these effects, either by moving the

underlying defects or otherwise modifying the emitters' chemical structure. Of the single-atom vacancies and interstitial defects, only boron vacancies are expected to become mobile around 800 °C, with nitrogen vacancies requiring temperatures in excess of 1500 °C and interstitial defects becoming mobile near room temperature [104]. This framework presented here could be used to study the temperature dependence of annealing effects, for comparison with theoretical calculations of the onset of defect mobility for different species.

3.6. Conclusion

We presented a method to efficiently assess the optical properties of statistically large heterogeneous quantum-emitter ensembles. Tracking systematic variations between samples or between treatments offers quantitative insight into the mechanisms at play. In the case of hBN, electron irradiation provides an accessible and controllable method for creating emitters in otherwise dark samples. For samples with dim emitters, annealing may provide a way to brighten emitters.

While this study focused on the brightness and density of emitters, the model can also be expanded to capture other properties of quantum emitters, such as their dipole orientation and spectral distribution. Previous work studied the alignment of emitter dipole orientations to the crystallographic axes of hBN [109]. By extending our model to include polarized emitter families and comparing to polarization resolved data, we could leverage the statistical power of much larger emitter ensembles to study the distribution of dipole orientations. A similar extension of our model could account for the emitters' spectra; including spectrally resolved data could reveal phenomena such as zero phonon line clustering, which has been observed in multiple recent studies [133, 134, 135]. By adapting the underlying spatial probability distribution functions, the model can be further extended to account for emitters clustering near edges or other extended defects.

This methodology can be applied to any material hosting point-source emitters, including dispersed nanoparticles and fluorescent molecules. It is is particularly relevant for 2D materials, where heterogeneity is prevalent and advances in fluorescence imaging have enabled the efficient acquisition of emission maps from large sample regions. Such wide-field techniques have been used to study the role of annealing temperatures on NV center quenching and formation [136], as well as to study the spectral and temporal properties of emitters in hBN [135, 134]. However, these studies relied on algorithms designed to identify and track individual emitters, which cannot handle significant heterogeneity between emitters and are expected to fail at high emitter densities and low emitter brightnesses. Combining these wide-field imaging techniques with the approach presented here paves the way to efficiently and accurately screen large ensembles of heterogeneous emitters, an important step for the identification and study of new platforms for defect-based quantum technologies.

3.7. Methods

Flakes of hBN were exfoliated from bulk single crystals (HQ Graphene) onto patterned Si wafers with a 90 nm layer of thermal SiO_2 on top. The flakes hosting regions A1-A2, B1-B2, C1-C3, and E1 were first exfoliated onto a polydimethylsiloxane (PDMS) stamp, and then transferred onto the silicon substrate at a temperature of 50 °C. The flakes hosting regions D1-D3 were prepared following the method in Refs. 109 and 94, and further underwent an O_2 plasma clean in an oxygen barrel asher (Anatech SCE 108). Flake thicknesses were measured using a stylus profilometer, and ranged from $<$100 nm to $>$600 nm, with most flakes falling between 200 and 400 nm. Of particular interest are regions which are suspended over holes etched into the substrate ($>$6 µm deep), where emitters show a greater contrast with the background and better isolation from substrate-dependent effects.

Suspended regions were identified using an optical microscope and alternately exposed to a 3keV electron beam (FEI Strata DB235 FIB SEM) and annealed in a tube furnace under

flowing Argon gas. The electron beam was rastered over a known area, with the dosage calculated from the area size and the approximate beam current. Low-dose irradiated regions, with the exception of D1, received fluences on the order of $2 \times 10^{16}\,\mathrm{e^-/cm^2}$, while high dose regions received approximately $2 \times 10^{17}\,\mathrm{e^-/cm^2}$. Region D1 received a dose of $4 \times 10^{15}\,\mathrm{e^-/cm^2}$. Calculated fluences for all regions are available in the Supporting Information. The annealing ramp rate was set to $10\,^\circ\mathrm{C\,min^{-1}}$, leading to a heat-up period of $\approx 1.5\,\mathrm{h}$ to reach 850 °C. Once 850 °C was reached, the temperature was maintained for 30 minutes, after which the sample was allowed to cool back to room temperature over the course of several hours. Argon gas was flowed from before heating until after cooling the sample to ensure complete evacuation of other gasses from the chamber while the sample temperature was elevated.

Samples were mounted in a home-built confocal fluorescence microscope, where PL was stimulated with a 592 nm continuous wave laser (MPB Communications, VFL-592) and collected between 650 and 900 nm. For this study, the pre-objective power was fixed to $\approx 500\,\mu\mathrm{W}$ and the laser polarization was rotated using a half waveplate (Newport 10RP12-16) and corrected for birefringence. PL maps were recorded for each region with multiple laser polarizations and registered, then added together to create a polarization-independent PL map. Maps were acquired for each region at each stage of the treatment process and compared to a point emitter model, as described in the main text, to determine the underlying microscopic parameters.

For the NV-center reference scan in Fig. 3.2(a), an electronics grade type IIa synthetic diamond from Element Six was irradiated with 2 MeV electrons at a fluence of $10^{14}\,\mathrm{e^-/cm^2}$ and then annealed in forming gas at 800 °C for 1 hour. The diamond sample was mounted in another home-built confocal fluorescence microscope. A 532 nm continuous wave laser (Gem 532, Laser Quantum) was used to optically excite the NV centers and fluorescence was collected with a 650 nm long-pass filter. Polarization was similarly varied using a half

wave plate and the pre-objective laser power was set to 500 µW.

A layer of NV centers was found approximately 3 µm from the diamond surface, and the confocal depth was set to focus on the NV at the center of the scan in Fig. 3.2(a). The laser polarization was set to maximize the PL from the central NV center. Due to the geometry of NV centers beneath a (100) diamond surface, all other NV centers in the sample are either aligned or misaligned to the excitation axis by the same angle.

3.8. Acknowledgement

The authors thank R. Grote for assistance with electron-beam irradiation. This work was supported by the National Science Foundation (DMR-1922278) and the Army Research Office (W911NF-15-1-0589). We gratefully acknowledge use of facilities and instrumentation at the Singh Center for Nanotechnology supported by the National Science Foundation through the National Nanotechnology Coordinated Infrastructure Program (NNCI-1542153) and Penn's Materials Research Science and Engineering Center (DMR-1720530).

3.9. Supplementary Info

Additional supplementary info is available in **??**. This includes: Profilometer measurement near region B1; PL maps of region B2 with persistent emitter identified; details of the emitter model used for fitting; additional simulation results; table of regions with additional information; additional emitter distributions obtained; full photoluminescence datasets with fit results.

CHAPTER 4

EXPERIMENTAL METHODS

The types of experiments we are interested in require a carefully orchestrated combination of optics, microwave electronics, and timing equipment to run successfully. Here, we describe the hardware and software solutions developed in the lab to enable such experiments and used in the remainder of the work presented in this thesis.

4.1. Experimental setup

The optics and sample preparation procedures are similar to those described in [137]. A sample of electronics grade type IIa diamond (Element Six) was irradiated with 2 MeV electrons ($\approx 10^{-14}\text{cm}^{-2}$ dose) and annealed at 800 °C for one hour in forming gas. A suitable NV with no strong carbon-13 nuclear couplings was identified several microns below the surface and a Solid Immersion Lens (SIL) centered on this NV was milled out of the diamond surface using focused ion beam milling. A gold/titanium circular antenna was deposited on the diamond surface, centered around the SIL using lithographic techniques, and wirebonded to a custom PCB used to mount the sample and couple to external microwave electronics. Unless otherwise noted, all of the experiments presented in the remainder of this thesis were performed on the NV at the center of this SIL. Other NVs, such as those used in Chapter 6, were identified along the antenna and traces - while the excitation and collection efficiency are not as high since they are not within a SIL, they are still close enough to the antenna to observe coherent oscillations.

This sample was mounted into a home-built confocal microscope which uses a 532 nm laser (Gem 532, Laser Quantum) gated by an Acousto-optic Modulator (AOM) in a double pass configuration to produce green illumination. The laser beam passes through a servo-mounted optical density (OD) wheel which allows broad control over the intensity, before going through a $4f$ lens pair and being reflected off a fast steering mirror (FSM, Optics in Motion OIM101) before passing into a free space high-NA objective (Olympus, MPLANFLN 100x). The sample can be moved into rough alignment with the objective using comput-

erized stages (Thorlabs) and the laser beam can be steered using the FSM for fine spatial control of the illumination. Photoluminescence (PL) from the sample is collected through the same objective, and is separated from the excitation light using a dichroic mirror (Semrock, BLP01-P01-635R) before being focused into a fiber and passed to a single-photon avalanche diode (SPAD, Laser Components, Count-20C-FC). The detection signal of the SPAD is passed through a pair of switches which can either route to a 50-ohm termination or one of two counters of a data acquisition device (DAQ, National Instruments, DAQ6323) to be recorded.

A rare-earth permanent magnet is mounted by hand in the setup and aligned along the NV axis to provide an on-axis magnetic field which separates the spin states. Depending on configuration, the magnetic field can range from $\lesssim 50\,\text{Gauss}$ to $\gtrsim 250\,\text{Gauss}$.

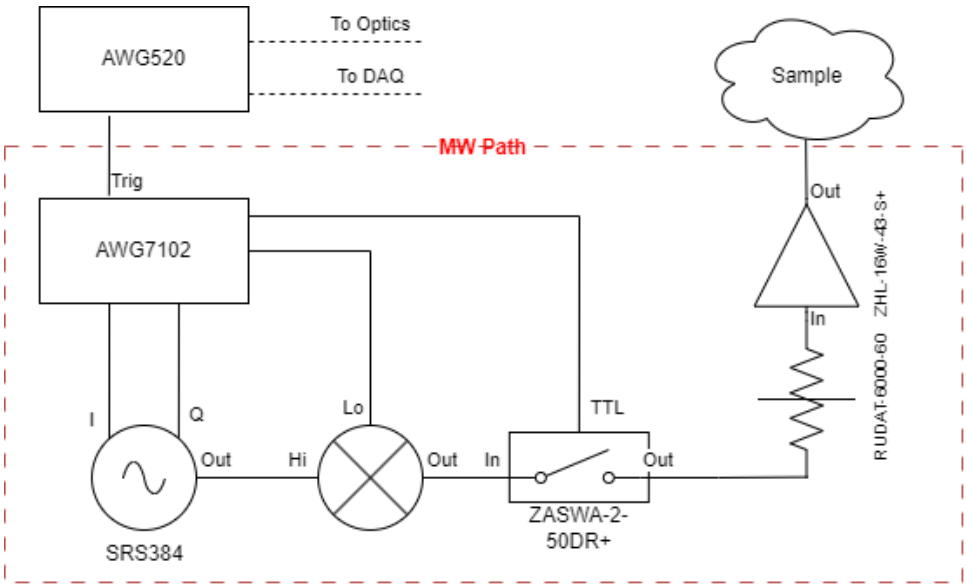

Figure 4.1: Electronics along the microwave path. Two analog signals from an AWG (AWG7102 Tektronix) are used to control the IQ modulation of a benchtop signal generator (SG384, Stanford Research Systems) which is fed into a mixer (ZX05-63LH+, Mini-Circuits), which allows sharp pulses not limited by the $\approx 200\,\mathrm{MHz}$ IQ modulation bandwidth of the signal generator. The output from the mixer is sent through a high-isolation switch (ZASWA-2-50DR, Mini-Circuits) also controlled by the AWG7102. The output was fed through a USB-controlled microwave attenuator (Rudat 6000-60, Mini-Circuits) and broadband amplifier (ZHL-16W-43-S+, Mini-Circuits) before being delivered into the sample through a custom SMA-connected PCB which is in turn wirebonded to the antenna traces.

The experiment is controlled by a pair of Arbitrary Waveform Generators (AWGs). One AWG (AWG520, Tektronix) controls the overall flow of the experiment and the optical path described above, including the AOM, the DAQ and the switch network used to record PL counts. The AWG520 also triggers a higher-resolution, larger memory AWG (AWG7102, Tektronix) which controls the generation of microwaves signals sent to the sample. The circuit used to generate the microwave signal is shown in Fig. 4.1. The analog outputs of the AWG7102 are connected to the IQ modulation of a microwave signal generator (SG384, Stanford Research Systems). To allow pulses faster than the $\approx 200\,\mathrm{MHz}$ bandwidth of the IQ modulation of the signal generator, the output is sent into the HI port of a fast RF mixer (ZX05-63LH+, Mini-Circuits) with a $1\,\mathrm{GHz}$ bandwidth, with the LO port controlled by a

digital output of the AWG7102. The output is sent through a high-isolation switch (ZASWA-2-50DR, Mini-Circuits), controlled by the AWG7102 using TTL logic, which prevents on-resonance leakage signals from reducing the coherence of the spin systems. The output of the switch is sent through a USB-controlled microwave attenuator (Rudat 6000-60, Mini-Circuits), allowing global control of the microwave power, before being amplified (ZHL-16W-43-S+, Mini-Circuits) and sent to the sample.

4.2. Experiment Timing

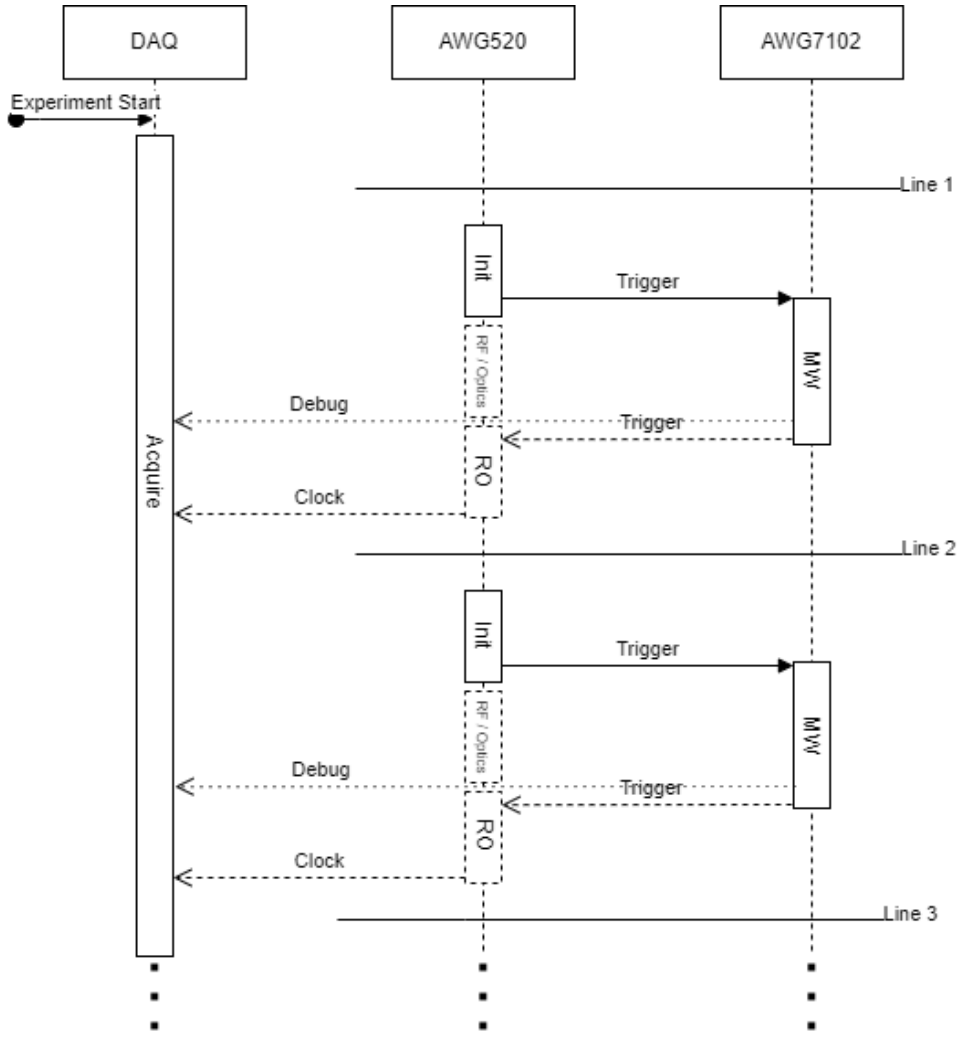

Figure 4.2: (a)Diagram showing the timing of experiments. Experiments are broken into lines, each of which contain an initialization, control, and readout phase. During the initialization phase, the AWG520 plays the optical sequence used to reset the defect spin system and triggers the AWG7102. During the control phase, the AWG7102 plays the microwave sequence used for coherent control of the electron spin. Optionally during the control phase the AWG520 can continue to play optical and radio-frequency sequences, and the AWG7102 can send debugging information using pulses into one of the DAQ counters. Finally, the (optional) readout phase is either triggered by the AWG7102 or the AWG520 simply waits the appropriate amount of time to begin readout. During this phase, the AWG520 plays the optical sequence necessary to readout the electron spin, and clocks the DAQ to record the state of the current counters - including those used to measure the photoluminescence from the photodetector(s) as well as the debugging counter.

Fig. 4.2 shows a diagram of the general timing sequence used for experiments. Three main pieces of equipment are involved in experiment timing: a DAQ, an AWG520, and an AWG7102. The DAQ collects signals using counters, including both the photoluminescence data from the photodetecor as well as any debugging signals from the AWGs. The AWG520 controls the general flow of the experiment, as well as the optical path components and generating any RF signals required. The AWG7102 generates microwaves (if necessary) and controls the components on the microwave path. The DAQ begins acquiring at the beginning of the experiment, and data is read out asynchronously by a remote computer. While it is acquiring, signals are only routed to the DAQ when the switches, controlled by the AWG520, are in the correct state. Both AWGs are preloaded with all the waveforms and sequence specifications for the experiment. A description of the package used to generate these waveforms is laid out below.

Experiments are generically broken into lines, each of which contains three phases: initialization, control, and readout. During the initialization phase, the AWG520 plays the optical sequence necessary to initialize the defect system in the desired manner. For example, this could be a steady state initialization - a longer green laser pulse used to reset the electronic spin and any coupled nuclear spins - or just an electronic reset - a shorter green laser pulse designed to reset just the electronic spin. During this phase, the AWG520 maintains the switches in the correct state so counts from the photodetector do not get routed to the DAQ and are not counted as part of the experimental signal. Following the initialization phase, the AWG520 triggers the AWG7102 to begin the control phase. During this phase, the AWG7102 plays the microwave sequence necessary for coherent control of the electron. The AWG7102 can also send optional debugging information to the DAQ using pulsed signals, which will be reported back to the remote computer. Also during this phase, the AWG520 can optionally play optical and/or RF sequences concurrently with the microwave sequence.

Finally, the (optional) readout phase is either triggered when the AWG7102 sends a trigger back to the AWG520 or when an appropriate amount of time has passed for the microwave sequence to play. During the readout phase, the AWG520 generates the optical sequence necessary to readout the state of the electron spin. For example, this could be a typical PL readout - a single green laser pulse - or a readout using SCC - which uses a combination of green, orange, and red lasers to convert the spin state of the electron into a charge state of the NV and then subsequently reads out the charge state (as described in [81, 138]). Crucially, during this phase the AWG520 also controls the switches so that counts from the photodetector are only directed into the DAQ when the readout pulses are being applied. Finally, the AWG520 sends a signal to the DAQ to recored the current state of the counters (known as a "clock") and advances to the next line.

Every line can have a separate waveforms for each of the initialization, control, and readout phases. The correct waveforms for each of these can be generated using a home-built software package we describe now.

4.3. Sequence generation package

To modularize the generation of necessary files and enable a high level description of experiments, we created a new python package, named qel_seq_gen. Here we describe the relevant modules and their functionality.

4.3.1. Pulses Module

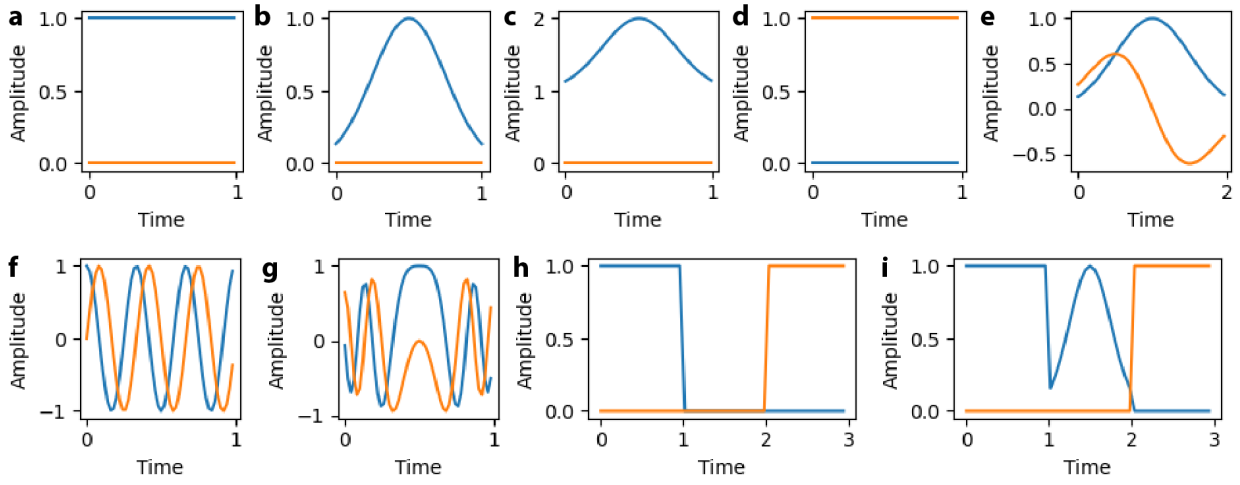

Figure 4.3: All plots are formed by sampling the Pulses or PulseSchedules at a high rate between 0 and the duration. In all plots, blue represents the real or in-phase (I) component of the signal and orange represents the imaginary or quadrature (Q) component. (a) A ConstantPulse of amplitude 1 and duration 1. (b) A GaussianPulse of amplitude 1, sigma 0.25, and duration 1. (c) A CompositePulse formed from adding the two previous pulses together. (d) An IQPulse formed by shifting the phase of the first pulse by $\frac{\pi}{2}$. (e) A FunctionPulse using a DRAG pulse, showing the ability to use arbitrary complex-valued functions. (f) A DetunedPulse, with detuning of 3 Hz. (g) A ChirpedPulse, using hyperbolic chirping. (h) A PulseSchedule formed by concatenating the I and Q ConstantPulses, with a special DelayPulse in between. (i) Pulses can also be added at arbitrary times during the PulseSchedule. Here a GaussianPulse was added in between the ConstantPulses of the last PulseSchedule. Amplitudes will add as complex numbers where pulses overlap.

To begin, we start with an abstract class known as Pulse. All members of the Pulse class must have a duration property, which defines the amount of time between the beginning and end of the Pulse, as well as a sample method, which takes as input a vectorized list of times between 0 and duration and returns the (complex) value of the pulse amplitude at that point. The real value of the function is interpreted as the in-phase amplitude of the pulse signal, while the imaginary value is the quadrature amplitude. We show several useful examples of such Pulses in Fig. 4.3. Fig. 4.3(a) shows a ConstantPulse, which has constant amplitude during its duration, while Fig. 4.3(b) shows a GaussianPulse, which

gives a gaussian pulse centered within the duration with a specified amplitude and width. Fig. 4.3(c) shows a CompositePulse, which adds two pulses together pointwise, formed from the previous two pulses. Fig. 4.3(d) shows an IQPulse, which takes an existing pulse and shifts the phase, formed from a square pulse shifted by $\frac{\pi}{2}$ radians. Fig. 4.3(e) shows a more general FunctionPulse, which can use any function that returns a complex value at any point between 0 and the Pulse duration. In this case we use it to define a Derivative Removal by Adiabatic Gate (DRAG) pulse, which is used in some quantum computing architectures to correct for pulse errors. Finally, we can also produce detuned and chirped pulses, which are demonstrated in Fig. 4.3(f) and (g), respectively.

Pulses can be concatenated to form a PulseSchedule, such as shown in Fig. 4.3(h), using a special DelayPulse (which is defined to have amplitude 0) to space apart two ConstantPulses of different phases. Pulses can also be added at any arbitrary time (given by the start of the Pulse) in the PulseSchedule - Fig. 4.3(i) shows the result of adding a GaussianPulse in between the two ConstantPulses. If Pulses overlap, their (complex) amplitudes are added pointwise. Like the Pulses themselves, the PulseSchedules also define a duration function (which goes from 0 to the maximum value of any pulse duration plus its starting time), as well as a sample, which returns the complex value for all the active Pulses at any given time between 0 and the PulseSchedule duration.

4.3.2. Waveforms module

A waveforms module is defined to handle tasks related to digitizing these abstract pulses. A waveform is an evenly spaced sampling of an abstract Pulse or PulseSchedule. The waveforms module defines functions used to justify these waveforms, as well as window them out for electronics such as switches and IQ modulation which require a finite rise time.

4.3.3. AWG_objects and AWG_prep modules

The awg_objects and awg_prep modules contain the classes and helper functions, respectively, used to compile waveforms into the format needed to load into the AWG7102 and AWG520. The relevant classes are AWGWaveform and AWGPattern, which tell the AWG what values to put out at each sample period, and AWGSequence, which handles the files used to specify which order to play the AWGWaveforms and AWGPatterns in. All of these are saved to binary file formats used by the AWGs and loaded before the experiment begins.

4.3.4. Experiments module

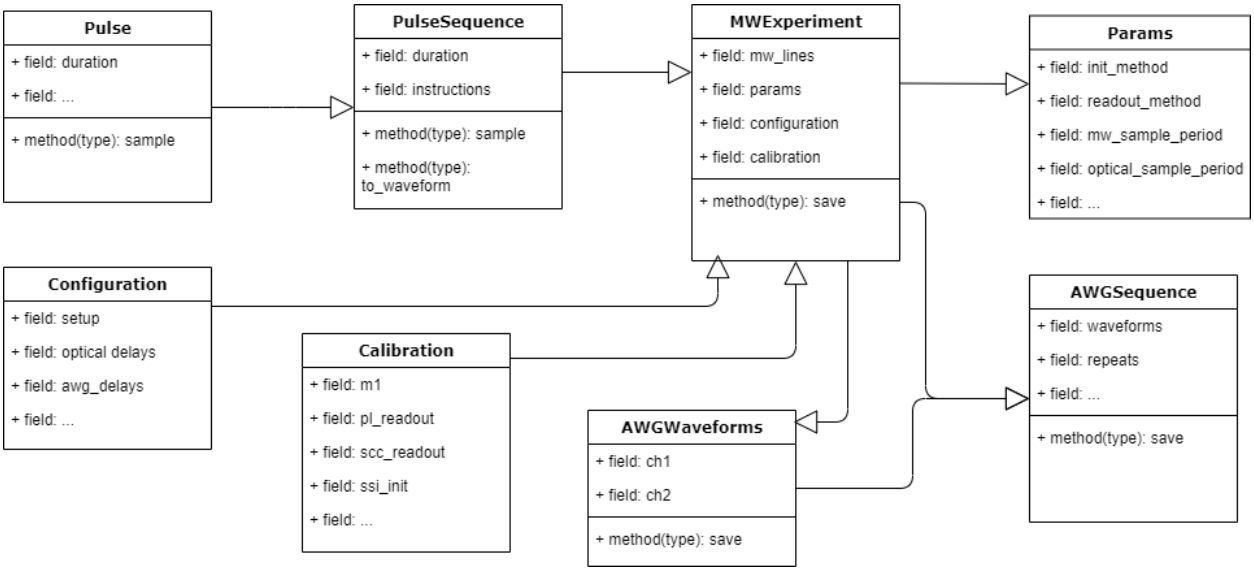

Figure 4.4: Abstract Pulses combine together to form a PulseSequence which is used to specify the microwave control of a defect. Multiple such lines are used to calibrate, initialize, and experiment on the system as part of the MWExperiment class. The MWExperiment uses calibration and configuration information saved in yaml files, as well as user-supplied information in the params structure (which is also saved as a yaml file along with the output files). The MWExperiment class outputs AWGWaveform/AWGPattern files, which specify the waveforms output by the AWGs, as well as AWGSequence files, which describe the sequence in which to play the waveforms, in special binary formats compatible with the AWGs.

Finally, the Experiments module contains the high level classes used to define the experimental sequences used. The class used in most of our experiments, called MWExperiment, describes a sequence of microwave control lines that will be applied to an initialized system which will be measured afterwards. A MWExperiment takes in a list of PulseSchedules which are to be played on a microwave carrier tone, such as those used to control the NV electron spin, and inserts them in between initialization and readout sequences. There are three such types of lines: calibration lines, initialization lines, and experimental lines. Fig. 4.5 shows the way these lines are interleaved to form an experiment. Experimental lines represent the sequences we wish to measure the effect of, typically some form of sweep, and are run in an interleaved mode - where each line is run and the result measured once before the whole sequence is repeated. Alternatively, the experimental lines can be run in batches, where many lines are run in an interleaved "batch" before moving on to the next batch of lines. This is useful in situations such as long sweeps where the AWGs do not have enough memory to hold all the necessary lines at once, or where the experimenter wants to make informed decisions based on the result of one batch whether to run the next. Before each experimental line is run, the initialization line(s) are run - which can accomplish things such as initializing the nuclear spin environment. Typically initialization lines do not include readout, and they can be run multiple times in an interleaved manner. Finally, calibration lines are run before every sweep of the experiment lines (or every batch if using batched mode). These take care of calibrations for slowly varying properties such as the electron readout PL, and are important for getting consistent signals that can be compared across experiments. Calibration lines can be run with or without the initialization lines beforehand. Since the calibration lines are often much shorter than experimental lines, it is usually advantageous to run them multiple times to remove as much systematic noise from the signal as possible.

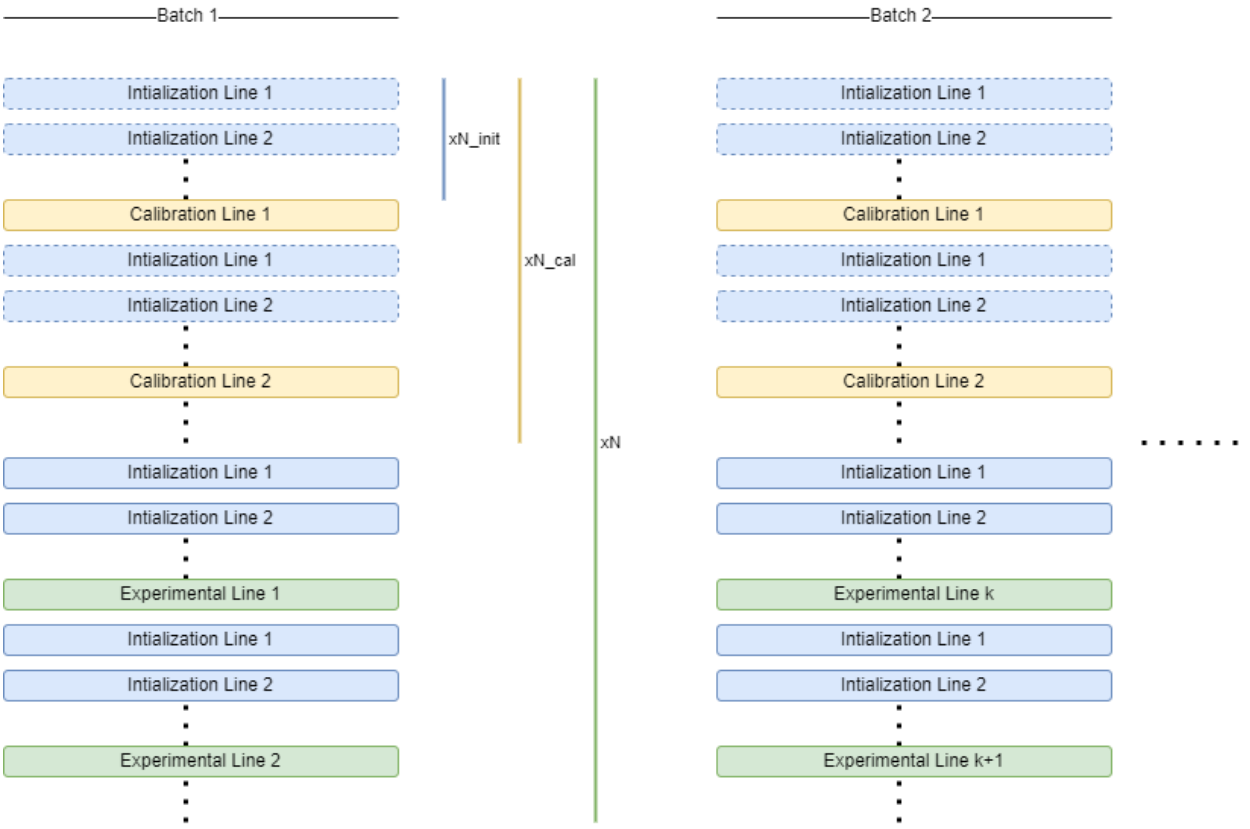

Figure 4.5: Initialization lines, which can be repeated an arbitrary number of times in an interleaved manner, are run before every experimental line and optionally before every calibration line. These lines do not include readouts and are used to, for example, initialize nuclear spins. Calibration lines are used to calibrate slowly varying parameters such as the electron spin readout, and are repeated an arbitrary number of times before the experimental sweep to remove systematic uncertainties in our system. Finally, experimental lines are used to study the system, often in the form of a sweep. Experimental lines can be broken up into multiple batches to prevent overloading the AWG memory, or if the experimenter wants to study the results of one batch before deciding to measure the next.

The MWExperiment class converts all of these lines to the waveform files used by the AWGs using specifications from two yaml files, named configuration and calibration, which describe relevant details of the system such as the equipment connections and desired waveform synthesis methods, measured delays for any of the equipment, and calibrated initialization, control, and readout parameters for the system under study. The class also contains a structure, named params, which allows the user to configure parameters such as the preferred

initialization and readout methods (which are generated according to the configuration files described above) and how the waveforms should be synthesized (directly using the AWG7102 or using the IQ modulations of the SRS384), as well as how many times the experiment should be repeated and how often confocal tracking should be performed. This structure also records information used in plotting the results of the experiment, such as which variable is being swept and what the sweep values are, and is saved along with the AWG files to give a complete description of the experiment.

4.4. Example Experiment

To show a concrete example, here we show the script used to generate a simple Ramsey experiment, as described in Fig. 2.3(b). Due to the modularity of the platform, most of the details are handled automatically, and more complicated pulse sequences can be built quickly. The files output by this script can be directly loaded into the home-built Matlab control infrastructure used in our lab to run the experiment with no further changes.

```
#External imports
import numpy as np
from omegaconf import OmegaConf

#Internal imports
from qel_seq_gen.pulses import PulseSchedule,DelayPulse,IQPulse
from qel_seq_gen.experiments import MWExperiment
from qel_seq_gen.calibration import CalibratedPulses

# Loading configs (can also alter certain parameters here)
config_file = 'configurations\\room_temp_setup_config.yaml'
calib_file = 'calibrations\\SIL_VIII_061514EL01_RTS_Calibration.yaml'
config = OmegaConf.load(config_file)
calib = OmegaConf.load(calib_file)

# Setting up experiment parameters
params = OmegaConf.create()
params.experiment_directory = "Nuclear_Spins"
params.experiment_name = "Ramsey"
```

```
params.readout_calibration = True
params.readout_mode = "wait"

# Parameters
detuning = 5e-3 #GHz
taus = list(range(25,5000,25))
params.var = {}
params.var.name = "Tau (ns)"
params.var.values = list(taus)
params.mw1 = {}
params.mw1.freq = calib.m1.freq
params.mw1.attenuation = calib.m1.attenuation
params.mw1.gen = config.mw1.gen
params.mw_sample_period = 1 #ns
params.interleave_batch_size = 0
params.optical_sample_period = 1
params.repetitions = 300e3
params.tracking_time = 600

mw_lines = []
calib_lines = []
init_lines = []

cal_pulses = CalibratedPulses(calib)
xpi2 = cal_pulses.m1_pi2
xpi = cal_pulses.m1_pi

#Readout Calibration Lines
if params.readout_calibration:
    calib_lines.append(PulseSchedule([], 'Readout Calib 0'))
    calib_lines.append(PulseSchedule([xpi], 'Readout Calib 1'))

# Echo Lines
for tau in taus:
    mw_lines.append(PulseSchedule([xpi2, DelayPulse(tau),
    IQPulse(xpi2, np.pi + 2*np.pi*tau*detuning)], #Final pulse is detuned
    'Ramsey tau ('+str(tau)+') -X'))

# Making and saving the experiment
echo_experiment = MWExperiment(mw_lines, calib_lines, init_lines, config, calib, params)
echo_experiment.save()
```

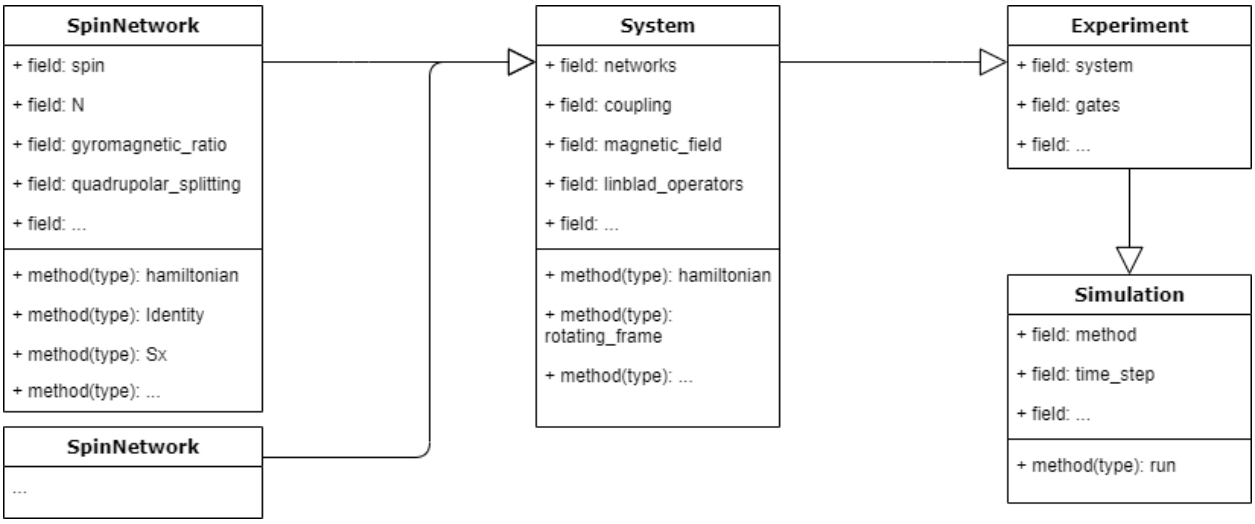

Figure 4.6: Class structure of the simulation package. Networks of identical spins with arbitrary coupling are grouped into a SpinNetwork. An arbitrary number of SpinNetworks form a System, with all-to-all coupling allowed. As well as providing convenience functions, methods allow these classes to construct the Hamiltonian for the system as a whole. An Experiment is defined as a series of gates on the System, at specific times, under the bang-bang approximation - where the gates are applied perfectly and in a time much shorter than the other dynamics of the system. Finally, the Experiment is simulated by a Simulation class, which allows different methods of numerical simulation, as well as adjusting their parameters.

While many quantum simulation packages are available, most are either general purpose or designed for narrow applications. To aide in our study of defect systems, we designed and built a flexible package which can describe and simulate coupled spin networks. This is built using the open-source QuTip package to handle the underlying operator definitions and master equation simulations.[139, 140]

4.5.1. Spin Networks

The fundamental unit of study we consider is a spin network, defined as a number of identical spins (electrons, nuclei, etc.) with the same spin number, gyromagnetic ratio, and quadrupolar parameters. The network can have arbitrary couplings between the spins. The

package gives convenience functions that provide the spin operators for individual nuclei, as well as the network as a whole (defined as the product of such operators on each individual spin), and identity functions (which are useful when creating operators for parent systems). There is also a function which returns the Hamiltonian for the whole network, without any external couplings, given the applied magnetic field.

4.5.2. Systems

Systems are defined by an arbitrary number of spin networks, coupled in an any-to-any manner, in a global magnetic field. Sparser couplings are defined by setting the appropriate coupling components to 0. Similar to the spin networks, systems define functions which give the Hamiltonian for the entire system, as well as other useful information, such as an interaction basis which can be used to simplify simulations.

One example would be an NV center system, with a single central electronic spin coupled to the single Nitrogen nuclear spin, a bath of Carbon-13 nuclear spins, and a bath of electronic P1 spins. Here, the package can handle both coupling between the networks as well as coupling within the networks to simulate the dynamics of the system as a whole. However, with the limitation of current simulation methods, we often look at just the relevant subsets of such a system to study the dynamics we want to understand.

4.5.3. Depolarization and Decoherence

The class structure can also describe open systems using Linblad operators, such as those associated with decoherence and depolarization. While this does limit the package to describing Markovian processes, future iteractions of the package could combine techniques to map the environment around out system, such as those described in the previous chapter, with techniques which simulate decoherence processes in an efficent manner - such as cluster expansion methods - to simulate higher order dynamics and more accurately capture the effects of the non-Markovian dynamics.

4.5.4. Charge and Optical Transitions

The simulation package only explicitly captures the spin degrees of freedom in our system and ignores the charge and optical degrees of freedom. This greatly speeds up the simulations, and captures most of the dynamics we are interested in. Furthermore, most experiments use readout calibrations which remove the lowest order contributions of these effects. However to capture higher-order effects, these can also be approximated with spin-dependent Linblad operators in the master equation simulations.

4.5.5. Experiments

Finally, the Experiment classes describe the experiments we are interested in. In an experiment, the system under study begins in a (pure or mixed) initial state, which is typically a product state in between the systems (although any arbitrary state can be used). The system is then evolved through periods of free evolution, with gates in between (defined by exact operators on the system state). This so-called "bang-bang" approximation, where gates are assumed to be perfectly described by the desired unitary and happen much faster than the free dynamics involved in the system, is a good approximation for the electronic pulses we typically use - which are much faster ($\gtrsim 10\,\mathrm{MHz}$) than the relevant couplings ($\lesssim 3\,\mathrm{MHz}$). Non-idealities, such as pulse errors and small amounts of evolution during the pulse, can be approximated by altering the gate operators.

4.5.6. Simulation Methods

Currently, the only supported simulation method in the package uses the master equation evolution from QuTip. While this is the most computationally expensive method, it is also the most accurate and is able to capture dynamics for the small systems we are currently studying.

4.6. Simulation Example

Here we show a simplified example of a script used to run the simulations. This will produce a plot of the acquired XY8 data (which has been saved into an high density storage format) and a comparable simulation using all the fitted parameters of our system, similar to Fig. 5.2. Since most of the details are hidden within the class structure, this can quickly and easily be adapted to new experiments.

```
from NVCenter import NVCenter
from qel_spin_sim.simulations import Experiment, ExactSimulation
import matplotlib.pyplot as plt
import numpy as np
import qutip
import h5py

data_file = "S:\\Projects\\Nuclear Spin Control\\hf5_data\\xy8_N_32_sweep.h5"

visibility = 0.85
offset = 0.05

electron_init_state = '0' #init state for electron spin
electron_T1 = 0 #Relaxation time for central spin
nitrogen_init_state = 'mixed' #initial state of the nitrogen spin
carbon_init_state = 'mixed' #initial state of the carbon spin
magnetic_field = 263.2 #267 #Gauss
inc_nitrogen = True
inc_non_sec = False #Whether to include non-secular terms
#Parallel and perpendicular hyperfine coupling for each C13
carbon_hyperfine_coupling = 2*np.pi*np.array([[-86.1e3,58.3e3],
                [-118.8e3, 68.4e3],
                [-46.4e3,67.7e3],
                [10.1e3, 25.4e3]])
carbon_interactions = None #interactions within the c13 bath

pulse_n = 32
min_tau = 0e-6
max_tau = 5e-6
tau_step = 10e-9
tau_sweep = np.arange(min_tau, max_tau, step=tau_step) #s
```

```
32
33  sim_time_step = 0 #leave 0 for no steps
34
35  def dd_gate_sim(tau, system, init_gate, dd_gate, pulse_n, readout_gate, coherence_op):
36          #Building the gate sequence
37          gates = [(0, init_gate)] #initialization pulse
38          #DD Gates
39          gates.extend([(tau + 2*tau*i_pulse, dd_gate) for i_pulse in range(pulse_n)])
40          gates.append(((2*pulse_n)*tau, readout_gate)) #readout pulse
41          exp = Experiment(gates)
42          sim = ExactSimulation(system, exp)
43          results = sim.run(time_step=sim_time_step)
44          #getting coherence
45          final_state = results[-1][-1]
46          return qutip.expect(coherence_op,final_state)
47
48  #Needed for the multiprocessing
49  if __name__ == '__main__':
50          data = h5py.File(data_file, 'r')
51          taus_ns = np.array([tau[0] for tau in data['tau']])
52          p0 = np.array([signal[0] for signal in data['signal']])
53          err = np.array([signal[0] for signal in data['error']])
54          plt.errorbar(taus_ns / 1e3, p0, err,  label = 'Data', linestyle = 'dashed', fmt='.')
55
56          NV = NVCenter(electron_init_state = electron_init_state,
57                                  electron_T1 = electron_T1,
58                                  nitrogen_init_state = nitrogen_init_state,
59                                  carbon_hyperfine_coupling = carbon_hyperfine_coupling,
60                                  carbon_interactions = carbon_interactions,
61                                  carbon_init_state = carbon_init_state,
62                                  magnetic_field = magnetic_field,
63                                  inc_nitrogen = inc_nitrogen,
64                                  inc_non_sec = inc_non_sec)
65          init_gate = NV.m1_X_gate(np.pi/2)
66          dd_gate = NV.m1_X_gate(np.pi)
67          read_gate = NV.m1_X_gate(-np.pi/2)
68          signal = np.array(qutip.parallel.parallel_map(dd_gate_sim, tau_sweep,
69          task_args=(NV, init_gate, dd_gate, pulse_n, read_gate, NV.meas_0), progress_bar=True))
70          plt.plot(tau_sweep*1e6, visibility*np.transpose(signal) + offset, label='Simulation')
71
72          plt.xlim([min_tau*1e6,max_tau*1e6])
73          plt.ylabel('P(|0>)')
```

```
74          plt.xlabel('Tau (us)')
75          plt.legend()
76          plt.show()
```

CHAPTER 5

NUCLEAR SPIN REGISTERS

While we have so far focused on the electronic spins associated with defects in semiconductors, perhaps no less important are the nuclear spins coupled to them. Some materials, such as diamond and Silicon-Carbide (SiC), can be isotopically purified by growing crystals using spin-0 nuclear isotopes, but others, such as hBN, cannot due to the lack of stable spinless isotopes. While originally viewed as a nuisance due to their effects limiting the coherence time of electronic spins, these nuclear spins became of great interest due to their extraordinarily long lifetimes even at room temperature. This allows them to be used to improve the readout of electronic spins[141], increase sensitivity of sensing schemes[142, 143], as well as to act as long-lived registers of quantum information[144, 145, 146]. In addition, characterizing the properties of the nuclear spins themselves is of great interest. Mapping nuclear spin networks reveals the atomic structure of the material studied, and the sensitivity of nuclear spins to local properties of the host material such as electric field gradients can be used to reveal information about bonding patterns and identify materials.

In this chapter we review some relevant techniques used to characterize and control nuclear spins coupled to optically active electronic spins.

5.1. Detection and Coherent Control

While early experiments focused on defects in materials carefully grown without nuclear and electronic spins to extend the lifetime of defect qubits[147], it was discovered that strongly coupled spins exhibited coherent interactions with the defect spin[148, 149] and could therefore be used for quantum information applications. While it is possible to control nuclear spins directly with lower frequency RF tones and strongly coupled spins can be characterized and entangled with the defect spin using ESR-type pulses, one particularly elegant solution for characterizing, entangling, and controlling a large number of nuclear spins is provided by dynamical decoupling sequences.

Dynamical decoupling, as the name implies, was designed to leverage the fast control of electronic spins to decouple them from the slower precession of nearby nuclear spins. Since the nuclear spin states have a finite correlation time due to interactions with the larger nuclear spin bath, this precession induces a quasi-randomly varying magnetic field that leads to decoherence in the electronic spin on long time scales. [150, 151, 152] By applying regularly spaced pulses to the electron spin, these slow variations cancel out, with the coherence time of the electron growing as the spacing between the pulses is decreased (or, equivalently, the number of pulses in a fixed amount of time is increased).[153] However, by bringing the DD pulse spacing into resonance with the precession of one or more nuclear spins, the hyperfine interaction between the electronic and nuclear spins can be resonantly enhanced. The unique hyperfine coupling of each nucleus with the central electronic spin, which shifts the nuclear precession frequencies when the electron is in the $m_s = \pm 1$ states, allows individual nuclei to be entangled and controlled. This is particularly useful for nuclear spins with hyperfine coupling weaker than the inverse of the Ramsey decoherence time, $|A| < \frac{1}{T_2^*}$, for which other techniques fail. The technique was first demonstrated by Taminiau et al.[154] with Carbon-13 nuclei coupled to NV centers in diamond. Here we review this important example.

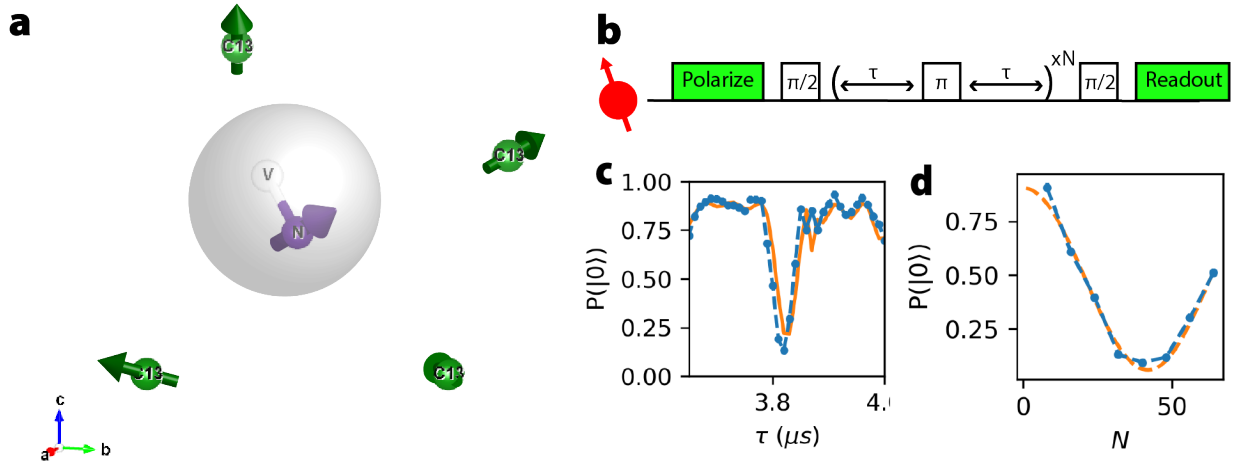

Figure 5.1: (a) The nuclear spin environment of a typical NV center in diamond. The central electronic spin (gray) interacts strongly with the Nitrogen nuclear spin (purple). Less strongly coupled are the Carbon-13 nuclei surrounding the NV center. (b) Example of a dynamical decoupling sequence used to detect nuclear spins using the electronic spin. Initial and final $\frac{\pi}{2}$ pulses are used to map the polarization of the NV center onto and back from the angle along the equator. N regularly spaced π pulses are applied, with spacing 2τ and symmetrized using an XY8 pattern. (c) Results of sweeping the τ parameter of the above sequence applied to an NV center in bulk type IIa diamond. N is fixed to 32 pulses. Blue markers with dashed line represent experimental data (errorbars are comparable to the size of the marker) and solid orange lines represent the result of simulations using the best fit parameters from the procedure described in Section 5.3. Several isolated dips show entanglement with different Carbon-13 nuclei. (d) Results of sweeping the N parameter for fixed $\tau = 3.82\,\mu$s. The oscillation shows the electron coherently entangling and disentangling with a single Carbon-13 nucleus.

As shown in Fig. 5.1(a), a typical NV center in type IIa diamond has a simple nuclear spin environment. The central electronic spin (gray) interacts strongly with any spins close to the NV center, such as the Nitrogen nucleus (purple, 99.7 % ^{14}N) and Carbon-13 nuclei (green, $\approx 1\,\%$ of the lattice in natural isotopic abundance), through a combination of contact interactions and dipolar coupling. For spin-1/2 isotopes, such as ^{13}C, the Hamiltonian of a nuclear spin coupled to an electronic spin in an field along the electronic spin axis can be

written as

$$H_N = A_\parallel S_Z I_Z + A_\perp S_Z I_X + \gamma_N B_Z I_Z \tag{5.1}$$

where $A_\parallel$ and $A_\perp$ are the parallel and perpendicular components of the hyperfine coupling, $I = (I_X, I_Y, I_Z)$ is the nuclear spin operator, γ_N is the nuclear gyromagnetic ratio, and B_Z is the (on-axis) magnetic field. Here we assume that the off-axis components of the magnetic field are negligible. Note that, without loss of generality, the axes are chosen such that the perpendicular component of the hyperfine coupling lies along the X axis of the nuclear spin. Hyperfine coupling terms involving S_X and S_Y can be ignored due to the large mismatch in energy scales between the electronic spin splitting and nuclear spin splittings. $A_\parallel$ shifts the nuclear precession frequency, while $A_\perp$ creates off-axis rotations of the nuclear spin. Normally, the off-axis rotations would cancel out due to the precession of the nuclear spin, but if the electron spin is flipped resonantly with this precession they will instead add constructively.

Fig. 5.1(b) shows the DD sequence used to create and measure this effect. First the electron is initialized and placed into an equatorial superposition state using a $\frac{\pi}{2}$ pulse. Electron π pulses are applied, spaced by 2τ and symmetrized in an XY8 pattern (X-Y-X-Y-Y-X-Y-X), to create the resonant effect. Finally, the electron angle along the equator is mapped back onto an on-axis polarization using a final $\frac{\pi}{2}$ pulse of opposite phase. The XY8 pattern reduced the effect of axis-dependent pulse errors. [155] To identify nuclear spin resonances, the τ parameter is swept across a wide range. Assuming the hyperfine coupling is much less than the Larmor frequency, $A_\parallel, A_\perp << \omega_L \equiv \gamma_N B_Z$, dips will appear when the spacing is resonant with a nuclear spin such that

$$\tau_k = \frac{(2k-1)\pi}{2\gamma_N B_Z + A_\parallel} \tag{5.2}$$

for some natural number k. An example of a small section of such a spectroscopy dataset is shown in Fig. 5.1(c), where τ is swept at a fixed $N = 32$. Here, a single well-isolated dip is visible, corresponding to $k = 3$ and $A_{\parallel} \approx 2\pi \times -86.1\,\text{kHz}$. Fig. 5.1(d) shows the effects of sweeping N at fixed $\tau = 3.82\,\mu\text{s}$. The oscillation shows the NV electron entangling and disentangling with the Carbon-13 nuclear spin, with a result of $P(|0\rangle) = 0.5$ showing the point of maximum entanglement.

The following section shows an example of how we used these resonances to identify and fit the hyperfine parameters of the four strongest Carbon-13 nuclei coupled to an isolated NV, a process vastly simplified by the flexible experiment and simulation framework described in Chapter 4.

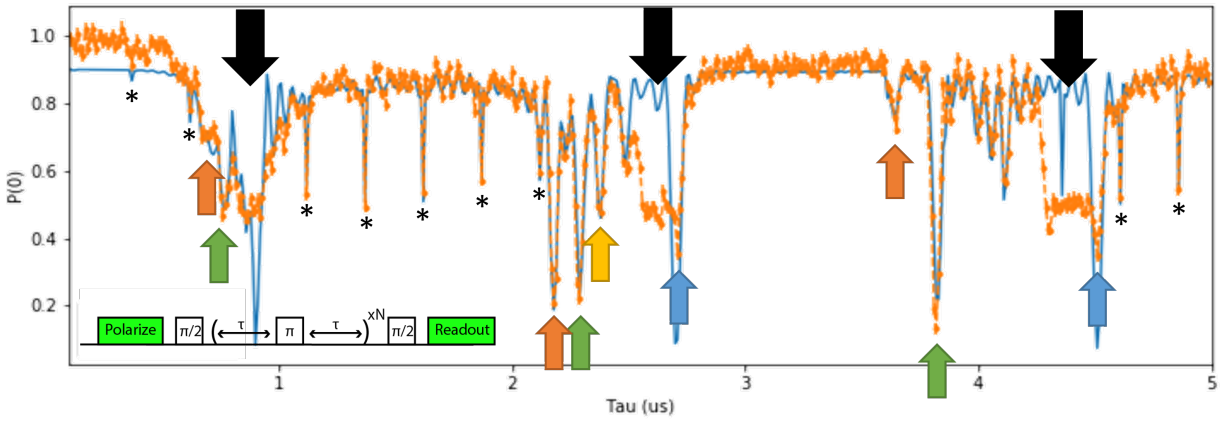

Figure 5.2: Here we present a wide sweep of τ for an XY8 DD experiment with a fixed $N = 32$ pulses (pulse sequence shown in inset). Periodic resonances appear at odd numbers (1,3,5,...) of multiple fundamental resonance frequencies, as predicted in Eq. (5.2), indicating entanglement of the electron spin with the nuclear spin environment. Large, broad resonances that saturate to $P(|0\rangle) \approx 0.5$ (marked by black arrows) indicate resonance with the Carbon-13 spin bath, where the NV entangles with a large number of nuclei all precessing at the Larmor frequency. Sharp resonance with short separation, marked with asterisks, are caused by resonance with the Nitrogen-14 nuclear spin, and associated with the effect described in Chapter 6. Additional isolated resonances, marked by colored arrows, are caused by Carbon-13 nuclei with moderate hyperfine coupling to the NV center electronic spin. Since their resonance frequencies are shifted by their unique hyperfine coupling, they separate from the larger nuclear spin bath resonance and other isolated resonances for large values of the resonance order k. Blue line indicates simulation using the best-fit parameters from our simulations (including the Nitrogen quadrupolar terms discussed in Chapter 6) and orange markers with dashed line indicates the experimental results. They are in good agreement except near the Larmor frequency, as the dynamics of the nuclear spin bath are not captured in our exact simulation.

We begin by noting that, from our Ramsey and ESR data, the NV we are here studying does not seem to have any strong nuclear spin couplings ($\gtrapprox \frac{2\pi}{T_2^*} \approx 2\pi \times 200\,\text{kHz}$), other than the known $2\pi \times 2.16\,\text{MHz}$ coupling to the Nitrogen-14 nuclear spin within the NV center itself. Based on this, we set the longitudinal magnetic field to be $\gtrapprox 200\,\text{Guass}$, such that the Larmor frequency of any Carbon-13 nuclei, $\omega_L = \gamma_{^{13}C} B_Z$, is greater than their hyperfine

coupling to the NV center electronic spin. The field is calibrated in both strength and angle by taking ESR data of both the $m_s = 0$ to $m_s = \pm 1$ transition, and using the formula given in [156]. The field is generally aligned by hand to be within $\approx 2-3^\circ$ of the NV axis, yielding good agreement with our models (which assume the magnetic field to lie perfectly along the axis).

After aligning the field and calibrating the microwave pulses for the $m_s = 0$ to $m_s = -1$ electron spin transition, we apply an XY8 dynamical decoupling sequence with a fixed $N = 32$ pulses, while sweeping the pulse separation parameter τ. Doing this, we find multiple resonance series showing the electron spin coupling to different parts of the nuclear spin environment. Broad resonances (marked by large black arrows) that saturate to $P(|0\rangle) = 0.5$ (indicating complete entanglement of the electron spin) are found with spacing corresponding to the inverse of the Carbon-13 Larmor frequency, indicating that the NV is entangling with the Carbon-13 spin bath. Sharper resonances (indicated by asterisks) with closer spacing are associated with the Nitrogen-14 nuclear spin, and arise due to the terms in the nuclear quadrupolar Hamiltonian discussed in Chapter 6. Isolated dips of moderate size, indicated by colored arrows, are associated with individual Carbon-13 nuclei which are coupled to the NV center. These begin close to the Larmor frequency resonance at low resonance number, but due to the unique hyperfine coupling of each nuclei they had a different fundamental resonance frequency and separate from the bath resonance at larger resonance numbers, as indicated by the formula in Eq. (5.2). We find four such series in this data, and we zoom in on well isolated resonances to gain more information about each nuclear spin.

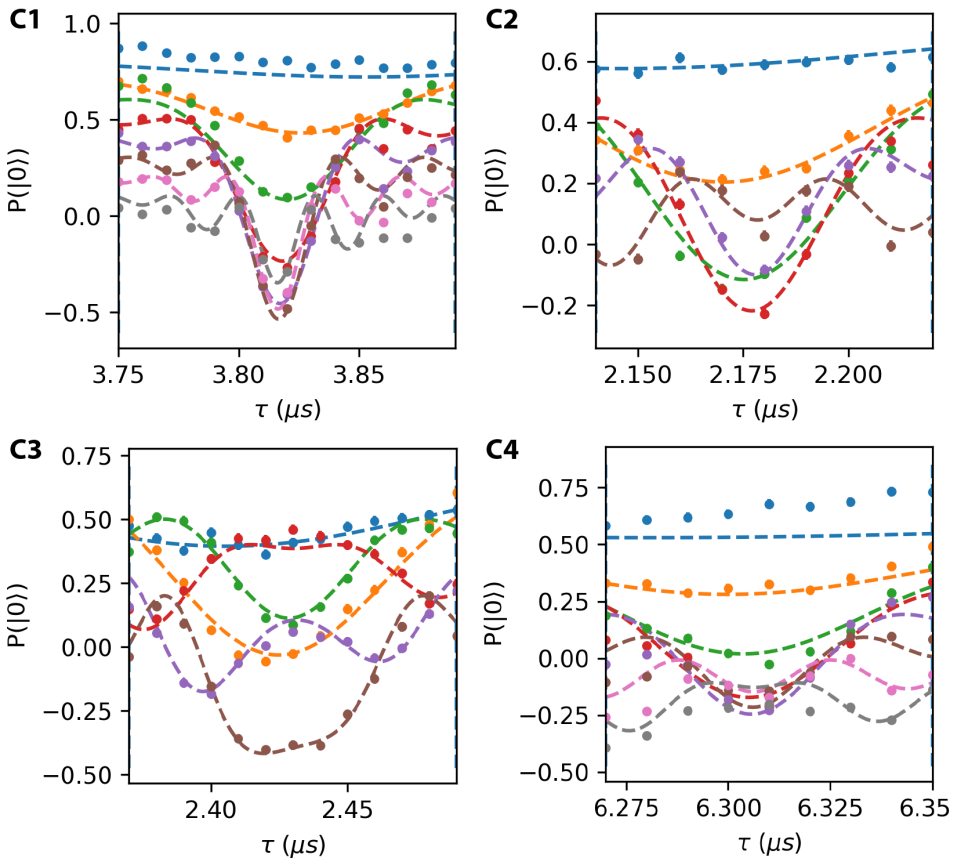

Figure 5.3: Dynamical decoupling data taken while sweeping both N and τ around isolated Carbon-13 resonances. Data is waterfalled, decreasing by 0.1 every 8 pulses, to aid the reader in seeing the effects of increasing N. While all resonances show oscillations, the resonance location in τ is not perfectly constant as N is increased, indicating that the simulation is more accurate in regimes where the approximation assumptions fail.

Since the resonance separate at higher resonance numbers, we can take use data taken from individual resonances to fit the parameter of each nucleus one at a time. In Fig. 5.3 we show the result of sweeping both N and τ of the XY8 sequence around isolated resonances for each of the Carbon-13 nuclear resonance series identified in Fig. 5.2. Carbon C1 has the cleanest oscillation, that lines up the closes with the analytical expressions. While carbons C2 and C3 still show clear oscillations, they show a small dependence of the resonance location in τ as

N is changed. They also show an asymmetry around the resonance maximum, both of which are in disagreement with the analytical approximations shown in Eq. (5.2) and [154]. This occurs since they have relatively large perpendicular hyperfine couplings $A_\perp$ compared to their fundamental resonance frequencies, violating the approximation assumptions. Finally, the carbon C4 resonance is close to the bath Larmor frequency. While we went to a higher resonance ($k = 4$), the data still shows decreased visibility due to this overlap. While this means that an even higher order resonance would be required to entangle this carbon with the NV with high fidelity, it can still be used to fit the nuclear hyperfine parameters.

All of these datasets are fit using the simulation package described in Chapter 4 and the scipy curve_fit method. Free parameters allowed to vary were the two hyperfine parameters, $A_\parallel$ and $A_\perp$, as well as overall visibility and offset parameters which allowed the fits to take into acconut the overlap with other extended features and any reduced readout visiblity due to pulse imperfections. The results of the best-fit simulations are shown as dashed lines in Fig. 5.3, as well as in the larger spectra in Fig. 5.2, and agree well with the data except near the Carbon-13 nuclear spin bath resonance (which is expected becuase the bath is not included in our exact simulations). A table of best-fit parameters is given in Table 5.1. Note that while our values for $A_\perp$ will always be positive since we have chosen our X axis to align with the hyperfine coupling, the sign of $A_\parallel$ is non-trivial, as it shifts the resonance frequencies up or down depending on its sign.

Carbon	$A_\parallel(2\pi \times kHz)$	$A_\perp(2\pi \times kHz)$
C1	−86.1(1)	58.3(8)
C2	−118.8(1)	68.5(7)
C3	−46.4(1)	67.7(3)
C3	10.1(1)	25.4(7)

Table 5.1: Fit values for Carbon 13 hyperfine parameters

While we have here shown a simple example used to sense and characterize the nuclear spins,

these sequences can also be used to initialize, readout, and control the nuclear spins [157]. This allows mapping of the nuclear spin networks which we will now describe.

5.4. Mapping Nuclear Spin Networks

One consequence of being able to initialize and control the nuclear spins surrounding an electronic spin is that they themselves can be used as sensors of their own environment. While the nuclear-nuclear couplings are smaller than the nuclear-electronic couplings, the nuclear lifetimes are much longer than the electron spin lifetime - which means they can be used to detect couplings more accurately. One application of this is the mapping of nuclear spin networks by measuring the nuclear-nuclear couplings within the network using double resonance techniques such as Spin-Echo Double Resonance (SEDOR). While the nuclear-electron interactions are the result of a mix of contact and dipolar interactions, due to the extended wavefunction of the electronic orbitals, the nuclear-nuclear interactions are dominated by dipolar couplings. This makes it relatively simple to infer the physical separation of nuclear spins once their coupling has been measured. While multiple locations are possible for a given coupling, by measuring couplings between many pairs of spins within the network the problem quickly becomes over-constrained and the physical layout of the network can be obtained with good confidence.

The first example of this was by Abobeih et al.[158]. I was fortunate to be able to work on expanding the technique while on an NSF/IIE Graduate International Research Experience (GIRE) fellowship with the group of Tim Taminiau at TU Delft, and a publication based on the work is forthcoming. My specific contributions used multi-axis readout of the nuclear spins, which allowed signed couplings to be obtained, and computational improvements which greatly improved the memory requirements and runtime of the algorithm used to obtain the nuclear spin locations from the coupling map. Using this, I was able to identify several new nuclei within the network.

CHAPTER 6

QUADRUPOLAR RESONANCE SPECTROSCOPY OF SINGLE NUCLEAR SPINS

The following chapter is a draft of a manuscript being prepared for submission by S. Alex Breitweiser, Tzu-Yung Huang, Mathieu Ouellet, and Lee C. Bassett.

6.1. Abstract

Nuclear Quadrupolar Resonance (NQR) spectroscopy can be used to probe chemical bonding patterns in materials and molecules through the unique coupling between nuclear spins and local fields. However, traditional NQR techniques require large ensembles of nuclei as the signal from each individual nucleus is too small to be detected - making it difficult to perform spectroscopy on an individual molecule or atomic site. Optically active electronic spin defects, such as the Nitrogen-Vacancy (NV) center in diamond, have been used to amplify the signal from coupled nuclei, enabling NQR spectroscopy of nuclear ensembles within an individual molecule. Here we use NV centers to precisely map the quadrupolar Hamiltonian for multiple individual Nitrogen-14 nuclei. Due to the sensitivity of this technique, we are able to measure differences between the quadrupolar parameters of different nuclei at a level beyond any previously reported method. In addition, this method reveals a previously unreported term that directly couples the $|m_I = -1\rangle$ and $|m_I = +1\rangle$ nuclear spin levels. We further demonstrate an association between the nuclear quadrupolar Hamiltonian and the electronic zero-field splitting parameters, which are related to strain and electric fields present at the defect site. This demonstrates the potential for high-sensitivity tomography of individual nuclear spin Hamiltonians using solid-state defects, highlighting the potential of single-spin NQR for molecular analysis.

6.2. Background

Nuclear Quadrupolar Resonance (NQR) has been used to great effect in the detection of explosive compounds [159] as well as in pharmaceutical analysis [160]. Due to the unique fields experienced by nuclei at each site, set primarily by the valence electrons and, therefore, the corresponding chemical bonds, NQR signals can reveal a wealth of information which

can be used to identify and characterize molecules and bulk materials. However, due to the small amount of signal obtained from each nucleus, traditional radio-frequency NQR is typically used only on bulk materials or collections of molecules with a large number of identical nuclei. This precludes the study of individual molecules and nuclear sites, obscuring any information about differences present due to local variations.

In recent years, experiments on optically active defects in semiconductors have allowed for investigations into smaller numbers of nuclei. These defects can host electronic spin states which can be initialized and measured with laser light and manipulated with microwave signals at room temperature. Dynamical Decoupling (DD) sequences have been shown to resonantly amplify the coupling of these electronic spins with surrounding nuclei [154], allowing high precision characterization and control of individual nuclei[157]. DD experiments on Nitrogen-Vacancy (NV) centers in diamond have already been shown to detect NQR signals from nuclear spin baths, distinguishing between monolayer and multi-layer regions within flakes of hexagonal Boron Nitride (hBN) [161, 162]. They have also been demonstrated to capture NMR signals from small nuclear ensembles within individual molecules. [163]

Here we demonstrate DD-based NQR spectroscopy of multiple individual Nitrogen-14 nuclei coupled to NV centers, accurately measuring the nuclear quadrupolar and hyperfine parameters and showing that they vary in a statistically significant way. We find at least one Nitrogen-14 that shows dynamics consistent with a previously unreported term in the nuclear quadrupolar Hamiltonian, and finally show that the nuclear hamiltonian parameters correlate with the electronic Zero-Field Splitting (ZFS) parameters - which are themselves a measure of the local fields present at the defect site. Finally, we run simulations to show the sensitivity of this technique in different regimes, including under the effects of decoherence.

6.3. The Nitrogen-14 Nuclear Hamiltonian

A prototypical example of an optically active spin defect, the Nitrogen-Vacancy (NV) center in diamond (Fig. 6.1a), consists of a substitutional Nitrogen coupled to a vacancy in the diamond lattice. In its negatively charged state, the NV center hosts an electronic spin-1 state which undergoes a spin dependent optical transition, allowing the spin state to both be initialized and read out with laser light. The electronic spin interacts with the intrinsic Nitrogen nuclear spin within the NV center ($\approx 99.7\,\%$ Nitrogen-14 in natural abundance), as well as Carbon-13 nuclei in the surrounding diamond lattice ($\approx 1.1\,\%$ natural abundance) and any other nearby nuclear spins.

The Hamiltonian of the Nitrogen-14 nuclei within the NV center is governed by the hyperfine coupling to the electronic spin, as well as the Zeeman splitting and the quadrupolar splitting, both of which are caused by coupling to external fields.

$$H_{^{14}N} = H_{\mathrm{hf}} + H_{\mathrm{Z}} + H_{\mathrm{quad}} \tag{6.1}$$

The hyperfine interaction for the Nitrogen-14 nuclei is constrained by symmetry to a small number of terms

$$H_{\mathrm{hf}} = A_Z S_Z I_Z + A_\perp (S_X I_X + S_Y I_Y) \tag{6.2}$$

where A_Z and $A_\perp$ are the parallel and perpendicular hyperfine coupling strengths, $S = (S_X, S_Y, S_Z)$ is the electronic spin operator, and $I = (I_X, I_Y, I_Z)$ is the nuclear spin operator. The Zeeman interaction is determined by the external magnetic field, $B = (B_X, B_Y, B_Z)$, and the Nitrogen-14 gyromagnetic ratio, $\gamma_{^{14}N}$.

$$H_{\mathrm{Z}} = \gamma_{^{14}N} B \cdot I \tag{6.3}$$

Nuclear Magnetic Resonance (NMR) literature shows that quadrupolar terms can arise from an off-axis electric field gradient. [165] The notation used in the NMR literature is such that

$$H_{\text{quad}} \triangleq \frac{eQV_{zz}}{4I(2I-1)}[3I_Z^2 - I(I+1) + \frac{\eta}{2}(I_+^2 + I_-^2)] \tag{6.4}$$

where e is the electron charge unit, Q is the quadrupolar moment unique to each nuclear isotope, V_{zz} is the electric field gradient along the principal nuclear axis, which here should be close to the NV axis, and $\eta \triangleq \frac{V_{xx}-V_{yy}}{V_{zz}}$ is a dimensionless parameter giving the relative strength of the off-axis electric field gradient. Note that the principal axes are chosen so that $|V_{zz}| > |V_{xx}| > |V_{yy}|$ and the electric field gradient is diagonal in this basis.

However, due to the symmetry of the NV center, *eta* is expected to be 0, and the quadrupolar Hamiltonian is typically written in NV literature as

$$H_{\text{quad}} = P(I_Z^2) \tag{6.5}$$

Where constant terms have been omitted, leaving a single quadrupolar splitting parameter P.

Spin-echo techniques have previously measured P[166], but DD techniques offer the ability to increase the spectral resolution of these measurements - measuring known terms to higher precision and also revealing previously unreported terms of smaller magnitude.

6.4. Measuring the Hamiltonian parameters of single nuclei

In the presence of a purely longitudinal magnetic field ($B = B_Z\hat{z}$), the perpendicular component of the hyperfine coupling ($A_\perp$) can be ignored due to the large mismatch in energy splitting between the electronic and nuclear spin states. However, in the presence of a weak transverse magnetic field ($B = B_Z\hat{z} + B_X\hat{x}$, $B_X \ll B_Z$) an effective perpendicular coupling

term appears due to spin mixing, leading to approximate hyperfine coupling of

$$H_{hf} \approx A_Z I_Z S_Z + \frac{\gamma_{^{14}N} B_X A_\perp}{\gamma_e B_Z} F S_Z I_X \tag{6.6}$$

where γ_e is the gyromagnetic ratio, and F is a constant that is particular to the Nitrogen-14 nuclear isotope. [167]

The new $S_Z I_X$ term in the effective hyperfine hamiltonian leads to off-axis rotations of the Nitrogen-14 nuclear spin which change directions depending on the state of the electron spin. Dynamical decoupling experiments (Fig. 6.1b) amplify this interaction when the spacing between pulses is resonant with the shifted frequency of the nuclear Larmor precession, causing two additional resonance series to emerge - one corresponding to each of the $|m_I\rangle = 0$ to $|m_I = \pm 1\rangle$ transitions. Fig. 6.1c,d show data (markers) obtained while sweeping the pulse spacing near these resonances for two NVs in bulk diamond for a fixed $N = 32$ pulse number. Interpolated pulse spacings are used to further increase the resolution beyond the hardware limitations. [164]

The shift of the resonance between the two NVs is consistent with a significant difference in both the hyperfine coupling A_Z and the quadrupolar splitting P. By taking multiple spectra with varying pulse numbers around these resonances, the values for A_Z and P can be fit to high accuracy using a simulation of the NV system. The results of best fit simulation are shown in Fig. 6.1c,d with dashed lines. Table 6.1 shows the results of such fits from these and several other NV centers in bulk diamond (Full data and additional information available in the online supplementary info). Interestingly, the values obtained for both P and A_Z vary an amount several orders of magnitude larger than the uncertainty in the fits. One NV in particular, NV A (Fig. 6.1c,d, blue), shows a value for P and A which differs by several kHz from any of the other NVs measured.

6.5. New term in the Quadrupolar Hamiltonian

In the presence of a purely longitudinal magnetic field ($B = B_Z\hat{z}$), the Larmor frequency of the Nitrogen-14 nuclear spin does not depend on the state of the electron spin. This means that no Nitrogen-related resonances are expected in the dynamical decoupling spectrum. However, dynamical decoupling spectroscopy (Fig. 6.2a, blue markers) of NV A under a purely longitudinal field show sharp, periodic resonances that indicate coupling to a spin precessing at a rate of approximately 4 MHz. Electron spin resonance (ESR) data on the same NV (Supplementary Info) show no couplings of this strength other than the hyperfine coupling to the spin-1 Nitrogen-14 nuclear spin.

Simulations (Fig. 6.2a, solid orange line) show this resonance series is consistent with a previously unreported term in the nitrogen quadrupolar hamiltonian, corresponding to an expanded quadrupolar splitting

$$H_{\text{quad}} = P(I_Z^2) + \alpha(I_+^2 + I_-^2)) \tag{6.7}$$

where P is the previously reported quadrupolar splitting and α is a term which directly couples the $|m_I = -1\rangle$ and $|m_I = +1\rangle$ states of the Nitrogen-14 nucleus, possibly arising from a non-zero electric field gradient η in (6.4).

Further consistent with this model is the contrast of the oscillation when sweeping the number of pulses at a fixed resonant pulse spacing (Fig. 6.2b), which is reduced by approximately $\frac{1}{3}$ due to the occupation probability of the $|m_I = 0\rangle$ state.

Normally, α is expected to be zero due to the symmetry of the NV center, but in the NV A system α is fitted to be 2.429(12) kHz (Fig. 6.2c,d).

This model is consistent with data taken at multiple magnetic fields and when using both

the $|m_S = 0\rangle$ / $|m_S = -1\rangle$ and $|m_S = 0\rangle$ / $|m_S = +1\rangle$ electron spin manifolds (Supplementary Info), confirming that this is consistent with the known values of the nuclear gyromagnetic ratio of Nitrogen-14 and the electro-nuclear hyperfine coupling.

6.6. Partial Initialization and Free evolution of the nuclear spin

A combination of conditional and non-conditional gates on the nuclear spin, based on the DD sequences described above, can be used to initialize the nuclear spin state using the electronic spin.[157]

To further demonstrate the correspondence to a direct $|m_I = \pm 1\rangle$ transition, a nuclear initialization sequence tuned to the new resonance series is applied to the NV, followed by a short ($\approx 100\,\text{ns}$) green laser pulse to reinitialize the electronic spin while leaving the nuclear spin state intact. (Fig. 6.3(a)).

Ramsey data taken with and without this initialization sequence (Power spectra shown inFig. 6.3b, blue and orange respectively - raw data available in the supplement) shows three oscillation frequencies corresponding to the three spin states of the Nitrogen-14 nuclear spin, separated by the hyperfine coupling of $A_Z \approx 2.17\,\text{MHz}$ in the optical ground state, with the relative amplitude of each oscillation showing the occupation probablity of the corresponding nuclear spin state.

Due to the large, off-axis hyperfine interaction in the optical excited state, the Nitrogen nuclear spin acquires a non-trivial polarization during repeated green illumination used to initialize and readout the electronic spin, leading to fitted steady-state occupation probabilities of 0.405(7) in the $|m_I = +1\rangle$ state and 0.251(7) in the $|m_I = -1\rangle$ state, with the remaining population in the $|m_I = 0\rangle$ state.

Fitting the Ramsey oscillations after initialization, however, shows that a significant amount

of the $|m_I = -1\rangle$ population has been transferred into the $|m_I = +1\rangle$ state, leading to occupation probabilities of 0.150(10) and 0.505(10), respectively.

By sweeping the amount of green illumination time used to reset the electron spin, we see that the nonequilibrium nuclear population lasts for several microseconds under green illumination (Fig. 6.2(d)) before returning to the steady state values, consistent with other studies on the nitrogen nuclear spin population [168].

This also confirms that the 20 us green laser pulse used to reset the NV system is sufficient to return the Nitrogen spin to its steady state value.

6.7. Sensitivity Analysis

The effect was not observed for any other NVs in the sample. To explain this, we examine the limits of this technique. The sensitivity of this technique is limited by both intrinsic decoherence mechanisms (captured by T_2) as well as pulse errors. The value of T_2 for NV A has been measured with a spin echo sequence to be $\approx 800\,\mu$s, and other NVs in the sample are expected to be similar. Since the total experimental sequence times are much shorter than this, the decay seen in the data is most likely due to pulse imperfections. We fit our experimental data using the decay envelope

$$S_N(t\tau) = e^{-\beta N} S_N^{sim}(\tau) \tag{6.8}$$

Where $S_N(\tau)$ is the expected signal for a DD experiment with N pulses with spacing τ, $S_N^{sim}(\tau)$ is the result of simulating the experiment with no decoherence or pulse imperfections, and β is a dimensionless parameter which characterizes the decay with the number of pulses. The effective β obtained from each DD fit is given in Table 6.1. NV A had the smallest β of $1.6(2)\,\text{x}10^{-3}$, with several other NVs having $\beta > 1\,\text{x}10^{-2}$.

Fig. 6.4(a) shows the maximum signal obtained in simulation as α is swept for various values of β. For $\beta = 1\,\text{x}10^{-2}$ the signal (green) only exceeds the noise floor (red dashed line, ≈ 0.03) for values of α greater than $\approx 200\,\text{Hz}$. Fig. 6.4(b) further confirms this by showing the average fit uncertainties from ten simulations at each value of α for various values of β, after including representative noise. α is considered undetectable when it is less than twice the uncertainty, meaning it is indistinguishable from 0 after being measured. Below this point, denoted by a dashed red line, the fit uncertainties also become large, further indicating the measured values are not reliable. The smallest measurable value of α is found when the uncertainty drops below α itself, which occurs around 100 Hz for $\beta = 1\,\text{x}10^{-2}$ (green).

6.8. Comparisons of NQR and ZFS parameters

Using the above fitted value of α for NV A gives a normalized electric field gradient value of $\eta = \frac{6*\alpha}{P} = 2.89 \times 10^{-3}$, using the notation from (6.4) above. Such an off-axis electric field gradient could arise due to a distortion of the NV's electron wave function due to strain or external electric field. Zero Field Splitting (ZFS) parameters extracted from ESR data on NV A differ significantly from the values obtained for other NVs in the sample (Table 6.1, raw data available in the supplementary info), consistent with a significant strain or electric field distortion.

Fig. 6.4(c) and (d) show the fitted values for the Nitrogen-14 quadrupolar splitting P and hyperfine coupling A plotted against the electronic D and E quadrupolar parameters obtained from zero field ESR data for each NV center studied here. There appears to be a non-trivial correlation between these values, further indicating that the nuclear quadrupolar Hamiltonian is likely influenced by local strain and electric fields.

6.9. Conclusion and outlook

Since the hyperfine and quadrupolar parameters are much stronger than the Zeeman splitting under these conditions, the resonances are stable under a wide range of magnetic field values. This means the magnetic field can be chosen to be convenient according to the system under study and experimental limitations. In the case of NV systems such as the one under study, the magnetic field can simply be made large enough to isolate the Carbon-13 resonances (c.f. Supplementary Info). This also means that the accuracy of the fits are not limited by the accuracy to which the magnetic field is known - $\Delta B \approx 0.1\,\mathrm{G}$ under these conditions, leading to a shift of $\gamma_{^{14}N}\Delta B \approx 2\pi\mathrm{x}30.7\,\mathrm{Hz}$.

Similar to other pulsed spectroscopy techniques, such as Nuclear Magnetic Resonance (NMR), the sensitivity of this technique is limited by T_2^e, the decoherence time of the electron. For nanodiamond and near-surface Nvs, which are of interest for sensing external nuclear spin baths, the effective decoherence time under dynamical decoupling has been shown to scale as

$$T_2^{e,DD} \approx N^{\gamma} T_2^e \tag{6.9}$$

where $T_2^{e,DD}$ is the decoherence time under a dynamical decoupling sequence of N pulses, T_2^e is the decoherence time under a single pulse spin echo sequence, and γ is a scaling exponent $0.2 \lesssim \gamma \lesssim 0.7$. The signal decay then becomes

$$S_N(\tau) = e^{-(\frac{2N\tau}{T_2^{e,DD}})^p} S_N^{sim}(\tau) = e^{-(\frac{2N\tau}{N^{\gamma}T_2^e})^p} S_N^{sim}(\tau) \tag{6.10}$$

where p is the decay exponent of the envelope, $1 < p < 3$. For a typical $\gamma \approx 0.5$ and $p \approx 2$, this simplifies to a decay envelope of

$$S_N(\tau) = e^{-(\frac{2\tau}{T_2^e})^2 N} S_N^{sim}(\tau) \tag{6.11}$$

yielding a decay parameter of $\beta = (\frac{2\tau}{T_2^e})^2$, assuming no pulse errors. For the resonances studied above at $\tau \approx 1.372\,\mu$s, a T_2^e of $10\,\mu$s would yield $\beta \approx 0.075$, enough to measure $\alpha \gtrsim 1\,$kHz, assuming a sufficient hyperfine coupling.

However, some NMR studies [169] have demonstrated resolutions beyond the T_2^e limit by using extended sequences which also account for the phase information of the external field, so it is possible smaller parameters could be measured using a similar extension.

Combined with techniques which have used optically active defects to map nuclear spin networks [158], this gives a powerful method for characterizing the properties of molecules and defect complexes. For example, since the signals can be located to a single spatial location within a single molecule, this technique could be used to detect specific protein folding irregularities that might not be present in all such molecules. For bulk materials, this could be used to characterize location-specific properties of the surface termination of materials, or fingerprint the possible states of a defect complex.

NMR techniques may be used in a similar manner, but are limited to studying spin-$\frac{1}{/}2$ nuclei (such as Carbon-13 and Nitrogen-15) which are low abundance in nature and further requires a strong, controllable magnetic field. Since NQR may be used on higher spin nuclei, such as Nitrogen-14 which is more abundant nature, and has less strict requirements on the magnetic field it is more suitable for the study of naturally occurring molecules and solid materials.

6.10. Methods

The experimental sample and optical setup are as described in [170]. NV A is at the focus of a Solid Immersion Lens (SIL) surrounded by a circular antenna used for microwave control. Other NVs studied were within range of the antenna but not within the focus of the SIL, leading to reduced optical readout contrast. Magnetic fields were supplied by a permanent magnet and were measured and aligned using the $|m_S = 0\rangle$ to $|m_S = \pm 1\rangle$ ESR transitions

of the electronic spin. Magnetic fields for each experiment are listed in the Supplementary Info.

The experiment timing was controlled by a pair of Arbitrary Waveform Generators (AWGs). One (AWG520 Tektronix) was triggered to start the experiment and controlled the optical excitations and collection paths, including the AOM used to turn on the green (532nm) laser used for readout and initialization, and the data acquisition system (National Instruments, PCIe-6323). The AWG520 was also used to trigger another AWG (AWG7102 Tektronix) which was used to control the IQ modulation of a benchtop signal generator (SG384, Stanford Research Systems) which was fed into a high-isolation switch (ZASWA-2-50DR, Mini-Circuits) also controlled by the AWG7102. The output was fed through a USB-controlled microwave attenuator (Rudat 6000-60, Mini-Circuits) and broadband amplifier (ZHL-16W-43-S+, Mini-Circuits) before being delivered into the sample through a custom SMA-connected PCB which is in turn wirebonded to the antenna traces.

NV	**D** (kHz)	**E** (kHz)	**A** (kHz)	**P** (kHz)	α (kHz)	β
A	2859.20(02)	8.33(4)	2168.1(1)	4934.9	2.429(12)	0.0016(2)
B	2870.47(2)	7.51(4)	2164.7(1)	4939.5(1)		0.0039(3)
C	2870.39(2)	7.63(4)	2163.5(5)	4939.4(2)		0.0095(4)
D	2870.37(1)	7.58(3)	2165.0(3)	4939.2(1)		0.0175(6)
E	2872.20(03)	7.58(4)	2162.9(4)	4936.9(2)		0.0205(4)
F	2870.41(2)	7.04(3)	2162.9(4)	4940.7(2)		0.0082(4)

Table 6.1: Electronic Zero Field Splitting (ZFS) and Nitrogen-14 Quadrupolar parameters for each NV studied.

6.11. Supplementary Information

The supplementary information mentioned throughout this text can be found in Appendix B.

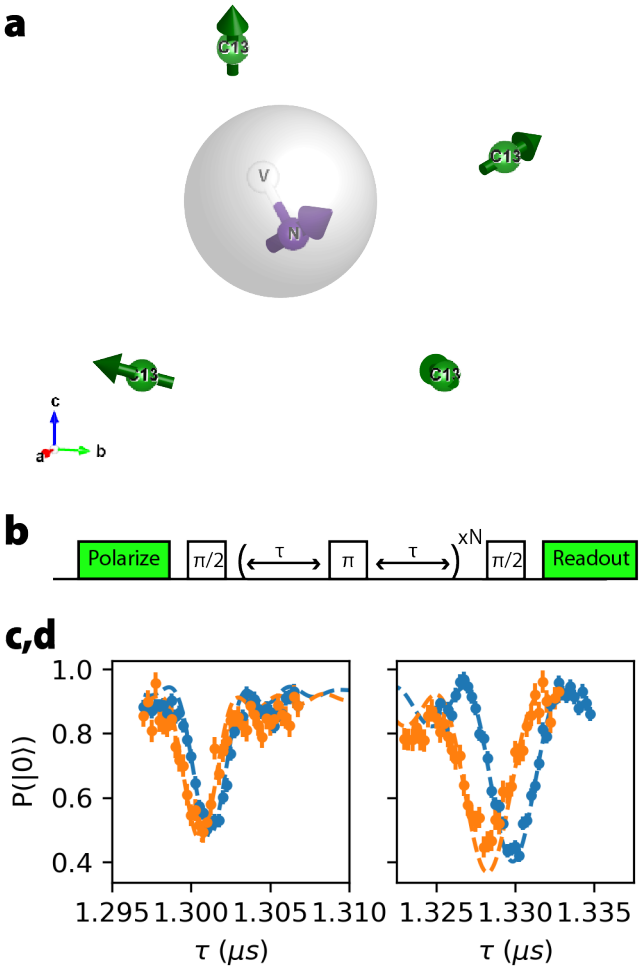

Figure 6.1: (a) Model of a typical NV center in diamond, with an electronic spin (gray) coupled to the intrinsic Nitrogen-14 nuclei (purple) and several Carbon-13 nuclei in the lattice (green). (b) Pulse schematic of a basic Dynamical Decoupling spectroscopy sequence. Initial and final $\frac{\pi}{2}$ pulses are in opposite directions, while decoupling π pulses are XY8 symmetrized. Pulses are applied on the $|m_S = 0\rangle$ / $|m_S = -1\rangle$ resonance of the electronic spin. Fine changes in the interpulse delay less than the hardware sampling rate are accomplished using interpolated sequences as described in [164] (c,d) Resonances corresponding to the $|m_I = \pm 1\rangle$ to $|m_I = 0\rangle$ transitions of the Nitrogen nuclear spin appear in the presence of an off-axis magnetic field. Spectra taken by sweeping τ for a fixed $N = 32$ DD sequence on two different NVs (NV A - blue, NV B - orange) are consistent with a significant difference in the Nuclear Quadrupolar hamiltonian. Data is shown with markers and simulation of the best fit results with dashed lines.

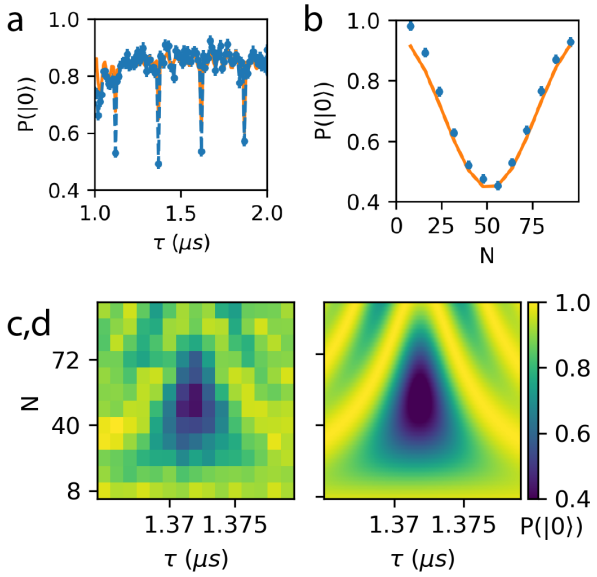

Figure 6.2: (a) Dynamical decoupling spectroscopy data taken on NV A (blue markers with dashed line) - taken by sweeping τ at a fixed $N = 32$ number of pulses - agree with the results from simulation (solid orange line). Extended oscillations come from coupling to four individually identified Carbon-13 nuclei, while periodic sharp dips originate from a new term in the Nitrogen-14 quadrupolar hamiltonian. (b) Data (blue markers) taken while sweeping the number of pulses at fixed $\tau = 1.372\,\mu$s agrees with simulations (solid orange line). The sub-unitary contrast of the oscillation is due to the approximately $\frac{2}{3}$ occupation probability of the Nitrogen-14 spin to be within the $|m_I = -1\rangle$ / $|m_I = +1\rangle$ manifold. (c) Data taken while sweeping both the inter-pulse delay (τ) and the number of pulses (N) is used to fit the strength of the new term in the quadrupolar hamiltonian. (d) The results of the best-fit simulation. Error bars in (c) are comparable to those in (a) and (b).

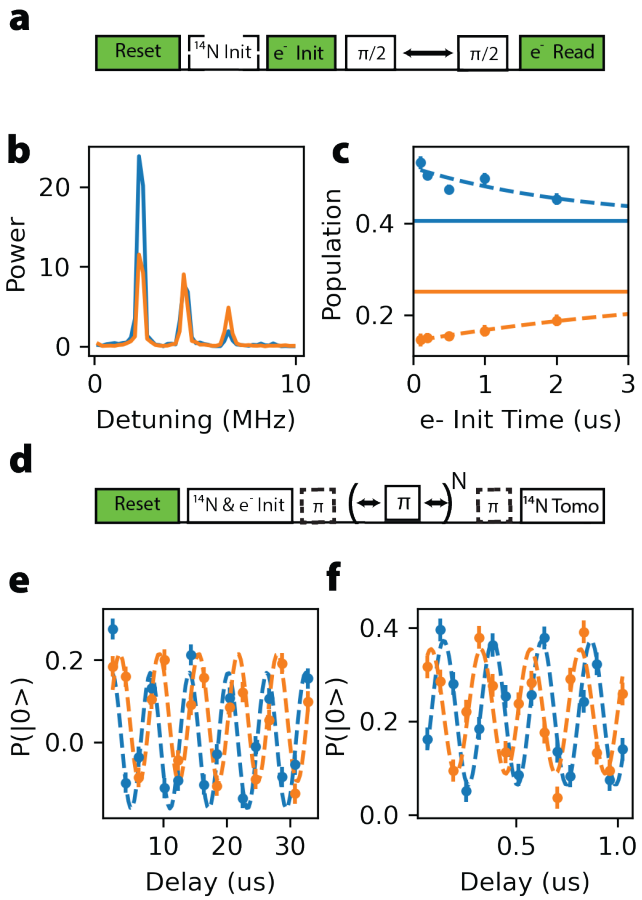

Figure 6.3: (a) Ramsey sequence used to measure initialization of the Nitrogen-14 nuclear spin. The initialization sequence used is described in the Supplementary Info. (b) Ramsey power spectra without (orange) and with (blue) a DD-based initialization sequence used to initialize the $|m_I = +1\rangle$ / $|m_I = -1\rangle$ manifold of the nitrogen-14 nuclear spin. Here, a long green laser pulse ($20\,\mu$s) is used to reset the system while a shorter (100 ns) laser pulse is used to reinitalize only the electron spin. Error bars are comparable in size to the markers used. (c) $|m_I = +1\rangle$ (blue markers) and $|m_I = -1\rangle$ (orange markers) populations fitted from Ramsey data while varying the amount of green time used to reinitialize the electron state. Exponential fits (dotted lines) show the population difference is expected to last several microseconds before returning to the steady state values (solid horizontal lines). (d) Pulse sequence used to measure the free induction decay of the Nitrogen nuclear spin. The nuclear tomography sequence used is described in the Supplementary Info. (e,f) Oscillations of the X (blue markers) and Y (orange markers) projection of the nitrogen nuclear spin within the $|m_I = +1\rangle$ / $|m_I = -1\rangle$ manifold during free evolution while the electron spin is in the (e) $|m_S = 0\rangle$ and (f) $|m_S = -1\rangle$ state. Fits (dashed lines) match the expected values for the frequency and direction of these oscillations.

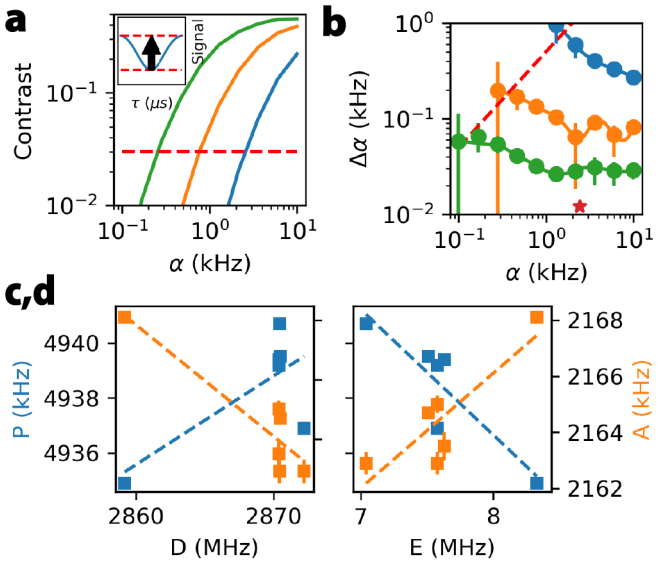

Figure 6.4: (a) Maximum signal obtained in simulation as α is swept for $\beta = 1\text{x}10^{-2}$ (blue), $3\text{x}10^{-2}$ (orange), and 0.1 (green). The point the signal surpasses the noise floor (red dashed line), which is chosen to be representative of our dataset, approximates the smallest η which can be measured. (b) Fit uncertainties obtained from simulated data as α is swept for various β parameters, using the noise floor indicated in a. A red star denotes the value of α and uncertainty obtained for NV A. Red dashed line indicates the level at which the uncertainty is equal to half of the α parameter, at which poing α is considered undetectable. (c,d) Plots of the measured P and A Nitrogen-14 parameters obtained from DD data for each NV, plotted against the D and E electron splitting parameters obtained from zero field ESR data. Dashed lines indicate linear fits. Error bars are approximately the same size as the markers.

CHAPTER 7

CONCLUSION AND FUTURE DIRECTIONS

The work presented in this thesis has shown significant advancements in the characterization of solid-state defect systems. In Chapter 3 we demonstrated that the optical properties of ensembles of defect-based emitters, even if they are heterogeneous, can be efficiently characterized across a broad parameter space, and we showed how that can be used to gain insights into the effects of growth and treatment of materials. We further demonstrated in Chapter 6 how the Hamiltonian of nuclear spins coupled to an optically-active electronic defect spin can be measured with unprecedented precision, opening a new window to both understanding the physics of these systems as well as the characterization of materials at the level of individual nuclei. This was in no small part enabled by the methods and infrastructure developed in Chapter 4.

However, the current process used to characterize defect systems is still very inefficient in the amount of equipment, power, time, and grad student labor required. While this thesis shows how new experiments can be generated quite easily, the current setup (which is comparable to most other state-of-the-art research setups) requires expensive equipment such as Arbitrary Waveform Generators (AWGs) that draw large amounts of power to run. Furthermore, the vast majority of data taken in the current method does not give much useful information, or is largely redundant. We recently addressed the first issue by demonstrating, in collaboration with the Aflatouni group, an integrated chip capable of generating the types of pulsed control sequences used in this thesis.[171] This low-power, reconfigurable, CMOS-based design replaces several large pieces of microwave equipment described in Section 4.1, and could open the door to real-time feedback methods which are currently prohibited by the overhead time and complexity required to control the equipment. The second issue could then be addressed by using methods which seek to estimate or "learn" the quantum Hamiltonian using adaptive sequences, which use the results from a previous experiment to determine which experiment to run next. A simple version of this would replace large,

high resolution Dynamical Decoupling spectra, such as the one shown in Fig. 5.2, with a coarser sweep. Then, finer data would only be taken around regions which show statistically significant deviations from the current model. If no significant deviations are found, another broad sweep at a different number of pulses or resonance order would be performed, and the algorithm repeated until a stopping conditions is reached (either a finite number of pulses / total sequence time or the eventual limit placed by T_2 decay).

Finally, once the system has been characterized, more efficient control sequences must be found. Since only the central electron spin can be efficiently polarized and controlled in the current architecture, nuclear polarization and control relies on long Dynamical Decoupling sequences. These must be performed at high resonance order to take advantage of the spectral isolation arising from the unique hyperfine coupling of each nuclear spin, leading to sequence times much longer than the fundamental limit placed by the intrinsic couplings. Several analytically-derived sequences have been proposed to enable more efficient nuclear polarization and nuclear-nuclear gates mediated by the electron spin. [172, 173] However, these still depend on spectral isolation at higher resonance orders to avoid crosstalk between nuclear spins with similar couplings. Instead, it is possible that even more efficient sequences can be found, using the parameters of known spins in the system to create sequences that directly account for other spin couplings - either using analytically methods or by closed-loop optimization based on simulations or experiments.

APPENDIX A

SUPPLEMENTARY INFORMATION: EFFICIENT OPTICAL QUANTIFICATION OF HETEROGENEOUS EMITTER ENSEMBLES

A.1. Height Measurements

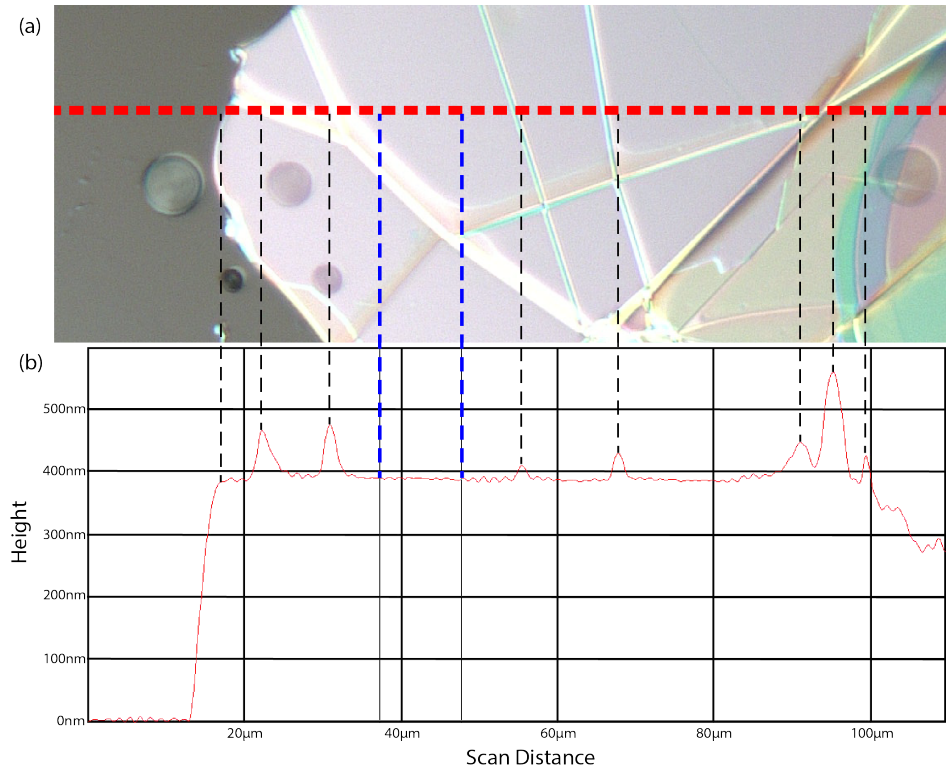

Figure A.1: a) Optical image and b) profilometer height measurement of the flake hosting regions B1 and B2. Features in the height measurement are correlated with the optical image using dashed lines. From this, the approximate location of the scan is indicated using a dashed red line. Between the two dashed blue lines, the average height is 388.1 nm.

Figure A.1 shows a profilometer height measurement of the flake hosting regions B1 and B2, along with an optical image of the flake. By correlating features in the height scan with features in the optical image (dashed black lines), we approximate the location of the profilometer scan (dashed red line). With the exception of optically visible ridges, the flake is flat in the region hosting region B1. The height is approximately 388.1 nm, based on the average height between the two dashed blue lines.

A.2. Tracking Emitters

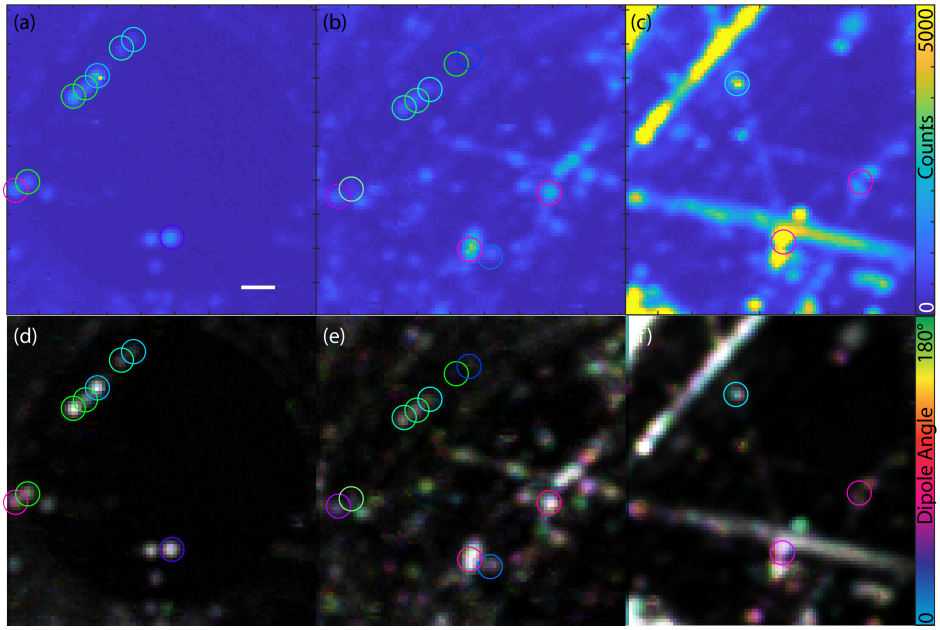

Figure A.2: Some emitters in Region B2 that seem to persist between treatments. (a-c) PL Intensity maps for Region B2 before treatment, after electron irradiation, and after annealing. (d-f) Polarization resolved PL, shown using a false color algorithm. Circles with fixed relative positions show emitters which may have persisted between treatments. The color of the circle represents the approximate polarization of the emitter. The white scale bar in (a) represents 1 µm.

Figure A.2 shows emitters which seem to persist between treatments in region B2. Eight emitters are identified before and after annealing, one of which is still visible after annealing. A combination of the consistent spatial layouts and similar dipole orientations support these identifications. The large-scale preservation of many emitters in similar locations supports our conclusion that irradiation does not significantly alter existing emitters, instead primarily creating new emitters. Three emitters identified after irradiation are also visible after annealing, including two which seem to have been created during irradiation. While not all emitters persist in the same location after annealing, two that did saw a significant increase in brightness, supporting our interpretation that annealing primarily increases the brightness

of emitters.

A.3. Emitter Model

We assume the emitters are point emitters, with Gaussian broadening from the laser beam width. Therefore, the total photoluminescence at a point is described by

$$I(r) = \sum_i A_i e^{\frac{-(r-r_i)^2}{2\sigma^2}}, \tag{A.1}$$

where $\sum_i$ is a sum over all the emitters, A_i describes an individual emitter's photoluminescence upon direct irradiation, $r - r_i$ is the distance from the emitter to the sampled point, and σ is the gaussian width of the beam.

For the scans used in this study this is a good approximation for the isolated emitters. In hBN scans, σ varies from 120 nm for a well-focused spot to 200 nm for the worst focused spots. This variation is due to the change in focus over large area scans. We take $\sigma = 150$ nm as a zeroth order approximation to the data, which is representative of the average over multiple isolated emitters in multiple scans. For the NV centers in planar diamond, σ varied from 195 nm to 220 nm, and $\sigma = 210$ nm was taken as the best approximation.

A.3.1. Single emitter

We start by analyzing the case of a single emitter randomly placed in the sample. For simplicity, we assume the sample is a square, with the understanding that as the sample size increases the large-scale geometry become insignificant due to the exponential decrease in response to far away emitters.

Probability of emitter position

To calculate the probability distribution of pixel intensities, we start with the probability distribution for separation between two points in a square of side length a, given by [174]

$$p(d) = 2d\left(-4\frac{d}{a^3} + \frac{\pi}{a^2} + \frac{d^2}{a^4}\right) \quad \text{for} \quad 0 < d < a\,, \tag{A.2}$$

where we implicitly assume the probability density to be zero elsewhere. There is, of course, a small probability for $a < d < \sqrt{2}a$, but we ignore this as it creates only an exponentially small correction to I.

We can then use the formula

$$p(I) = p(d(I))\frac{d}{dI}(d) \tag{A.3}$$

with the gaussian

$$I(d) = Ae^{\frac{-d^2}{2\sigma^2}} \tag{A.4}$$

to get the photoluminescence probability density from a single emitter of known brightness

$$p(I|A) = \frac{2\sigma^2}{Ia^2}\left(\pi - \frac{4\sqrt{2}\sigma\sqrt{log(-\frac{I}{A})}}{a} + \frac{2\sigma^2 log(-\frac{I}{A})}{a^2}\right) \quad \text{for} \quad e^{\frac{-a^2}{2\sigma^2}} < \frac{I}{A} < 1\,. \tag{A.5}$$

Because we have ignored the slight probability of $a < d < \sqrt{2}a$, this is not quite normalized, having a total probability of $\frac{-13+6\pi}{6} \approx 0.975$. So we impose

$$p(I|A) = \left[1 - \int_{Ae^{\frac{-a^2}{2\sigma^2}}}^{\infty} p(I|A)dI\right]\delta(I) \quad \text{for} \quad \frac{I}{A} < e^{\frac{-a^2}{2\sigma^2}}\,, \tag{A.6}$$

ignoring the fine structure of these very small intensities (which becomes exact in the large $\frac{a}{\sigma}$ limit). Note that this normalization factor will change once we quantize our model below, but the same formula is used to ensure normalization.

Averaging over brightness distribution

In the previous section, we fixed the brightness of a single emitter to A, but the inhomogeneous emitters observed in the samples studied require a more general brightness distribution. We begin by assuming the brightness of emitters is uniformly distributed between 0 and some maximum brightness, A_{max}. Then, we have the averaged single-emitter probability density

$$p(I|[0, A_{max}]) = \frac{\int_0^{A_{max}} p(I|A)dA}{A_{max}}, \tag{A.7}$$

where $p(I|A)$ is the intensity distribution given A, as specified above. This yields an analytical solution, according to Mathematica, of

$$p(I|[0, A_{max}]) = \frac{2\sigma^2}{IA_{max}a^2} \times \left[\pi(A_{max} - I) + 2\frac{\sigma^2}{a^2}((I - A_{max}) + A_{max}log(\frac{A_{max}}{I}))\right] \quad \text{for} \quad e^{\frac{-a^2}{2\sigma^2}} < \frac{I}{A_{max}} < 1\,. \tag{A.8}$$

We can then easily convert this to a uniform distribution between a minimum and maximum intensity by

$$p(I|[A_{min}, A_{max}]) = \frac{A_{max}p(I|[0, A_{max}]) - A_{min}p(I|[0, A_{min}])}{A_{max} - A_{min}}\,. \tag{A.9}$$

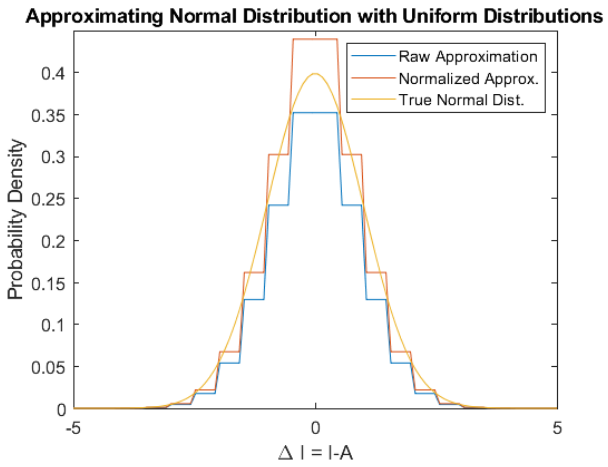

Figure A.3: A simple approximation of a Normal Distribution by flat uniform distributions. The normalized approximation is used to optimize the numerical efficiency of the model.

With a fast numerical formula to generate flat distribution probability densities, we can approximate normal distributions to arbitrarily accuracy as a weighted sum of uniform distributions between these points. This can be made precise by increasing the number of uniform distributions, at the cost of additional computational overhead. Since the normal distribution is concave, this is a strictly lower approximation, so to ensure densities are not affected by this we also normalize the approximation. For brevity and clarity, we present this graphically, in Fig. A.3, rather than algebraically. This gives us our final probability density for a normally distributed family of emitters as a weighted sum of uniform distributions

$$p(I|N(A,\sigma)) \approx \sum_i w_i p(I|[A-s_i, a+s_i])\,. \tag{A.10}$$

A.3.2. Multiple emitters

PDF for n emitters

Denoting the probability density we calculated for a single emitter as $p_1(I)$, we can calculate the brightness probability density for two emitters as the self-convolution

$$p_2(I) = (p_1 \circledast p_1)(I)\,, \tag{A.11}$$

where we have assumed the emitters are drawn from the same brightness distribution, but are otherwise independent in density and brightness. Similarly for n emitters,

$$p_n(I) = (p_{n-1} \circledast p_1)(I) = \underbrace{(p_1 \circledast ... \circledast p_1)}_{n\text{-times}}(I)\,. \tag{A.12}$$

Note that, using recursive methods, this convolution can be done in $O(log(n))$ time, making it computationally feasible for even a large number of defects. For consistency and obvious physical reasons, we define the zero emitter distribution

$$p_0(I) = \delta(I)\,. \tag{A.13}$$

Averaging over number of emitters

If the probability of having n emitters is labeled P_n, the total probability distribution is then

$$p(I|P_n) = \sum_{n=0}^{\infty} P_n p_n(I)\,. \tag{A.14}$$

We assume a large area, a^2, and therefore a number of emitters $N = a^2\eta$, where η is the density of emitters. To make this a continuous parameter, we set

$$P_{\lfloor N \rfloor} = (\lceil N \rceil - N), \quad P_{\lceil N \rceil} = (N - \lfloor N \rfloor), \quad \text{and} \quad P_n = 0 \quad \text{otherwise}\,, \tag{A.15}$$

where $\lfloor N \rfloor$ and $\lceil N \rceil$ are the floor and ceiling functions, respectively. Note that, since the number of emitters in a scan is fixed, we do not use a Poisson distribution here.

Multiple families of emitters

To handle m families of emitters, each with their own photoluminescence probability distribution $p^i(I)$ with $i = 1...m$, we convolve the probability distributions together:

$$p_{emitters}(I) = (p^1 \circledast ... \circledast p^m)(I)\,. \tag{A.16}$$

A.3.3. Background Intensity

A Poisson background distribution was used to fit the background, giving a single background parameter, λ, and thus

$$p(I) = \left(p_{emitters} \circledast p_{background}(\lambda)\right)(I)\,. \tag{A.17}$$

Since the intensities in this study rise well above unity, we approximate a Poisson distribution by a normal distribution with equal mean and variance.

A.3.4. Parameterizing the model

With the above discussion informing our choices, we therefore parameterize the model in terms of m underlying densities and brightness distributions with a single background parameter

$$p(I|\eta_m, A_m, \sigma_m, \lambda) = \overset{M}{\underset{m=1}{\circledast}} \left(\sum_n P_n(\eta_m) p_n(I|A_m, \sigma_m) \right) \circledast \text{Poiss}(I|\lambda) \tag{A.18}$$

A.3.5. Quantizing the Model

Throughout this analysis, we have taken both I and A to be continuous variables, allowed to take on any positive real value. However, since the data is recorded in photon counts, only integer values are possible for I. To account for both of these, we sampled the probability distributions for this model in quantized steps, replacing, e.g., integrals with weighted sums. Ideally sampling would occur at every whole number to capture the fundamental quantization of I; however, for scans with very bright emitters, it was necessary to increase this quantization further to improve the computational time necessary to optimize the parameters, as described below. In every case, this quantization was well below the counts and each of the model parameters, meaning it should not significantly affect the accuracy of the model.

Since the underlying probability distributions are quantized, we also similarly quantize the model parameters, which further reduces the parameter space and allows for better parameter estimation.

A.3.6. Parameter Estimation

First, a region of interest is defined - which may be used to mask out regions of clearly different properties (supported vs unsupported, avoiding extended defects, etc). From this a distribution of pixel intensities is defined, grouped into an appropriate number of bins. We then set a number of emitter families, n, and run an optimization algorithm to determine the best model parameters to approximate the data distribution,

$$\mathbf{x} = [\eta_1, A_1, \sigma_1, ...\eta_n, A_n, \sigma_n, \lambda]\,. \tag{A.19}$$

Our optimization target function is the Neyman modified chi-squared parameter,

$$\tilde{\chi}^2 \equiv \sum_i \frac{(p_i(\mathbf{x}) - m_i)^2}{max(m_i, W)}\,, \tag{A.20}$$

where the sum is taken over the data bins, $p_i(\mathbf{x})$ is the predicted number of pixels in the bin from the above model distribution given the parameter vector $\mathbf{x}$, and m_i is the measured number of data pixels in that bin. W is a parameter which accounts for the fact that our model is not exact, and prevents rare occurrences not described by the model from overwhelming the fit. W is chosen to be 1, so ideally $W \approx \frac{\tilde{\chi}^2}{N} \approx 1$ [175].

We use the Matlab implementation of Differential Evolution [176] to optimize this function, with the following constraints:

- The density of each emitter family must be large enough to have at least one defect in the sample area, but not so large that there is more than one defect per square Gaussian blur.
- The brightness of each emitter family must be larger than zero, but less than the maximum brightness of a single pixel in the sample minus the background parameter.
- The density of each each emitter family must be larger than the density of pixels of the family's average brightness expected due to the Poisson background
- The width of each emitter family must be larger than the Poisson width expected due to the family's brightness, but not larger than the family's brightness itself (otherwise it would predict negative brightness defects)

In addition, to decrease the parameter space volume (which increases the density of points sampled by the differential evolution algorithm), we restricted the parameters to be within

an order of magnitude either way of the initial guess parameters (for emitter parameters) or within a factor of 2 for the background parameter (which is more tightly constrained). This is large enough to capture the behaviors we are looking for while still allowing for repeatable and accurate convergence of the optimization algorithm. Further rounds of convergence with even smaller windows were used to find better parameters, with the best parameter set (according to the Akaike Information Criteria, see below) always kept.

A.3.7. Parameter Uncertainties

To estimate the uncertainty, we assume that, near the minima, the chi-squared function looks parabolic:

$$\tilde{\chi}^2(\mathbf{x}) \approx \tilde{\chi}^2(\mathbf{x_0}) + \frac{1}{2}(\mathbf{x}-\mathbf{x_0})^T H(\mathbf{x_0})(\mathbf{x}-\mathbf{x_0})\,, \tag{A.21}$$

where $\mathbf{x}$ is the vector of parameters, $\mathbf{x_0}$ is the argument of the minimum chi-squared, and $H(\mathbf{x_0})$ is the Hessian at $\mathbf{x_0}$. $H(\mathbf{x_0})$ is calculated numerically using the DERIVEST suite. In cases where $H(\mathbf{x_0})$ is not positive definite, which is possible due to shallow or insufficiently converged minima, negative eigenvalues are corrected by finding the distance along that eigenvector necessary to produce a change in χ^2 of 1. Using the formula for log likelihood [175],

$$log(\mathcal{L}) = -\frac{\tilde{\chi^2}}{2} + \text{const}\,, \tag{A.22}$$

where $\mathcal{L}$ is the likelihood of the estimated parameters, we estimate the standard errors to be

$$\epsilon_i \approx \sqrt{(H(\mathbf{x_0})/2)^{-1}_{ii}}\,. \tag{A.23}$$

To get 95% confidence intervals, we multiply the standard errors by 1.96.

A.3.8. Selecting number of Defect Families

To select the optimal number of families, we need a "goodness of fit" metric which allows us to compare fits with different numbers of parameters. Here we use the Akaike Information Criteria (AIC), defined by

$$AIC = \tilde{\chi}^2(\mathbf{x_0}) + 2 \times \text{length}(\mathbf{x}) + \text{const}\,, \tag{A.24}$$

where a lower AIC is considered to represent a better fit. Note that we again use the expression for log likelihood in terms of the modified Neyman chi-squared parameter. We start with zero emitter families, and produce optimal fits for increasing number of families until the AIC begins to increase. We then take the best AIC and assume that represents the "best" fit with the optimal number of emitter families.

A.3.9. Testing the Model

To test our model and fitting procedure, we apply it to simulated datasets with known parameters. These simulations mirror the assumptions in our analysis - namely, emitters with brightnesses drawn from multiple normal distributions are placed randomly onto a Poissonian background with fixed densities. Throughout our experimental datasets, most backgrounds seem to be around 100 counts with little variation between samples (prior to annealing). We therefore fix our background to be $\lambda = 100$ counts. This sets a noise floor of $\sqrt{\lambda} = 10$ counts, which in turn sets a scale for the brightness of emitters. The result of simulating one emitter family, well above this scale, is shown in the main text in Fig. 2(d-f). As shown there, the density and brightness of emitters found by the fitting procedure agrees with the true underlying parameters used in the simulation (as determined by the 95% confidence interval of the fit). In addition, the best-fit background of 100.11(39) counts agrees with the simulated background parameter of 100 counts.

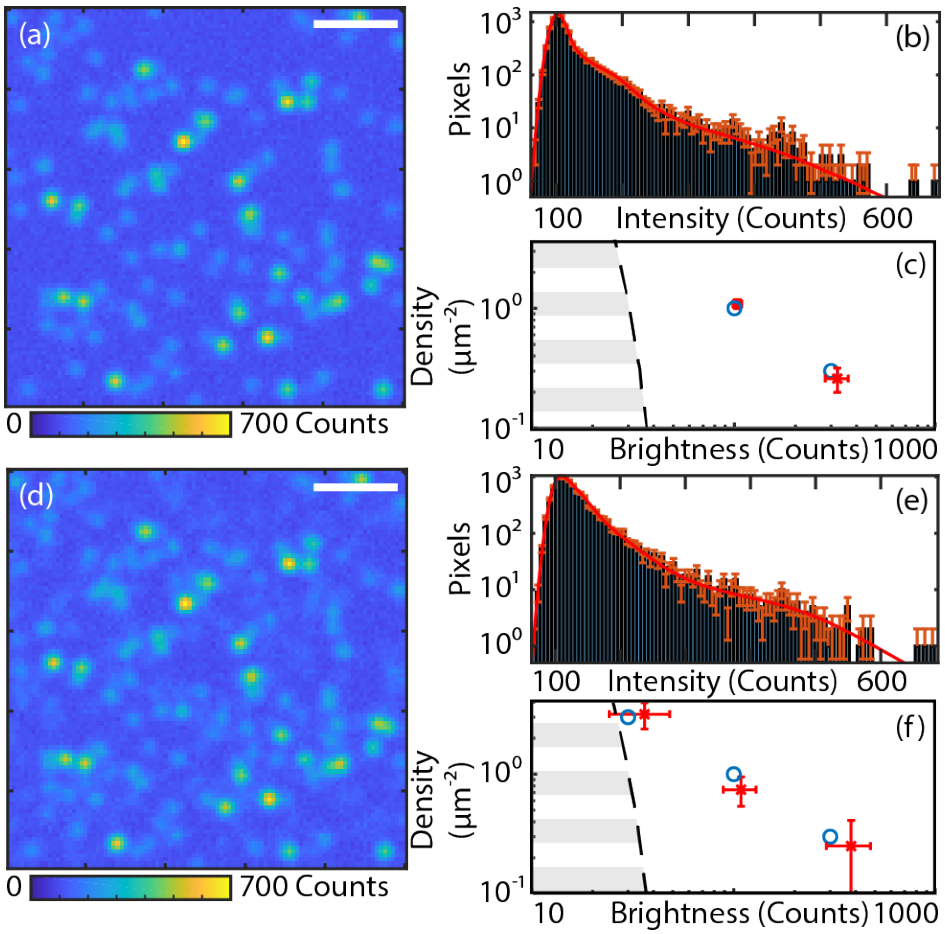

Figure A.4: a,d) Simulations similar to the one presented in FIG.2(d) in the main text, but with two and three emitter families, respectively. (b-c, e-f) Corresponding pixel intensity histograms and emitter family parameter plots. The emitter family parameters found by fitting agree with the underlying simulation values, shown by blue circles. Scale bars in (a,d) represents 2 µm. Error bars in (c,f) represent 95 % confidence intervals.

Figure A.4 presents similar simulations with two and three families. Figure A.4(a) shows a simulation that adds an additional emitter family that is brighter but less dense than the first one. Again, the fitted family parameters shown in Fig. A.4(c) are in agreement with the underlying simulation values, and the true background of 100 counts is within the uncertainty range of the fitted background, 99.75(28) counts.

Figure A.4(d) shows a simulation that further adds a dim, very dense emitter family that is difficult to distinguish by eye. And again, the fitted family parameters shown in Fig. A.4(e)

are in agreement with the underlying simulation values, and the true background of 100 counts is within the uncertainty range of the fitted background, 100.6(18) counts. We note, however, that the fits are less accurate and the confidence intervals have increased, as expected due to the larger number of parameters. However, this shows that the model is able to capture multiple families accurately.

A.4. Samples

Region	Flake Thickness	1st Treatment	2nd Treatment
A1	215nm	2×10^{16} e$^-$/cm^2 3keV irradiation	30 min 850 °C Ar Anneal
A2	240nm	2×10^{16} e$^-$/cm^2 3keV irradiation	30 min 850 °C Ar Anneal
B1	390nm	2×10^{17} e$^-$/cm^2 3keV irradiation	30 min 850 °C Ar Anneal
B2	250-350nm	2×10^{17} e$^-$/cm^2 3keV irradiation	30 min 850 °C Ar Anneal
C1	630nm	(Ambient chamber conditions)	30 min 850 °C Ar Anneal
C2	60nm	(Ambient chamber conditions)	30 min 850 °C Ar Anneal
C3	>300nm	(Ambient chamber conditions)	30 min 850 °C Ar Anneal
D1†	*	30 min 850 °C Ar Anneal	4×10^{15} e$^-$/cm^2 3keV irradiation
D2	*	30 min 850 °C Ar Anneal	6×10^{15} e$^-$/cm^2 3keV irradiation
D3	*	30 min 850 °C Ar Anneal	1×10^{16} e$^-$/cm^2 3keV irradiation
E1	200-250nm	2×10^{16} e$^-$/cm^2 of 5keV irradiation	30 min 850 °C Ar Anneal

Table A.1: A table of the regions studied and the treatments used.
* Thickness information is not available for these regions. † This region underwent an additional 30 min 850 °C Ar Anneal after being irradiated.

Table A.1 shows all regions for which data was taken, including the thickness of the flakes near the suspended regions. Regions B1 and B2 are on the same flake. Regions D1-D3 were exfoliated from a different bulk crystal and underwent an O_2 plasma clean prior to initial imaging.

A.5. Additional Emitter Distributions

Figure A.5 and shows emitter distributions similar to those shown in Fig. 4 in the main text, but for regions which received only indirect irradiation followed by annealing. The pre-treatment emitter distribution in Fig. A.5(a) is similar to that presented in Fig. 4(a) of the main text, dominated by a peak around 40 counts, with additional smaller peaks at

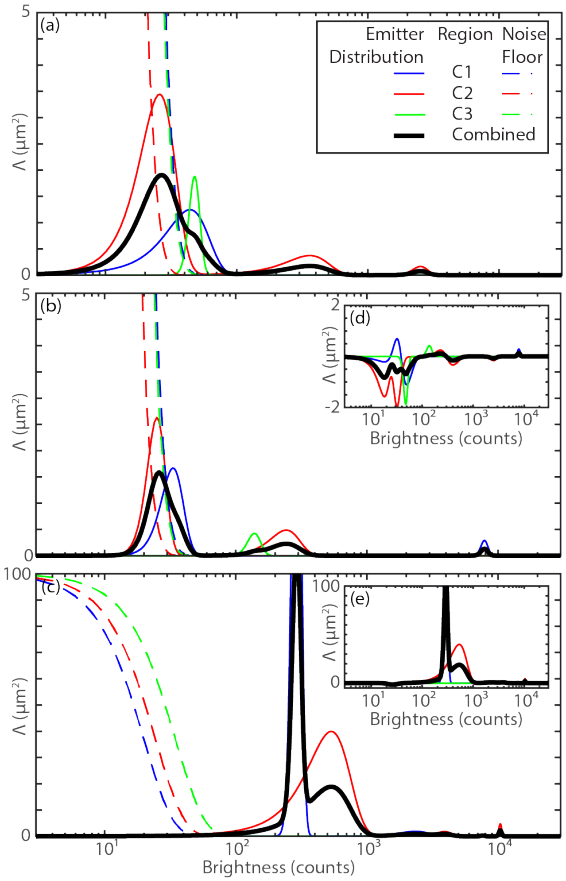

Figure A.5: Emitter distributions for regions which received indirect irradiation prior to annealing; distributions for each region a) before treatment, b) after irradiation, and c) after annealing are shown. Changes are shown for the d) pre-treament to post-irradiation and e) post-irradiation to post-annealing distributions.

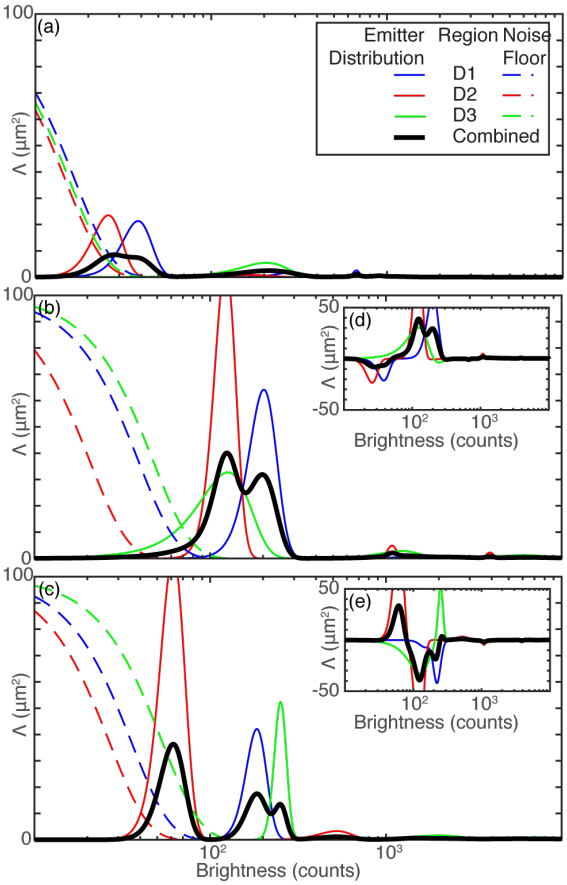

Figure A.6: Emitter distributions for regions which received annealing prior to direct irradiation; distributions for each region a) before treatment, b) after annealing, and c) after irradiation are shown. Changes are shown for the d) pre-treament to post-annealing and e) post-annealing to post-irradiation distributions.

higher brightnesses. After receiving only indirect exposure, the distribution in Fig. A.5(b) shows the same peaks but with decreased densities, which we attribute to photobleaching. In addition, a small peak at high brightness appears, which is attributed to irradiation from stray ions caught in the accelerating voltage. After annealing, a huge density of emitters is found between 100 and 1000 counts, which we attribute to emitters present before annealing

but below the noise floor becoming much brighter. In addition, smaller peaks are found above 1000 counts, which we attribute to brightening of emitters already visible in the sample.

Fig. A.6 shows emitter distributions for regions which were annealed prior to being irradiated. Fig. A.6(a) shows a pre-treatment emitter distribution which much denser broader than those in Fig. A.5(a) or Fig. 4(a), which we attribute to the flakes being exfoliated from a different bulk crystal. After annealing, the distributions in Fig. A.6(b) become much brighter and denser. In addition, the background of two of the three regions increased significantly. We attribute these effects to both already visible emitters becoming brighter, as well as emitters from below the noise floor rising above it. After irradiation, the distributions in Fig. A.6(c) are both slightly dimmer and slightly less dense than those in Fig. A.6(b). We attribute this again to photobleaching, and note that, based on the changes in Fig. 4(b) of the main text, the effects of the low dosage of irradiation used would not be visible on this scale.

A.6. Raw Data

In the online electronic supplement, available at ******, we present the raw data acquired in the study as well as the parameter plots from the corresponding fits. For each stage of the treatment, the PL map is shown with a 1 µm scale bar, and the suspended region is outlined in red. For regions where supported photoluminescence near the edge of the suspended region appear to bleed into the suspended region, a buffer uniformly shrinks the suspended region (so as to not introduce any sampling bias). Pixel histograms and model fits accompany each PL map.

APPENDIX B

SUPPLEMENTARY INFORMATION: QUADRUPOLAR RESONANCE SPECTROSCOPY OF SINGLE NUCLEAR SPINS

B.1. ESR and Ramsey

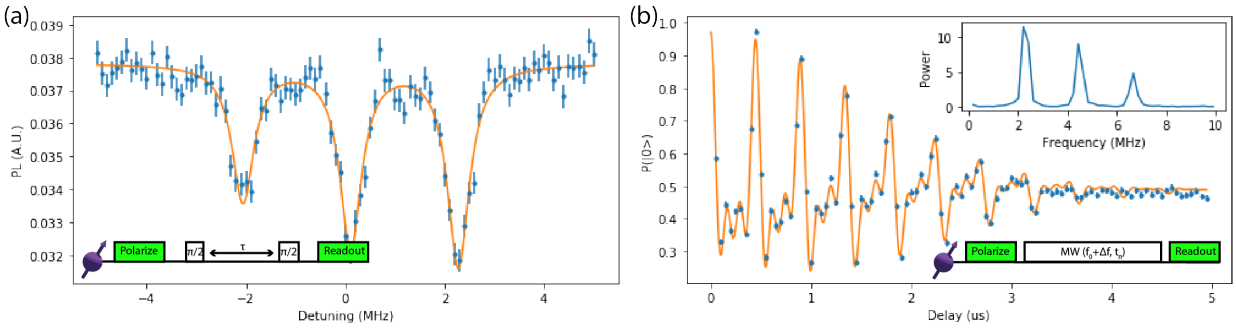

Figure B.1: (a) ESR and (b) Ramsey data (blue points) from NV A. Fits (solid orange lines) are consistent with a model containing only the nitrogen-14 nuclear spin coupling, with no other strongly coupled spins detected.

With natural isotopic abundance, we expect around 1.1% of the carbon nuclei in the diamond lattice to be carbon-13. In bulk electronics grade samples, this means we expect a "typical" NV center to have a few carbon-13 nuclei coupled in the 10 to 100 kHz range, as well as the NV's intrinsic nitrogen-14 nucleus with ≈ 2.17 MHz coupling. It is possible to have more strongly coupled carbon-13 nuclei, but ESR and Ramsey data on this sample (Fig. B.1) are consistent with a model including only the nitrogen-14 nuclear spin and no other strongly coupled nuclei ($|A_Z| \gtrapprox \frac{1}{T_2^*} \approx 300$ kHz, where $|A_Z|$ is the strength of the on-axis component of the elecro-nuclear hyperfine coupling).

B.2. Dynamical Decoupling

Dynamical decoupling spectroscopy is expected to reveal several more weakly coupled C-13 nuclei (with $\frac{1}{T_2^*} \gtrapprox |A_Z| \gtrapprox \frac{1}{T_2} \approx 10$ kHz). Indeed, we observe resonances associated with at least four C-13 nuclei within the data shown in Fig. B.2. However, the data also contain an unexpected, higher-frequency resonance series in addition to the expected carbon-13 resonances. The resonance series corresponds to a frequency of several MHz, and it is stable to reorientation of the external DC magnetic field (up to at least $\pm 3°$).

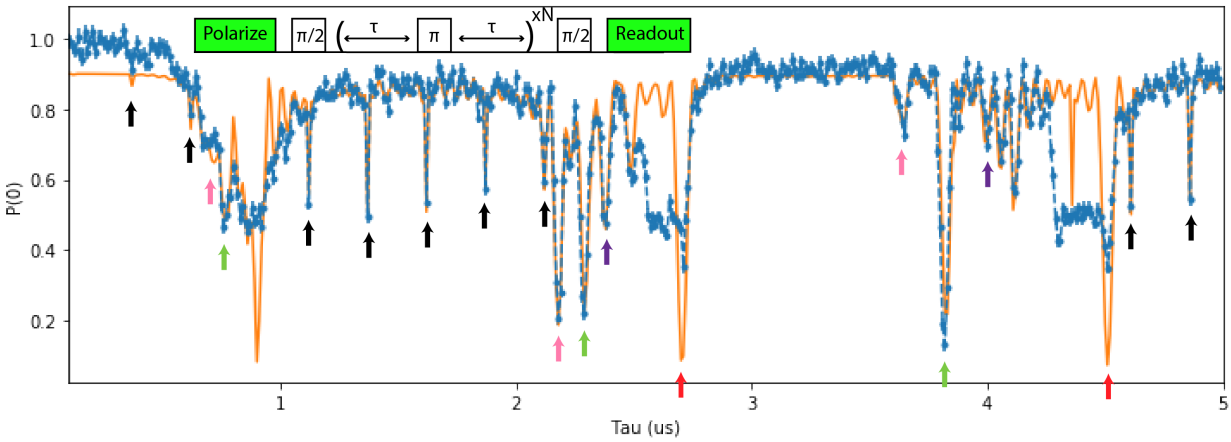

Figure B.2: Dynamical decoupling data (blue points w/ dashed line) shows resonances associated with multiple individual carbon-nuclei (colored arrows), as well as a resonance series associated with a higher energy spin (black arrows). Simulation (solid yellow line) shows this is consistent with an additional term in the nitrogen-14 nuclear quadrupolar Hamiltonian, as well the known carbon-13 nuclei. Data is taken with $N = 32$ pulses at a magnetic field of 264 Gauss aligned within $\approx 1^\circ$ of the NV axis. (Inset) High resolution data (markers) taken for various N around $\tau = 1.372$ us fitted using our in-house simulator (best-fit simulation represented by dashed lines). Based on this we determine α is 2.43(2) kHz for the Nitrogen-14 nuclear spin.

B.3. Fitting hyperfine and quadrupolar parameters

To fit the value of both the hyperfine and quadrupolar parameters of the Nitrogen nuclear spins in the NVs studied, the number of Dynamical Decoupling pulses was swept while looking at a narrow region around a high order resonances for each the $|m_I = 0\rangle$ to $|m_I = \pm 1\rangle$ transitions. The resonances were chosen to avoid features related to Carbon-13 nuclei coupled to each NV. The data for both resonances was simultaneously fitted to a simulation based on the hamiltonian given in the main text for each NV, with the hyperfine and quadrupolar parameters allowed to vary. Additional variation parameters were added to account for the loss of coherence due to pulse imperfections and dephasing of the NV electron spin during the DD sequence. Data for each NV listed in the main text is shown in figure Fig. B.3

For NV A, data was taken around the new resonance described in the main text while

sweeping the pulse number. Again, the data collected was fitted using a simulation which includes the new quadrupolar parameter described in the main text.

B.4. Nuclear Spin Initialization and Tomography Sequences

Based on our fitted simulations, we find that $N = 24$ pulses at a spacing of $\tau = 1.372\,\mu s$ gives an approximate $\frac{\pi}{2}$ rotation between the $|m_I = -1\rangle$ and $|m_I = +1\rangle$ states of the Nitrogen-14 nuclear spin conditional on the state of the electron spin within the $|m_S = 0\rangle$ / $|m_S = -1\rangle$ manifold (see Fig1(b) of main text). Furthermore, simulations show that a high-fidelity unconditional Z rotation on the $|m_I = \pm 1\rangle$ manifold of the Nitrogen-14 spin can be implemented using a single pulse on the $|m_S = 0\rangle$ / $|m_S = -1\rangle$ electron spin manifold, due to the small magnitude of the off-axis term in the nuclear quadrupolar hamiltonian.

Using these two-qubit gates, we implement nuclear initialization and tomography sequences adapted from [157], as depcited in Fig. B.4.

B.5. Initialized Ramsey

Raw Ramsey data for each electron re-initialization length is shown in Fig. B.5. Data for the steady state Ramsey is repeated from Fig. B.1

B.6. Simulations

Simulations throughout the manuscript were performed using exact simulation of the described Hamiltonians, along with the well-known Hamiltonian for the electronic spin of the negatively charged NV center at room temperature. Only spin degrees of freedom are considered, while optical and charge dynamics are assumed to be normalized away by readout calibrations which are interleaved with the experiments. Decoherence dynamics are modeled as a uniform decay of this signal, using the form described in Equation (8) of the main text. Hyperfine and quadrupolar parameters are extract from data by allowing these param-

eters to vary in the simulations and fitting the simulation results to the data using general optimization methods.

In Figure 4, simulation are performed without (a) and with (b) Gaussian noise which is representative of the dominant shot-noise in our experiments. In Figure 4(a), the maximum contrast is obtained by sweeping the number of pulses and measuring the largest contrast obtained, where contrast is defined as the depth of the resonance peak divided by the total readout contrast (normalized to be 1). In Figure 4(b), simulations were performed and random noise was added in, using a noise amount characteristic of our experiments. For each value of β, the α parameter in simulation was reduced until the uncertainty in the fit dropped below the actual signal.

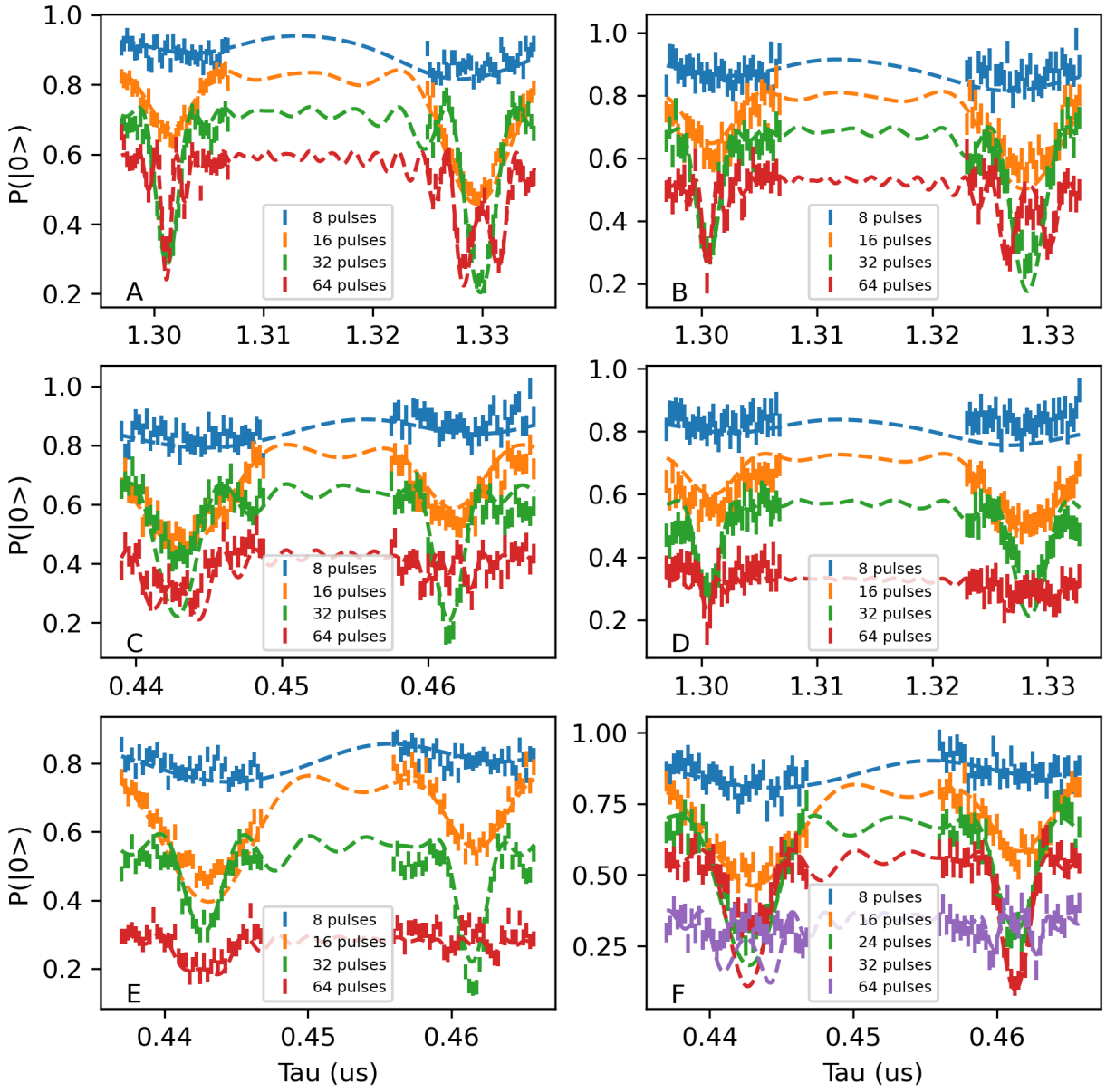

Figure B.3: Dynamical decoupling data for each NV studied, showing resonances associated with $|m_I = 0\rangle$ to $|m_I = \pm 1\rangle$ transitions of the Nitrogen-14 nuclear spin as the number of dynamical decoupling pulses is swept. Pulse spacings below the hardware limit ($\approx 1\,\text{ns}$) are achieved using interpolated sequences [164]

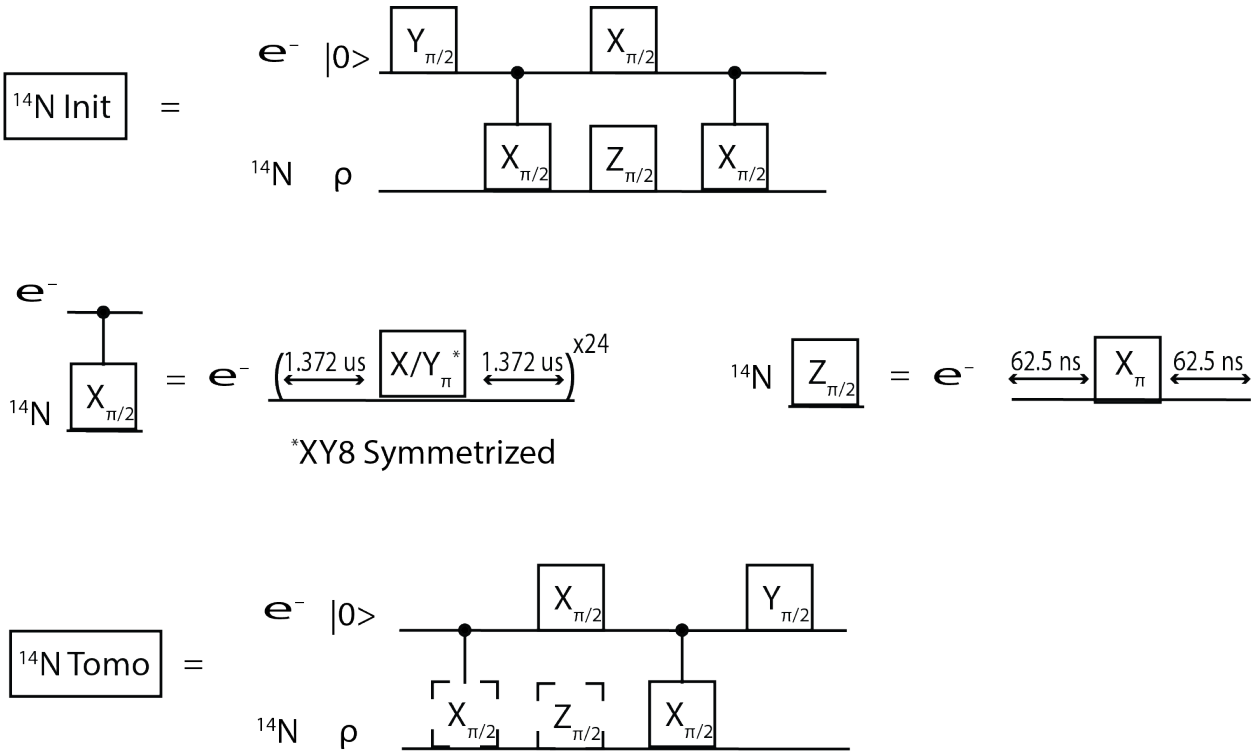

Figure B.4: Sequences used to initialize and read out the nuclear spin state using the electron spin. Dashed gates in the tomography sequence are included or removed depending on the desired nuclear measurement axis.

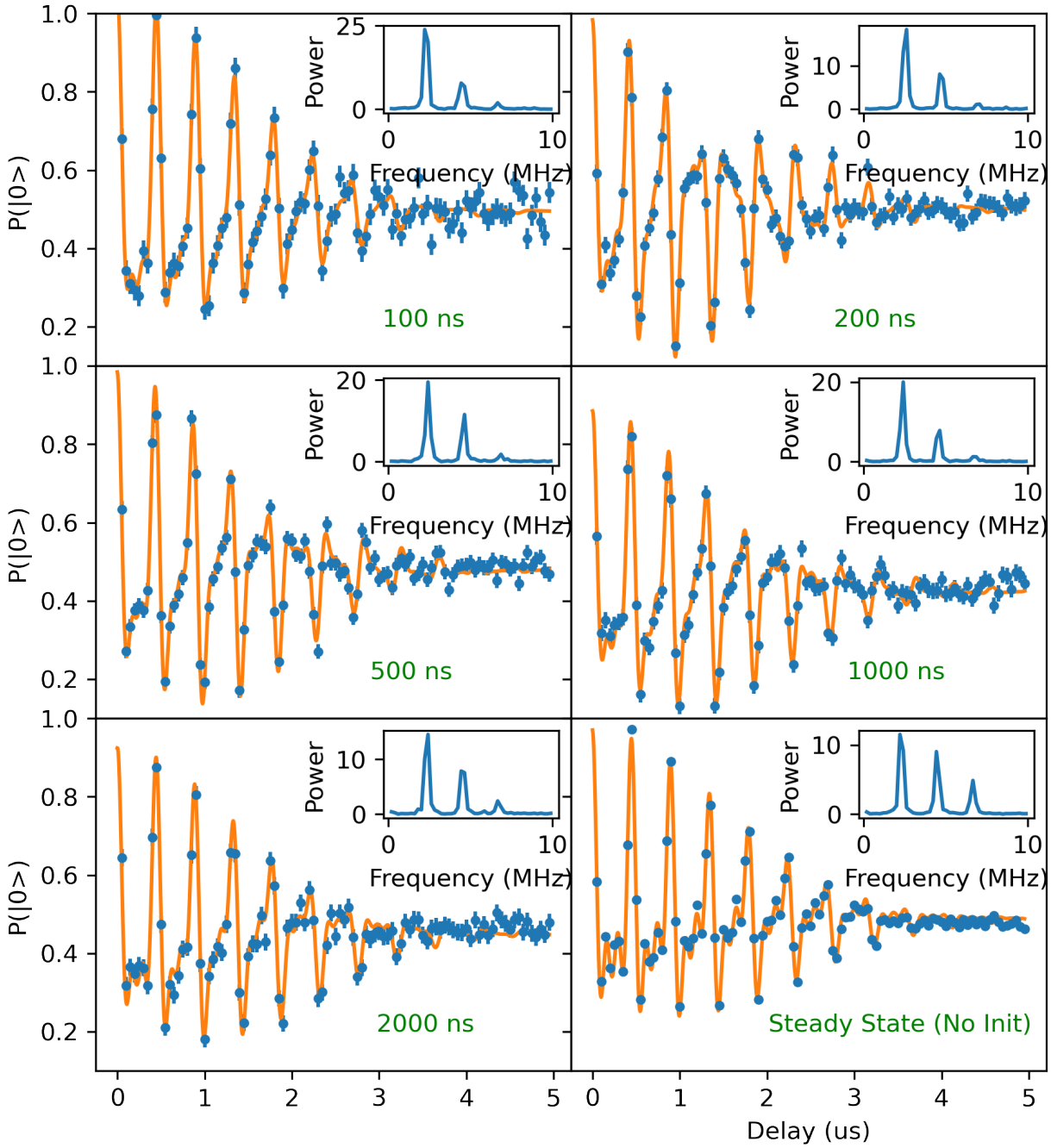

Figure B.5: Initialized Ramsey experiment for each of the electron re-initialization times, as depicted in Fig3(a) of the main text. Blue markers are data and yellow lines are oscillatory fits used to extract the occupation parameters of the Nitrogen-14 spin. (Insets) Power spectra for each of the Ramsey experiments - the polarization of the Nitrogen-14 spin is apparent from the unequal height of the frequency peaks.

BIBLIOGRAPHY

[1] Maxwell Planck. *The theory of heat radiation, second edition.* translated by M. Masius, Blakiston's Son Co, Philadelphia, 1914.

[2] Professor E. Rutherford F.R.S. Lxxix. the scattering of α and β particles by matter and the structure of the atom. *The London, Edinburgh, and Dublin Philosophical Magazine and Journal of Science*, 21(125):669–688, 1911.

[3] J. S. Bell. On the einstein podolsky rosen paradox. *Physics Physique Fizika*, 1:195–200, Nov 1964.

[4] Michael A Nielsen and Isaac Chuang. Quantum computation and quantum information, 2002.

[5] Yuri I. Manin. Vychislimoe i nevychislimoe [computable and noncomputable] (in russian). *Sov. Radio*, pages 13–15, 1980.

[6] Richard P. Feynman. Simulating physics with computers. *International Journal of Theoretical Physics*, 21(6):467–488, Jun 1982.

[7] David Deutsch and Roger Penrose. Quantum theory, the church–turing principle and the universal quantum computer. *Proceedings of the Royal Society of London. A. Mathematical and Physical Sciences*, 400(1818):97–117, 1985.

[8] P.W. Shor. Algorithms for quantum computation: discrete logarithms and factoring. In *Proceedings 35th Annual Symposium on Foundations of Computer Science*, pages 124–134, 1994.

[9] Lov K. Grover. A fast quantum mechanical algorithm for database search. In *Proceedings of the Twenty-Eighth Annual ACM Symposium on Theory of Computing*, STOC '96, page 212–219, New York, NY, USA, 1996. Association for Computing Machinery.

[10] Seth Lloyd. Universal quantum simulators. *Science*, 273(5278):1073–1078, 1996.

[11] David P. Divincenzo. The Physical Implementation of Quantum Computation. *Fortschritte der Physik*, 48(9-11):771–783, January 2000.

[12] Charles H. Bennett and Gilles Brassard. Quantum cryptography: Public key distribution and coin tossing. *Theoretical Computer Science*, 560:7–11, 2014. Theoretical Aspects of Quantum Cryptography – celebrating 30 years of BB84.

[13] Anne Broadbent, Joseph Fitzsimons, and Elham Kashefi. Universal blind quantum computation. In *2009 50th Annual IEEE Symposium on Foundations of Computer Science*, pages 517–526. IEEE, 2009.

[14] Stefanie Barz, Elham Kashefi, Anne Broadbent, Joseph F Fitzsimons, Anton Zeilinger, and Philip Walther. Demonstration of blind quantum computing. *science*, 335(6066):303–308, 2012.

[15] Charles H. Bennett, Gilles Brassard, Claude Crépeau, Richard Jozsa, Asher Peres, and William K. Wootters. Teleporting an unknown quantum state via dual classical and einstein-podolsky-rosen channels. *Phys. Rev. Lett.*, 70:1895–1899, Mar 1993.

[16] D. Boschi, S. Branca, F. De Martini, L. Hardy, and S. Popescu. Experimental realization of teleporting an unknown pure quantum state via dual classical and einstein-podolsky-rosen channels. *Phys. Rev. Lett.*, 80:1121–1125, Feb 1998.

[17] Dik Bouwmeester, Jian-Wei Pan, Klaus Mattle, Manfred Eibl, Harald Weinfurter, and Anton Zeilinger. Experimental quantum teleportation. *Nature*, 390(6660):575–579, Dec 1997.

[18] C. L. Degen, F. Reinhard, and P. Cappellaro. Quantum sensing. *Rev. Mod. Phys.*, 89:035002, Jul 2017.

[19] I. K. Kominis, T. W. Kornack, J. C. Allred, and M. V. Romalis. A subfemtotesla multichannel atomic magnetometer. *Nature*, 422(6932):596–599, Apr 2003.

[20] R. L. Fagaly. Superconducting quantum interference device instruments and applications. *Review of Scientific Instruments*, 77(10):101101, 2006.

[21] David Toyli, Charles Casas, David Christle, Viatcheslav Dobrovitski, and David Awschalom. Fluorescence thermometry enhanced by the quantum coherence of single spins in diamond. *Proceedings of the National Academy of Sciences of the United States of America*, 110, 05 2013.

[22] P. Neumann, I. Jakobi, F. Dolde, C. Burk, R. Reuter, G. Waldherr, J. Honert, T. Wolf, A. Brunner, J. H. Shim, D. Suter, H. Sumiya, J. Isoya, and J. Wrachtrup. High-precision nanoscale temperature sensing using single defects in diamond. *Nano Letters*, 13(6):2738–2742, 2013. PMID: 23721106.

[23] G. Kucsko, P. C. Maurer, N. Y. Yao, M. Kubo, H. J. Noh, P. K. Lo, H. Park, and M. D. Lukin. Nanometre-scale thermometry in a living cell. *Nature*, 500(7460):54–58, Aug 2013.

[24] Marcus W. Doherty, Viktor V. Struzhkin, David A. Simpson, Liam P. McGuinness, Yufei Meng, Alastair Stacey, Timothy J. Karle, Russell J. Hemley, Neil B. Manson, Lloyd C. L. Hollenberg, and Steven Prawer. Electronic properties and metrology applications of the diamond nv$^-$ center under pressure. *Phys. Rev. Lett.*, 112:047601, Jan 2014.

[25] M. Kasevich and S. Chu. Measurement of the gravitational acceleration of an atom with a light-pulse atom interferometer. *Applied Physics B*, 54(5):321–332, May 1992.

[26] Achim Peters, Keng Yeow Chung, and Steven Chu. Measurement of gravitational acceleration by dropping atoms. *Nature*, 400(6747):849–852, Aug 1999.

[27] T Gustavson, Arnaud Landragin, and MA Kasevich. Rotation sensing with a dual atom-interferometer sagnac gyroscope. *Classical and Quantum Gravity*, 17:2385, 06 2000.

[28] J. J . Bollinger, Wayne M. Itano, D. J. Wineland, and D. J. Heinzen. Optimal frequency measurements with maximally correlated states. *Phys. Rev. A*, 54:R4649–R4652, Dec 1996.

[29] Vittorio Giovannetti, Seth Lloyd, and Lorenzo Maccone. Quantum metrology. *Phys. Rev. Lett.*, 96:010401, Jan 2006.

[30] Vittorio Giovannetti, Seth Lloyd, and Lorenzo Maccone. Advances in quantum metrology. *Nature Photonics*, 5(4):222–229, Apr 2011.

[31] T. D. Ladd, F. Jelezko, R. Laflamme, Y. Nakamura, C. Monroe, and J. L. O'Brien. Quantum computers. *Nature*, 464(7285):45–53, Mar 2010.

[32] J. I. Cirac and P. Zoller. Quantum computations with cold trapped ions. *Phys. Rev. Lett.*, 74:4091–4094, May 1995.

[33] Oliver Morsch and Markus Oberthaler. Dynamics of bose-einstein condensates in optical lattices. *Rev. Mod. Phys.*, 78:179–215, Feb 2006.

[34] Marco Anderlini, Patricia J. Lee, Benjamin L. Brown, Jennifer Sebby-Strabley, William D. Phillips, and J. V. Porto. Controlled exchange interaction between pairs of neutral atoms in an optical lattice. *Nature*, 448(7152):452–456, Jul 2007.

[35] Immanuel Bloch, Jean Dalibard, and Sylvain Nascimbène. Quantum simulations with ultracold quantum gases. *Nature Physics*, 8(4):267–276, Apr 2012.

[36] K. Wright, K. M. Beck, S. Debnath, J. M. Amini, Y. Nam, N. Grzesiak, J.-S. Chen, N. C. Pisenti, M. Chmielewski, C. Collins, K. M. Hudek, J. Mizrahi, J. D. Wong-Campos, S. Allen, J. Apisdorf, P. Solomon, M. Williams, A. M. Ducore, A. Blinov, S. M. Kreikemeier, V. Chaplin, M. Keesan, C. Monroe, and J. Kim. Benchmarking an 11-qubit quantum computer. *Nature Communications*, 10(1):5464, Nov 2019.

[37] Jonathan P. Home, David Hanneke, John D. Jost, Jason M. Amini, Dietrich Leibfried, and David J. Wineland. Complete methods set for scalable ion trap quantum information processing. *Science*, 325(5945):1227–1230, 2009.

[38] S. Olmschenk, D. N. Matsukevich, P. Maunz, D. Hayes, L.-M. Duan, and C. Monroe. Quantum teleportation between distant matter qubits. *Science*, 323(5913):486–489, 2009.

[39] H. B. Dang, A. C. Maloof, and M. V. Romalis. Ultrahigh sensitivity magnetic field and magnetization measurements with an atomic magnetometer. *Applied Physics Letters*, 97(15):151110, 2010.

[40] Kasper Jensen, Rima Budvytyte, Rodrigo A. Thomas, Tian Wang, Annette M. Fuchs, Mikhail V. Balabas, Georgios Vasilakis, Lars D. Mosgaard, Hans C. Stærkind, Jörg H. Müller, Thomas Heimburg, Søren-Peter Olesen, and Eugene S. Polzik. Non-invasive detection of animal nerve impulses with an atomic magnetometer operating near quantum limited sensitivity. *Scientific Reports*, 6(1):29638, Jul 2016.

[41] Y. Nakamura, Yu. A. Pashkin, and J. S. Tsai. Coherent control of macroscopic quantum states in a single-cooper-pair box. *Nature*, 398(6730):786–788, Apr 1999.

[42] D. Vion, A. Aassime, A. Cottet, P. Joyez, H. Pothier, C. Urbina, D. Esteve, and M. H. Devoret. Manipulating the quantum state of an electrical circuit. *Science*, 296(5569):886–889, 2002.

[43] J. A. Schreier, A. A. Houck, Jens Koch, D. I. Schuster, B. R. Johnson, J. M. Chow, J. M. Gambetta, J. Majer, L. Frunzio, M. H. Devoret, S. M. Girvin, and R. J. Schoelkopf. Suppressing charge noise decoherence in superconducting charge qubits. *Phys. Rev. B*, 77:180502, May 2008.

[44] Jonathan R. Friedman, Vijay Patel, W. Chen, S. K. Tolpygo, and J. E. Lukens. Quantum superposition of distinct macroscopic states. *Nature*, 406(6791):43–46, Jul 2000.

[45] Caspar H. van der Wal, A. C. J. ter Haar, F. K. Wilhelm, R. N. Schouten, C. J. P. M. Harmans, T. P. Orlando, Seth Lloyd, and J. E. Mooij. Quantum superposition of macroscopic persistent-current states. *Science*, 290(5492):773–777, 2000.

[46] I. Chiorescu, Y. Nakamura, C. J. P. M. Harmans, and J. E. Mooij. Coherent quantum dynamics of a superconducting flux qubit. *Science*, 299(5614):1869–1871, 2003.

[47] John M. Martinis, S. Nam, J. Aumentado, and C. Urbina. Rabi oscillations in a large josephson-junction qubit. *Phys. Rev. Lett.*, 89:117901, Aug 2002.

[48] Frank Arute, Kunal Arya, Ryan Babbush, Dave Bacon, Joseph C. Bardin, Rami Barends, Rupak Biswas, Sergio Boixo, Fernando G. S. L. Brandao, David A. Buell, Brian Burkett, Yu Chen, Zijun Chen, Ben Chiaro, Roberto Collins, William Courtney, Andrew Dunsworth, Edward Farhi, Brooks Foxen, Austin Fowler, Craig Gidney, Marissa Giustina, Rob Graff, Keith Guerin, Steve Habegger, Matthew P. Harrigan, Michael J. Hartmann, Alan Ho, Markus Hoffmann, Trent Huang, Travis S. Humble, Sergei V. Isakov, Evan Jeffrey, Zhang Jiang, Dvir Kafri, Kostyantyn Kechedzhi, Julian Kelly, Paul V. Klimov, Sergey Knysh, Alexander Korotkov, Fedor Kostritsa, David Landhuis, Mike Lindmark, Erik Lucero, Dmitry Lyakh, Salvatore Mandrà, Jarrod R. McClean, Matthew McEwen, Anthony Megrant, Xiao Mi, Kristel Michielsen, Masoud Mohseni, Josh Mutus, Ofer Naaman, Matthew Neeley, Charles Neill, Murphy Yuezhen Niu, Eric Ostby, Andre Petukhov, John C. Platt, Chris Quintana, Eleanor G. Rieffel, Pedram Roushan, Nicholas C. Rubin, Daniel Sank, Kevin J. Satzinger, Vadim Smelyanskiy, Kevin J. Sung, Matthew D. Trevithick, Amit Vainsencher, Benjamin Villalonga, Theodore White, Z. Jamie Yao, Ping Yeh, Adam Zalcman, Hartmut Neven, and John M. Martinis. Quantum supremacy using a programmable superconducting processor. *Nature*, 574(7779):505–510, Oct 2019.

[49] Petar Jurcevic, Ali Javadi-Abhari, Lev S Bishop, Isaac Lauer, Daniela F Bogorin, Markus Brink, Lauren Capelluto, Oktay Günlük, Toshinari Itoko, Naoki Kanazawa, Abhinav Kandala, George A Keefe, Kevin Krsulich, William Landers, Eric P Lewandowski, Douglas T McClure, Giacomo Nannicini, Adinath Narasgond, Hasan M Nayfeh, Emily Pritchett, Mary Beth Rothwell, Srikanth Srinivasan, Neereja Sundaresan, Cindy Wang, Ken X Wei, Christopher J Wood, Jeng-Bang Yau, Eric J Zhang, Oliver E Dial, Jerry M Chow, and Jay M Gambetta. Demonstration of quantum volume 64 on a superconducting quantum computing system. *Quantum Science and Technology*, 6(2):025020, mar 2021.

[50] R. C. Jaklevic, John Lambe, A. H. Silver, and J. E. Mercereau. Quantum interference effects in josephson tunneling. *Phys. Rev. Lett.*, 12:159–160, Feb 1964.

[51] P. W. Anderson and J. M. Rowell. Probable observation of the josephson superconducting tunneling effect. *Phys. Rev. Lett.*, 10:230–232, Mar 1963.

[52] D. Drung, C. Abmann, J. Beyer, A. Kirste, M. Peters, F. Ruede, and Th. Schurig. Highly sensitive and easy-to-use squid sensors. *IEEE Transactions on Applied Super-*

conductivity, 17(2):699–704, 2007.

[53] Denis Vasyukov, Yonathan Anahory, Lior Embon, Dorri Halbertal, Jo Cuppens, Lior Neeman, Amit Finkler, Yehonathan Segev, Yuri Myasoedov, Michael L. Rappaport, Martin E. Huber, and Eli Zeldov. A scanning superconducting quantum interference device with single electron spin sensitivity. *Nature Nanotechnology*, 8(9):639–644, Sep 2013.

[54] D. Halbertal, J. Cuppens, M. Ben Shalom, L. Embon, N. Shadmi, Y. Anahory, H. R. Naren, J. Sarkar, A. Uri, Y. Ronen, Y. Myasoedov, L. S. Levitov, E. Joselevich, A. K. Geim, and E. Zeldov. Nanoscale thermal imaging of dissipation in quantum systems. *Nature*, 539(7629):407–410, Nov 2016.

[55] David G. Cory, Amr F. Fahmy, and Timothy F. Havel. Ensemble Quantum Computing by NMR Spectroscopy. *Proceedings of the National Academy of Science*, 94(5):1634–1639, March 1997.

[56] David G. Cory, Mark D. Price, and Timothy F. Havel. Nuclear magnetic resonance spectroscopy: An experimentally accessible paradigm for quantum computing. *Physica D: Nonlinear Phenomena*, 120(1):82–101, 1998. Proceedings of the Fourth Workshop on Physics and Consumption.

[57] Neil A. Gershenfeld and Isaac L. Chuang. Bulk spin-resonance quantum computation. *Science*, 275(5298):350–356, 1997.

[58] Lorenza Viola and Seth Lloyd. Dynamical suppression of decoherence in two-state quantum systems. *Phys. Rev. A*, 58:2733–2744, Oct 1998.

[59] Lorenza Viola, Emanuel Knill, and Seth Lloyd. Dynamical decoupling of open quantum systems. *Phys. Rev. Lett.*, 82:2417–2421, Mar 1999.

[60] Wen Yang, Zhen-Yu Wang, and Ren-Bao Liu. Preserving qubit coherence by dynamical decoupling. *Frontiers of Physics in China*, 6(1):2–14, Mar 2011.

[61] B. E. Kane. A silicon-based nuclear spin quantum computer. *Nature*, 393(6681):133–137, May 1998.

[62] A. Gruber, A. Dräbenstedt, C. Tietz, L. Fleury, J. Wrachtrup, and C. von Borczyskowski. Scanning confocal optical microscopy and magnetic resonance on single defect centers. *Science*, 276(5321):2012–2014, 1997.

[63] F. Jelezko, I. Popa, A. Gruber, C. Tietz, J. Wrachtrup, A. Nizovtsev, and S. Kilin.

Single spin states in a defect center resolved by optical spectroscopy. *Applied Physics Letters*, 81(12):2160–2162, 2002.

[64] F. Jelezko, T. Gaebel, I. Popa, A. Gruber, and J. Wrachtrup. Observation of coherent oscillations in a single electron spin. *Phys. Rev. Lett.*, 92:076401, Feb 2004.

[65] Jörg Wrachtrup and Fedor Jelezko. Processing quantum information in diamond. *Journal of Physics: Condensed Matter*, 18(21):S807, may 2006.

[66] H. Bernien, B. Hensen, W. Pfaff, G. Koolstra, M. S. Blok, L. Robledo, T. H. Taminiau, M. Markham, D. J. Twitchen, L. Childress, and R. Hanson. Heralded entanglement between solid-state qubits separated by three metres. *Nature*, 497(7447):86–90, May 2013.

[67] B. Hensen, H. Bernien, A. E. Dréau, A. Reiserer, N. Kalb, M. S. Blok, J. Ruitenberg, R. F. L. Vermeulen, R. N. Schouten, C. Abellán, W. Amaya, V. Pruneri, M. W. Mitchell, M. Markham, D. J. Twitchen, D. Elkouss, S. Wehner, T. H. Taminiau, and R. Hanson. Loophole-free bell inequality violation using electron spins separated by 1.3 kilometres. *Nature*, 526(7575):682–686, Oct 2015.

[68] Kae Nemoto, Michael Trupke, Simon J. Devitt, Burkhard Scharfenberger, Kathrin Buczak, Jörg Schmiedmayer, and William J. Munro. Photonic quantum networks formed from nv centers. *Scientific Reports*, 6(1):26284, May 2016.

[69] J. M. Taylor, P. Cappellaro, L. Childress, L. Jiang, D. Budker, P. R. Hemmer, A. Yacoby, R. Walsworth, and M. D. Lukin. High-sensitivity diamond magnetometer with nanoscale resolution. *Nature Physics*, 4(10):810–816, Oct 2008.

[70] C. L. Degen. Scanning magnetic field microscope with a diamond single-spin sensor. *Applied Physics Letters*, 92(24):243111, 2008.

[71] Gopalakrishnan Balasubramanian, I. Y. Chan, Roman Kolesov, Mohannad Al-Hmoud, Julia Tisler, Chang Shin, Changdong Kim, Aleksander Wojcik, Philip R. Hemmer, Anke Krueger, Tobias Hanke, Alfred Leitenstorfer, Rudolf Bratschitsch, Fedor Jelezko, and Jörg Wrachtrup. Nanoscale imaging magnetometry with diamond spins under ambient conditions. *Nature*, 455(7213):648–651, Oct 2008.

[72] J. R. Maze, P. L. Stanwix, J. S. Hodges, S. Hong, J. M. Taylor, P. Cappellaro, L. Jiang, M. V. Gurudev Dutt, E. Togan, A. S. Zibrov, A. Yacoby, R. L. Walsworth, and M. D. Lukin. Nanoscale magnetic sensing with an individual electronic spin in diamond. *Nature*, 455(7213):644–647, Oct 2008.

[73] F. Dolde, H. Fedder, M. W. Doherty, T. Nöbauer, F. Rempp, G. Balasubramanian, T. Wolf, F. Reinhard, L. C. L. Hollenberg, F. Jelezko, and J. Wrachtrup. Electric-field sensing using single diamond spins. *Nature Physics*, 7(6):459–463, Jun 2011.

[74] T. Staudacher, F. Shi, S. Pezzagna, J. Meijer, J. Du, C. A. Meriles, F. Reinhard, and J. Wrachtrup. Nuclear magnetic resonance spectroscopy on a (5-nanometer)³ sample volume. *Science*, 339(6119):561–563, 2013.

[75] H. J. Mamin, M. Kim, M. H. Sherwood, C. T. Rettner, K. Ohno, D. D. Awschalom, and D. Rugar. Nanoscale nuclear magnetic resonance with a nitrogen-vacancy spin sensor. *Science*, 339(6119):557–560, 2013.

[76] L. P. McGuinness, Y. Yan, A. Stacey, D. A. Simpson, L. T. Hall, D. Maclaurin, S. Prawer, P. Mulvaney, J. Wrachtrup, F. Caruso, R. E. Scholten, and L. C. L. Hollenberg. Quantum measurement and orientation tracking of fluorescent nanodiamonds inside living cells. *Nature Nanotechnology*, 6(6):358–363, Jun 2011.

[77] S. Steinert, F. Dolde, P. Neumann, A. Aird, B. Naydenov, G. Balasubramanian, F. Jelezko, and J. Wrachtrup. High sensitivity magnetic imaging using an array of spins in diamond. *Review of Scientific Instruments*, 81(4):043705, 2010.

[78] Romana Schirhagl, Kevin Chang, Michael Loretz, and Christian L. Degen. Nitrogen-vacancy centers in diamond: Nanoscale sensors for physics and biology. *Annual Review of Physical Chemistry*, 65(1):83–105, 2014. PMID: 24274702.

[79] J. Meijer, B. Burchard, M. Domhan, C. Wittmann, T. Gaebel, I. Popa, F. Jelezko, and J. Wrachtrup. Generation of single color centers by focused nitrogen implantation. *Applied Physics Letters*, 87(26), 12 2005. 261909.

[80] Marcus W. Doherty, Neil B. Manson, Paul Delaney, Fedor Jelezko, Jörg Wrachtrup, and Lloyd C.L. Hollenberg. The nitrogen-vacancy colour centre in diamond. *Physics Reports*, 528(1):1–45, 2013. The nitrogen-vacancy colour centre in diamond.

[81] David A. Hopper, Henry J. Shulevitz, and Lee C. Bassett. Spin readout techniques of the nitrogen-vacancy center in diamond. *Micromachines*, 9(9), 2018.

[82] J H N Loubser and J A van Wyk. Electron spin resonance in the study of diamond. *Reports on Progress in Physics*, 41(8):1201, aug 1978.

[83] Y. Chu, N.P. de Leon, B.J. Shields, B. Hausmann, R. Evans, E. Togan, M. J. Burek, M. Markham, A. Stacey, A.S. Zibrov, A. Yacoby, D.J. Twitchen, M. Loncar, H. Park, P. Maletinsky, and M.D. Lukin. Coherent optical transitions in implanted nitrogen

vacancy centers. *Nano Letters*, 14(4):1982–1986, 2014. PMID: 24588353.

[84] Lee C. Bassett, Audrius Alkauskas, Annemarie L. Exarhos, and Kai-Mei C. Fu. Quantum defects by design. *Nanophotonics*, 8(11):1867–1888, 2019.

[85] Gary Wolfowicz, F. Joseph Heremans, Christopher P. Anderson, Shun Kanai, Hosung Seo, Adam Gali, Giulia Galli, and David D. Awschalom. Quantum guidelines for solid-state spin defects. *Nature Reviews Materials*, 6(10):906–925, Oct 2021.

[86] David D. Awschalom, Lee C. Bassett, Andrew S. Dzurak, Evelyn L. Hu, and Jason R. Petta. Quantum spintronics: Engineering and manipulating atom-like spins in semiconductors. *Science*, 339(6124):1174–1179, 2013.

[87] David D. Awschalom, Ronald Hanson, Jörg Wrachtrup, and Brian B. Zhou. Quantum technologies with optically interfaced solid-state spins. *Nature Photonics*, 12(9):516–527, Sep 2018.

[88] Meng Ye, Hosung Seo, and Giulia Galli. Spin coherence in two-dimensional materials. *npj Computational Materials*, 5(1):44, Apr 2019.

[89] Andreas Gottscholl, Mehran Kianinia, Victor Soltamov, Sergei Orlinskii, Georgy Mamin, Carlo Bradac, Christian Kasper, Klaus Krambrock, Andreas Sperlich, Milos Toth, Igor Aharonovich, and Vladimir Dyakonov. Initialization and read-out of intrinsic spin defects in a van der waals crystal at room temperature. *Nature Materials*, 19(5):540–545, May 2020.

[90] Nathan Chejanovsky, Amlan Mukherjee, Jianpei Geng, Yu-Chen Chen, Youngwook Kim, Andrej Denisenko, Amit Finkler, Takashi Taniguchi, Kenji Watanabe, Durga Bhaktavatsala Rao Dasari, Philipp Auburger, Adam Gali, Jurgen H. Smet, and Jörg Wrachtrup. Single-spin resonance in a van der waals embedded paramagnetic defect. *Nature Materials*, 20(8):1079–1084, Aug 2021.

[91] Hannah L. Stern, Qiushi Gu, John Jarman, Simone Eizagirre Barker, Noah Mendelson, Dipankar Chugh, Sam Schott, Hoe H. Tan, Henning Sirringhaus, Igor Aharonovich, and Mete Atatüre. Room-temperature optically detected magnetic resonance of single defects in hexagonal boron nitride. *Nature Communications*, 13(1):618, Feb 2022.

[92] Andreas Gottscholl, Matthias Diez, Victor Soltamov, Christian Kasper, Dominik Krauße, Andreas Sperlich, Mehran Kianinia, Carlo Bradac, Igor Aharonovich, and Vladimir Dyakonov. Spin defects in hbn as promising temperature, pressure and magnetic field quantum sensors. *Nature Communications*, 12(1):4480, Jul 2021.

[93] A. J. Healey, S. C. Scholten, T. Yang, J. A. Scott, G. J. Abrahams, I. O. Robertson, X. F. Hou, Y. F. Guo, S. Rahman, Y. Lu, M. Kianinia, I. Aharonovich, and J.-P. Tetienne. Quantum microscopy with van der waals heterostructures. *Nature Physics*, 19(1):87–91, Jan 2023.

[94] Annemarie L. Exarhos, David A. Hopper, Raj N. Patel, Marcus W. Doherty, and Lee C. Bassett. Magnetic-field-dependent quantum emission in hexagonal boron nitride at room temperature. *Nature Communications*, 10(1):222, Jan 2019.

[95] S. Alex Breitweiser, Annemarie L. Exarhos, Raj N. Patel, Jennifer Saouaf, Benjamin Porat, David A. Hopper, and Lee C. Bassett. Efficient optical quantification of heterogeneous emitter ensembles. *ACS Photonics*, 7(1):288–295, 2020.

[96] Mete Atatüre, Dirk Englund, Nick Vamivakas, Sang-Yun Lee, and Joerg Wrachtrup. Material platforms for spin-based photonic quantum technologies. *Nat. Rev. Mater*, 3(5):38, 2018.

[97] G. Davies, M. F. Hamer, and P. W. Charles. Optical studies of the 1.945 eV vibronic band in diamond. *Proc. R. Soc. London, Ser. A*, 348:285, 1976.

[98] J.H.N. Loubser and J.A. Van Wyk. Optical spin-polarisation in a triplet state in irradiated and annealed type 1b diamonds. *Diamond Res.*, 9:11, 1977.

[99] Victor M Acosta, Erik Bauch, Micah P Ledbetter, Charles Santori, K-MC Fu, Paul E Barclay, Raymond G Beausoleil, Héloïse Linget, Jean Francois Roch, Francois Treussart, et al. Diamonds with a high density of nitrogen-vacancy centers for magnetometry applications. *Phys. Rev. B: Condens. Matter Mater. Phys.*, 80(11):115202, 2009.

[100] FC Waldermann, Paolo Olivero, J Nunn, K Surmacz, ZY Wang, D Jaksch, RA Taylor, IA Walmsley, M Draganski, P Reichart, et al. Creating diamond color centers for quantum optical applications. *Diamond and Related Materials*, 16(11):1887–1895, 2007.

[101] Igor Aharonovich, Dirk Englund, and Milos Toth. Solid-state single-photon emitters. *Nat. Photonics*, 10(10):631, 2016.

[102] Guillaume Cassabois, Pierre Valvin, and Bernard Gil. Hexagonal boron nitride is an indirect bandgap semiconductor. *Nat. Photonics*, 10(4):262, 2016.

[103] Nicholas L McDougall, Jim G Partridge, Rebecca J Nicholls, Salvy P Russo, and Dougal G McCulloch. Influence of point defects on the near edge structure of hexagonal

boron nitride. *Phys. Rev. B: Condens. Matter Mater. Phys.*, 96(14):144106, 2017.

[104] L Weston, D Wickramaratne, M Mackoit, A Alkauskas, and CG Van de Walle. Native point defects and impurities in hexagonal boron nitride. *Phys. Rev. B: Condens. Matter Mater. Phys.*, 97(21):214104, 2018.

[105] Andre K Geim and Irina V Grigorieva. Van der waals heterostructures. *Nature*, 499(7459):419, 2013.

[106] Joshua David Caldwell, Igor Aharonovich, Guillaume Cassabois, James H Edgar, Bernard Gil, and D. N. Basov. Photonics with hexagonal boron nitride. *Nat. Rev. Mater*, 4:552, 2019.

[107] Toan Trong Tran, Kerem Bray, Michael J. Ford, Milos Toth, and Igor Aharonovich. Quantum emission from hexagonal boron nitride monolayers. *Nat. Nanotechnol.*, 11:37, Oct 2015.

[108] Toan Trong Tran, Christopher Elbadawi, Daniel Totonjian, Charlene J Lobo, Gabriele Grosso, Hyowon Moon, Dirk R Englund, Michael J Ford, Igor Aharonovich, and Milos Toth. Robust multicolor single photon emission from point defects in hexagonal boron nitride. *ACS Nano*, 10(8):7331–7338, 2016.

[109] Annemarie L. Exarhos, David A. Hopper, Richard R. Grote, Audrius Alkauskas, and Lee C. Bassett. Optical signatures of quantum emitters in suspended hexagonal boron nitride. *ACS Nano*, 11(3):3328–3336, 2017.

[110] Nathan Chejanovsky, Mohammad Rezai, Federico Paolucci, Youngwook Kim, Torsten Rendler, Wafa Rouabeh, Felipe Fávaro de Oliveira, Patrick Herlinger, Andrej Denisenko, Sen Yang, et al. Structural attributes and photodynamics of visible spectrum quantum emitters in hexagonal boron nitride. *Nano Lett.*, 16(11):7037–7045, 2016.

[111] Nicholas R. Jungwirth, Brian Calderon, Yanxin Ji, Michael G. Spencer, Michael E. Flatté, and Gregory D. Fuchs. Temperature dependence of wavelength selectable zero-phonon emission from single defects in hexagonal boron nitride. *Nano Lett.*, 16(10):6052–6057, 2016.

[112] LJ Martínez, Thomas Pelini, V Waselowski, JR Maze, Bernard Gil, Guillaume Cassabois, and Vincent Jacques. Efficient single photon emission from a high-purity hexagonal boron nitride crystal. *Phys. Rev. B: Condens. Matter Mater. Phys.*, 94(12):121405, 2016.

[113] Milos Toth and Igor Aharonovich. Single photon sources in atomically thin materials. *Annu. Rev. Phys. Chem.*, 70, 2019.

[114] Gabriele Grosso, Hyowon Moon, Benjamin Lienhard, Sajid Ali, Dmitri K Efetov, Marco M Furchi, Pablo Jarillo-Herrero, Michael J Ford, Igor Aharonovich, and Dirk Englund. Tunable and high-purity room temperature single-photon emission from atomic defects in hexagonal boron nitride. *Nat. Commun.*, 8(1):705, 2017.

[115] Gichang Noh, Daebok Choi, Jin-Hun Kim, Dong-Gil Im, Yoon-Ho Kim, Hosung Seo, and Jieun Lee. Stark tuning of single-photon emitters in hexagonal boron nitride. *Nano Lett.*, 18(8):4710–4715, 2018.

[116] Tobias Vogl, Ruvi Lecamwasam, Ben C. Buchler, Yuerui Lu, and Ping Koy Lam. Compact cavity-enhanced single-photon generation with hexagonal boron nitride. *ACS Photonics*, 6(8):1955–1962, 2019.

[117] Xiangzhi Li, Robert A. Scully, Kamran Shayan, Yue Luo, and Stefan Strauf. Near-unity light collection efficiency from quantum emitters in boron nitride by coupling to metallo-dielectric antennas. *ACS Nano*, 13(6):6992–6997, 2019.

[118] Sherif Abdulkader Tawfik, Sajid Ali, Marco Fronzi, Mehran Kianinia, Toan Trong Tran, Catherine Stampfl, Igor Aharonovich, Milos Toth, and Michael J Ford. First-principles investigation of quantum emission from hbn defects. *Nanoscale*, 9(36):13575–13582, 2017.

[119] A Sajid, Jeffrey R Reimers, and Michael J Ford. Defect states in hexagonal boron nitride: Assignments of observed properties and prediction of properties relevant to quantum computation. *Phys. Rev. B: Condens. Matter Mater. Phys.*, 97(6):064101, 2018.

[120] Mehdi Abdi, Jyh-Pin Chou, Adam Gali, and Martin B Plenio. Color centers in hexagonal boron nitride monolayers: A group theory and ab initio analysis. *ACS Photonics*, 5(5):1967–1976, 2018.

[121] Zai-Quan Xu, Christopher Elbadawi, Toan Trong Tran, Mehran Kianinia, Xiuling Li, Daobin Liu, Timothy B Hoffman, Minh Nguyen, Sejeong Kim, James H Edgar, et al. Single photon emission from plasma treated 2d hexagonal boron nitride. *Nanoscale*, 10(17):7957–7965, 2018.

[122] Tobias Vogl, Geoff Campbell, Ben C Buchler, Yuerui Lu, and Ping Koy Lam. Fabrication and deterministic transfer of high-quality quantum emitters in hexagonal boron nitride. *ACS Photonics*, 5(6):2305–2312, 2018.

[123] Sumin Choi, Toan Trong Tran, Christopher Elbadawi, Charlene Lobo, Xuewen Wang, Saulius Juodkazis, Gediminas Seniutinas, Milos Toth, and Igor Aharonovich. Engineering and localization of quantum emitters in large hexagonal boron nitride layers. *ACS Appl. Mater. Interfaces*, 8(43):29642–29648, 2016.

[124] Hanh Ngoc My Duong, Minh Anh Phan Nguyen, Mehran Kianinia, Takeshi Ohshima, Hiroshi Abe, Kenji Watanabe, Takashi Taniguchi, James H Edgar, Igor Aharonovich, and Milos Toth. Effects of high-energy electron irradiation on quantum emitters in hexagonal boron nitride. *ACS Appl. Mater. Interfaces*, 10(29):24886–24891, 2018.

[125] Nicholas V Proscia, Zav Shotan, Harishankar Jayakumar, Prithvi Reddy, Charles Cohen, Michael Dollar, Audrius Alkauskas, Marcus Doherty, Carlos A Meriles, and Vinod M Menon. Near-deterministic activation of room-temperature quantum emitters in hexagonal boron nitride. *Optica*, 5(9):1128–1134, 2018.

[126] Joshua Ziegler, Rachael Klaiss, Andrew Blaikie, David Miller, Viva R Horowitz, and Benjamín J Alemán. Deterministic quantum emitter formation in hexagonal boron nitride via controlled edge creation. *Nano Lett.*, 19(3):2121–2127, 2019.

[127] Rainer Storn and Kenneth Price. Differential evolution – a simple and efficient heuristic for global optimization over continuous spaces. *Journal of Global Optimization*, 11(4):341–359, Dec 1997.

[128] Tobias Vogl, Marcus W. Doherty, Ben C. Buchler, Yuerui Lu, and Ping Koy Lam. Atomic localization of quantum emitters in multilayer hexagonal boron nitride. *Nanoscale*, 11:14362–14371, 2019.

[129] J Kotakoski, CH Jin, O Lehtinen, K Suenaga, and AV Krasheninnikov. Electron knock-on damage in hexagonal boron nitride monolayers. *Phys. Rev. B: Condens. Matter Mater. Phys.*, 82(11):113404, 2010.

[130] M. E. Turiansky, A. Alkauskas, L. C. Bassett, and C. G. Van de Walle. Dangling bonds in hexagonal boron nitride as single-photon emitters. *Phys. Rev. Lett.*, 123:127401, 2019.

[131] Zav Shotan, Harishankar Jayakumar, Christopher R Considine, Mazena Mackoit, Helmut Fedder, Jorg Wrachtrup, Audrius Alkauskas, Marcus W Doherty, Vinod M Menon, and Carlos A Meriles. Photoinduced modification of single-photon emitters in hexagonal boron nitride. *ACS Photonics*, 3(12):2490–2496, 2016.

[132] Niko Nikolay, Noah Mendelson, Ersan Özelci, Bernd Sontheimer, Florian Böhm, Günter Kewes, Milos Toth, Igor Aharonovich, and Oliver Benson. Direct measurement

of quantum efficiency of single-photon emitters in hexagonal boron nitride. *Optica*, 6(8):1084–1088, Aug 2019.

[133] Noah Mendelson, Zai-Quan Xu, Toan Trong Tran, Mehran Kianinia, John Scott, Carlo Bradac, Igor Aharonovich, and Milos Toth. Engineering and tuning of quantum emitters in few-layer hexagonal boron nitride. *ACS Nano*, 13(3):3132–3140, 2019.

[134] Jean Comtet, Evgenii Glushkov, Vytautas Navikas, Jiandong Feng, Vitaliy Babenko, Stephan Hofmann, Kenji Watanabe, Takashi Taniguchi, and Aleksandra Radenovic. Wide-field spectral super-resolution mapping of optically active defects in hexagonal boron nitride. *Nano Lett.*, 19(4):2516–2523, 2019.

[135] Hannah L Stern, Ruizhi Wang, Ye Fan, Ryo Mizuta, James C Stewart, Lisa-Maria Needham, Trevor D Roberts, Rebecca Wai, Naomi S Ginsberg, David Klenerman, et al. Spectrally resolved photodynamics of individual emitters in large-area monolayers of hexagonal boron nitride. *ACS Nano*, 13(4):4538–4547, 2019.

[136] Srivatsa Chakravarthi, Chris Moore, April Opsvig, Emma Hunt, Andrew Ivanov, Ian Christen, Scott Dunham, and Kai-Mei C Fu. A window into nv center kinetics via repeated annealing and spatial tracking of thousands of individual nv centers. *arXiv preprint arXiv:1907.07793*, 2019.

[137] D. A. Hopper. *PREPARING AND MEASURING SINGLE SPINS IN DIAMOND AT ROOM TEMPERATURE*. PhD thesis, Philadelphia PA, 2019.

[138] D A Hopper, J D Lauigan, T Y Huang, and L C Bassett. Real-time charge initialization of diamond nitrogen-vacancy centers for enhanced spin readout. *Phys. Rev. Applied*, 13:024016, 2020.

[139] J.R. Johansson, P.D. Nation, and Franco Nori. Qutip: An open-source python framework for the dynamics of open quantum systems. *Computer Physics Communications*, 183(8):1760–1772, 2012.

[140] J.R. Johansson, P.D. Nation, and Franco Nori. Qutip 2: A python framework for the dynamics of open quantum systems. *Computer Physics Communications*, 184(4):1234–1240, 2013.

[141] L. Jiang, J. S. Hodges, J. R. Maze, P. Maurer, J. M. Taylor, D. G. Cory, P. R. Hemmer, R. L. Walsworth, A. Yacoby, A. S. Zibrov, and M. D. Lukin. Repetitive readout of a single electronic spin via quantum logic with nuclear spin ancillae. *Science*, 326(5950):267–272, 2009.

[142] Sebastian Zaiser, Torsten Rendler, Ingmar Jakobi, Thomas Wolf, Sang-Yun Lee, Samuel Wagner, Ville Bergholm, Thomas Schulte-Herbrüggen, Philipp Neumann, and Jörg Wrachtrup. Enhancing quantum sensing sensitivity by a quantum memory. *Nature Communications*, 7(1):12279, Aug 2016.

[143] Tobias Rosskopf, Jonathan Zopes, Jens M. Boss, and Christian L. Degen. A quantum spectrum analyzer enhanced by a nuclear spin memory. *npj Quantum Information*, 3(1):33, Aug 2017.

[144] M. V. Gurudev Dutt, L. Childress, L. Jiang, E. Togan, J. Maze, F. Jelezko, A. S. Zibrov, P. R. Hemmer, and M. D. Lukin. Quantum register based on individual electronic and nuclear spin qubits in diamond. *Science*, 316(5829):1312–1316, 2007.

[145] P. C. Maurer, G. Kucsko, C. Latta, L. Jiang, N. Y. Yao, S. D. Bennett, F. Pastawski, D. Hunger, N. Chisholm, M. Markham, D. J. Twitchen, J. I. Cirac, and M. D. Lukin. Room-temperature quantum bit memory exceeding one second. *Science*, 336(6086):1283–1286, 2012.

[146] John J. L. Morton, Alexei M. Tyryshkin, Richard M. Brown, Shyam Shankar, Brendon W. Lovett, Arzhang Ardavan, Thomas Schenkel, Eugene E. Haller, Joel W. Ager, and S. A. Lyon. Solid-state quantum memory using the 31p nuclear spin. *Nature*, 455(7216):1085–1088, Oct 2008.

[147] Gopalakrishnan Balasubramanian, Philipp Neumann, Daniel Twitchen, Matthew Markham, Roman Kolesov, Norikazu Mizuochi, Junichi Isoya, Jocelyn Achard, Johannes Beck, Julia Tissler, Vincent Jacques, Philip R. Hemmer, Fedor Jelezko, and Jörg Wrachtrup. Ultralong spin coherence time in isotopically engineered diamond. *Nature Materials*, 8(5):383–387, May 2009.

[148] L. Childress, M. V. Gurudev Dutt, J. M. Taylor, A. S. Zibrov, F. Jelezko, J. Wrachtrup, P. R. Hemmer, and M. D. Lukin. Coherent dynamics of coupled electron and nuclear spin qubits in diamond. *Science*, 314(5797):281–285, 2006.

[149] R. Hanson, V. V. Dobrovitski, A. E. Feiguin, O. Gywat, and D. D. Awschalom. Coherent dynamics of a single spin interacting with an adjustable spin bath. *Science*, 320(5874):352–355, 2008.

[150] W. M. Witzel and S. Das Sarma. Quantum theory for electron spin decoherence induced by nuclear spin dynamics in semiconductor quantum computer architectures: Spectral diffusion of localized electron spins in the nuclear solid-state environment. *Phys. Rev. B*, 74:035322, Jul 2006.

[151] Nan Zhao, Sai-Wah Ho, and Ren-Bao Liu. Decoherence and dynamical decoupling control of nitrogen vacancy center electron spins in nuclear spin baths. *Phys. Rev. B*, 85:115303, Mar 2012.

[152] L. T. Hall, J. H. Cole, and L. C. L. Hollenberg. Analytic solutions to the central-spin problem for nitrogen-vacancy centers in diamond. *Phys. Rev. B*, 90:075201, Aug 2014.

[153] G. de Lange, Z. H. Wang, D. Ristè, V. V. Dobrovitski, and R. Hanson. Universal dynamical decoupling of a single solid-state spin from a spin bath. *Science*, 330(6000):60–63, 2010.

[154] T. H. Taminiau, J. J. T. Wagenaar, T. van der Sar, F. Jelezko, V. V. Dobrovitski, and R. Hanson. Detection and control of individual nuclear spins using a weakly coupled electron spin. *Phys. Rev. Lett.*, 109:137602, Sep 2012.

[155] Terry Gullion, David B Baker, and Mark S Conradi. New, compensated carr-purcell sequences. *Journal of Magnetic Resonance (1969)*, 89(3):479–484, 1990.

[156] P. L. Stanwix, L. M. Pham, J. R. Maze, D. Le Sage, T. K. Yeung, P. Cappellaro, P. R. Hemmer, A. Yacoby, M. D. Lukin, and R. L. Walsworth. Coherence of nitrogen-vacancy electronic spin ensembles in diamond. *Phys. Rev. B*, 82:201201, Nov 2010.

[157] T. H. Taminiau, J. Cramer, T. van der Sar, V. V. Dobrovitski, and R. Hanson. Universal control and error correction in multi-qubit spin registers in diamond. *Nature Nanotechnology*, 9(3):171–176, Mar 2014.

[158] M. H. Abobeih, J. Randall, C. E. Bradley, H. P. Bartling, M. A. Bakker, M. J. Degen, M. Markham, D. J. Twitchen, and T. H. Taminiau. Atomic-scale imaging of a 27-nuclear-spin cluster using a quantum sensor. *Nature*, 576(7787):411–415, Dec 2019.

[159] Vadim S Grechishkin and Nikolai Ya Sinyavskii. New technologies: nuclear quadrupole resonance as an explosive and narcotic detection technique. *Physics-Uspekhi*, 40(4):393, apr 1997.

[160] Elizabeth Balchin, David J. Malcolme-Lawes, Iain J. F. Poplett, Michael D. Rowe, John A. S. Smith, Gareth E. S. Pearce, and Stephen A. C. Wren. Potential of nuclear quadrupole resonance in pharmaceutical analysis. *Analytical Chemistry*, 77(13):3925–3930, 2005. PMID: 15987093.

[161] I. Lovchinsky, J. D. Sanchez-Yamagishi, E. K. Urbach, S. Choi, S. Fang, T. I. Andersen, K. Watanabe, T. Taniguchi, A. Bylinskii, E. Kaxiras, P. Kim, H. Park, and M. D. Lukin. Magnetic resonance spectroscopy of an atomically thin material using a single-

spin qubit. *Science*, 355(6324):503–507, 2017.

[162] Jacob Henshaw, Pauli Kehayias, Maziar Saleh Ziabari, Michael Titze, Erin Morissette, Kenji Watanabe, Takashi Taniguchi, J. I. A. Li, Victor M. Acosta, Edward S. Bielejec, Michael P. Lilly, and Andrew M. Mounce. Nanoscale solid-state nuclear quadrupole resonance spectroscopy using depth-optimized nitrogen-vacancy ensembles in diamond. *Applied Physics Letters*, 120(17):174002, 2022.

[163] I. Lovchinsky, A. O. Sushkov, E. Urbach, N. P. de Leon, S. Choi, K. De Greve, R. Evans, R. Gertner, E. Bersin, C. Müller, L. McGuinness, F. Jelezko, R. L. Walsworth, H. Park, and M. D. Lukin. Nuclear magnetic resonance detection and spectroscopy of single proteins using quantum logic. *Science*, 351(6275):836–841, 2016.

[164] Ashok Ajoy, Yi-Xiang Liu, Kasturi Saha, Luca Marseglia, Jean-Christophe Jaskula, Ulf Bissbort, and Paola Cappellaro. Quantum interpolation for high-resolution sensing. *Proceedings of the National Academy of Sciences*, 114(9):2149–2153, 2017.

[165] J. A. S. Smith. Nuclear quadrupole resonance spectroscopy. general principles. *Journal of Chemical Education*, 48(1):39, 1971.

[166] Chang S. Shin, Mark C. Butler, Hai-Jing Wang, Claudia E. Avalos, Scott J. Seltzer, Ren-Bao Liu, Alexander Pines, and Vikram S. Bajaj. Optically detected nuclear quadrupolar interaction of ^{14}N in nitrogen-vacancy centers in diamond. *Phys. Rev. B*, 89:205202, May 2014.

[167] Yi-Xiang Liu, Ashok Ajoy, and Paola Cappellaro. Nanoscale vector dc magnetometry via ancilla-assisted frequency up-conversion. *Phys. Rev. Lett.*, 122:100501, Mar 2019.

[168] Tanmoy Chakraborty, Jingfu Zhang, and Dieter Suter. Polarizing the electronic and nuclear spin of the NV-center in diamond in arbitrary magnetic fields: analysis of the optical pumping process. *New Journal of Physics*, 19(7):073030, jul 2017.

[169] Ilai Schwartz, Joachim Rosskopf, Simon Schmitt, Benedikt Tratzmiller, Qiong Chen, Liam P. McGuinness, Fedor Jelezko, and Martin B. Plenio. Blueprint for nanoscale nmr. *Scientific Reports*, 9(1):6938, May 2019.

[170] David A. Hopper, Joseph D. Lauigan, Tzu-Yung Huang, and Lee C. Bassett. Real-time charge initialization of diamond nitrogen-vacancy centers for enhanced spin readout. *Phys. Rev. Appl.*, 13:024016, Feb 2020.

[171] Kaisarbek Omirzakhov, Mohamad Hossein Idjadi, Tzu-Yung Huang, S. Alex Breitweiser, David A. Hopper, Lee C. Bassett, and Firooz Aflatouni. An integrated

reconfigurable spin control system on 180 nm cmos for diamond nv centers. *IEEE Transactions on Microwave Theory and Techniques*, pages 1–12, 2023.

[172] Ilai Schwartz, Jochen Scheuer, Benedikt Tratzmiller, Samuel Müller, Qiong Chen, Ish Dhand, Zhen-Yu Wang, Christoph Müller, Boris Naydenov, Fedor Jelezko, and Martin B. Plenio. Robust optical polarization of nuclear spin baths using hamiltonian engineering of nitrogen-vacancy center quantum dynamics. *Science Advances*, 4(8):eaat8978, 2018.

[173] Benedikt Tratzmiller, Jan F. Haase, Zhenyu Wang, and Martin B. Plenio. Parallel selective nuclear-spin addressing for fast high-fidelity quantum gates. *Phys. Rev. A*, 103:012607, Jan 2021.

[174] Johan Philip. The probability distribution of the distance between two random points in a box. https://people.kth.se/~johanph/habc.pdf.

[175] T. Hauschild and M. Jentschel. Comparison of maximum likelihood estimation and chi-square statistics applied to counting experiments. *Nucl. Instrum. Methods Phys. Res., Sect. A*, 457(1):384 – 401, 2001.

[176] Markus Buehren. Differential evolution (mathworks file exchange package). https://www.mathworks.com/matlabcentral/fileexchange/18593-differential-evolution.